2000

# Optimization of a helicon plasma source for maximum density with minimal ion heating

Matthew M. Balkey
*West Virginia University*

## Recommended Citation

Balkey, Matthew M., "Optimization of a helicon plasma source for maximum density with minimal ion heating" (2000). *Graduate Theses, Dissertations, and Problem Reports*. 1195.
https://researchrepository.wvu.edu/etd/1195

# OPTIMIZATION OF A HELICON PLASMA SOURCE FOR MAXIMUM DENSITY WITH MINIMAL ION HEATING

Matthew M. Balkey

Dissertation submitted to the College of Arts and Sciences at
West Virginia University
In partial fulfillment of the requirements for the degree of

Doctor of Philosophy
in
Physics

E. E. Scime, Ph. D., chair
H. A. Weldon , Ph. D.
J. E. Littleton, Ph. D.
L. E. Halliburton, Ph. D.
C. D. Stinespring, Ph. D.

Department of Physics
Morgantown, West Virginia
2000

Keywords: Plasma Physics, Helicon, Ion Heating

# Abstract

## Optimization of a Helicon Plasma Source for Maximum Density with Minimal Ion Heating

**Matthew M. Balkey**

Measurements of electron density and perpendicular ion temperatures in an argon helicon plasma are presented for five different antennas: A Nagoya type III antenna, a double-saddle antenna, a 19 cm long $m = +1$ helical antenna, a 30 cm long $m = +1$ helical antenna and a 19 cm $m = +1$ helical antenna with wide straps. Electromagnetic wave measurements in the range from 100 kHz to 50 MHz are also presented for a wide range of plasma parameters. The data show a clear transition between RF power coupling to the plasma to create density and coupling to heat ions. The transition from plasma production to ion heating indicates that the mechanism responsible for heating the ions is distinct from the mechanism responsible for ionizing the plasma in a helicon source. The primary objective of the experiments described here is to identify the operational conditions for a helicon source such that the intrinsic ion heating is minimized without sacrificing density production. Secondary objectives of this project include: identifying the optimal antenna configuration for density production and/or ion heating, investigating the mechanism responsible for ion heating through measurements of the fluctuating magnetic field at the edge of the source, and determining if downstream density measurements can be used as a quantitative measure of the electron density in the helicon source.

## ACKNOWLEDGMENTS

I would like to thank my advisor, Professor Earl E. Scime for his support, guidance, and patience. John Kline, Robert Boivin, and Paul Keiter provided necessary technical assistance and advice. Brian Kent and Rick Soulsby were very helpful in many ways around the lab. The shop team of Carl Weber, Doug Mathess, and Tom Milam were an invaluable resource. Thanks to Bruce Dean for the wonderful discussions during the hours spent running on the streets of Morgantown. I owe a debt of gratitude to Bob Spangler for helping me discover the joys of kayaking (my life will never be the same) to Joanna Matheson for the laughs, friendship, and of course, a home. I want to thank my family, Martha, Robert John, Amy, Kirk, and Spencer for their prayers and loving support. Finally, I want to thank Bill Amatucci for his patience and encouragement over the past year.

## TABLE OF CONTENTS

# 1.0 INTRODUCTION

## 1.1 HISTORY OF HELICON SOURCES

Helicon plasma research has developed into an active research area since the discovery of the helicon source in the 1960's [*Boswell*, 1970]. The helicon source has been suggested for numerous applications including plasma processing, plasma rockets, and the study of space physics. The name of the helicon source originates from the helicon wave. The helicon wave is a right-hand, circularly polarized, electromagnetic wave confined inside an insulating cylinder and generally lies in the frequency range $w_{ci} << (w_{ci}w_{ce})^{1/2} << w << w_{ce} << w_{pe}$ , where $w_{ce} = e\left|\vec{B}_0\right|/m_e$ is the electron cyclotron frequency, $w_{ci} = e\left|\vec{B}_0\right|/m_i$ is the ion cyclotron frequency, $\vec{B}_0$ is the background magnetic field, and $m_e$ and $m_i$ are the electron and ion mass respectively [*Keiter*, 1996; *Boswell and Chen*, 1997]. Helicon waves occur in bounded plasmas. In free space, these waves are known as whistler waves.

The first observations of whistler waves were reported during the latter half of World War I. Soldiers spying on enemy communications heard clear tones lasting several seconds that descended in frequency from several kHz to a few Hz [*Boswell and Chen* 1997]. H. Barkhausen presented the first report concerning these descending tones in a paper titled, "Whistling tones from the earth," in 1919 [*Barkhausen*, 1919]. The physics responsible for the whistling tones was unknown until the 1930's when Hartree and Appleton developed a theory for electromagnetic waves in magnetized plasmas [*Hartree*, 1931; *Appleton*, 1932]. Booker simplified the Appleton-Hartree dispersion relation in 1938 yielding [*Booker*, 1938],

$$N^2 = 1 - \frac{w_{pe}^2}{w\left(w - w_{ce}\cos(q)\right)}, \qquad (1)$$

for the R wave, where $w = 2pf$ and $f$ is the wave frequency; $N = c/v_f = c/(w/k)$ is the index of refraction of the plasma; $w_{pe} = \left(n_e e^2/e_0 m_e\right)^{1/2}$ is the electron plasma frequency;

$q$ is the angle between the wave vector $\vec{k}$ and the background magnetic field, $\vec{B}_0$; $n_e$ is the electron density measured in units of m$^{-3}$; $c = 3.00 \times 10^8$ m/s is the speed of light in vacuum; $m_e = 9.109 \times 10^{-19}$ kg is the electron mass, and $e = 1.602 \times 10^{-19}$ C is the electron charge. For $\vec{k}$ parallel to $\vec{B}_0$, $N$ goes to infinity as $w$ approaches $w_{ce}$. Equation (1) is known as the R wave dispersion relation. The R wave is a right hand circularly polarized, electromagnetic wave that travels parallel to $\vec{B}_0$. The dispersion relationship was further simplified to consider only low frequencies and high refractive indexes to obtain [*Storey*, 1953],

$$N^2 \approx \frac{w_{pe}^2}{w w_{ce} \cos q}. \tag{2}$$

Further analysis of this dispersion relationship by Storey showed that the group velocity has a maximum of $dw/dk = w/(4w_{ce})$ [*Storey,* 1953]. This provided an explanation of the descending tones heard at the beginning of the century. Lightning strikes would generate a broad spectrum of electromagnetic waves and the waves then experience dispersion in the plasma of the magnetosphere. Higher frequencies travel along the magnetic field faster than lower frequencies, thereby arriving at the observer earlier.

The first experimental observation of a whistler wave in a laboratory plasma was reported from the ZETA plasma device in 1960 [*Gallet et al.*, 1960]. The waves propagated along the magnetic field lines of this large toroidal fusion device. Rod Boswell inadvertently continued experimental studies of whistler waves when he built the first helicon source in the late 1960's [*Boswell*, 1970]. Boswell's intention was to study ion cyclotron waves, which are the left hand polarized version of the waves described by equation (1) [*Boswell and Chen*, 1997]. The plasma source developed by Boswell (shown in Figure 1) was a cylindrically symmetric source consisting of a 5 cm diameter, 55 cm long glass tube inserted in two magnetic field coils. The magnetic field coils were capable of generating magnetic fields up to 1.5 kG. The antenna was built from a single piece of copper wire bent to form two loops approximately 16 cm long [*Boswell and Chen*, 1997]. The initial helicon plasmas were created in a background of 1.5 mTorr of argon by exciting the antenna with 600 W of RF power at a frequency of 8 MHz. In the absence of a magnetic field, a density of $1.4 \times 10^{11}$ cm$^{-3}$ was observed. The density increased to $3.8\times10^{12}$ cm$^{-3}$ on axis with a background magnetic field of 750G [*Boswell*, 1970]. Other plasma sources available at that time required many kW of power to achieve comparable densities [*Motley et al.*, 1979].

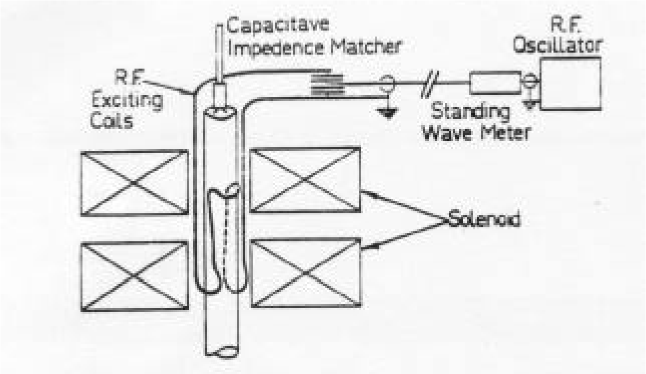

Figure 1. A schematic of the first helicon source built by Rod Boswell in the 1960's [*Boswell and Chen*, 1997].

The early experiments of Boswell and co-workers investigated the effects of magnetic field strength, chamber size and RF power on plasma density in helicon sources [*Boswell*, 1970, 1972, 1984; *Boswell and Porteous*; 1982; *Zhu and Boswell*, 1989, 1990]. Later researchers provided detailed measurements of the densities, electron and ion temperatures, and magnetic fields within helicon sources as a function of RF power, antenna configuration, magnetic field strength, and neutral pressure [*Chen*, 1991, 1992; *Chen and Decker*, 1992; *Chen and Chevalier*, 1992; *Chevalier and Chen*, 1993; *Chen et al.*, 1997; *Perry and Boswell*, 1989; *Shoji et al.*, 1993]. One characteristic of the helicon plasma source uncovered in the early Boswell experiments is the jumps in density that occur when the magnetic field is increased (Figure 2). Note that the density scales with $\left|\vec{B}_0\right|$ in the regions between the jumps. This is expected from the whistler wave dispersion relationship detailed in equation (2). Similar jumps in the plasma density have been observed as a function of RF power and driving frequency [e.g., *Keiter et al.*, 1997; *Kwak et al.*, 1997].

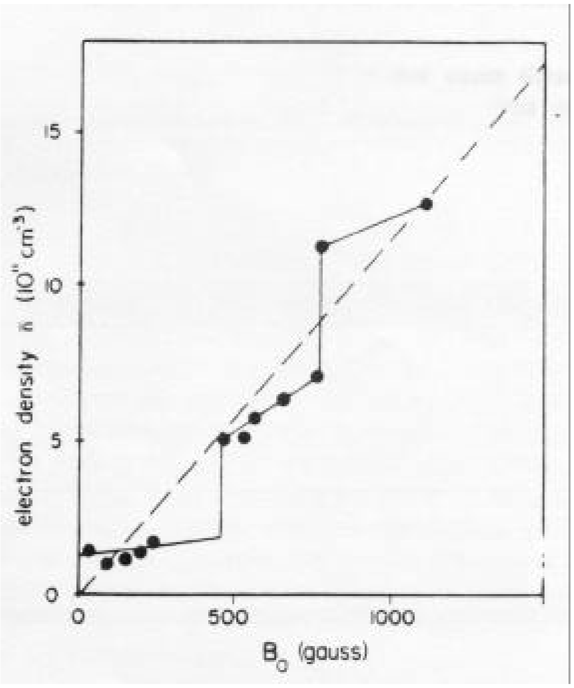

Figure 2. An example of the density jumps characteristic of a helicon plasma source [*Boswell*, 1984].

In the 1980's, helicon sources were primarily studied as a possible plasma-processing source. After a sabbatical visit to the Australian National University (ANU) in 1985, Frank Chen began research on a helicon source at the University of California, Los Angeles (UCLA) [*Chen and Boswell*, 1997]. The efficiency of the helicon source at low pressures of a few mTorr lead many to believe that helicon sources were good candidates for plasma etching sources intended for sub-micron sized feature etching [*Perry et al.*, 1991; *Chen and Boswell*, 1997; *Chen et al.*, 1997]. Other sources such as electron cyclotron resonance (ECR) sources were capable of creating comparable densities, but required operating pressures of 10's of mTorr. At such pressures, the ion-neutral collision frequency is large. Collisions in the sheath then scatter the ions during their transit to the wafer causing over-etching of trenches [*Hershkowitz and Harper*, 1999; *Lieberman and Lichtenberg*, 1999; *Conrads and Schmidt*, 2000].

The mechanism responsible for coupling RF power into helicon source plasmas is poorly understood. Chen proposed electron Landau damping of the helicon wave as a possible mechanism to explain the efficiency of helicon sources [*Chen*, 1991]. In Chen's model, electrons traveling at the helicon wave phase velocity are ideally suited to ionize argon atoms; thereby yielding enhanced plasma density production. Preliminary reports of fast electrons in helicon sources [*Chen*, 1989; *Chen and Decker,* 1992*; Lowenhardt et al.* 1991; *Zhu and Boswell*, 1991; *Ellingboe et al.*, 1995; *Molvik et al.*, 1997; *Chen and Hershkowitz*, 1998] and a model showing enhanced ionization when a fraction of the electrons become trapped between peaks in the wave potential [*Degling and Boswell*, 1997] gave credence to the Landau damping hypothesis. Recently, an energy analyzer capable of accounting for the large RF fluctuations present in a helicon source was constructed at UCLA. Using this energy analyzer, the electron distribution in a helicon source was carefully examined. Chen and Blackwell concluded that Landau-accelerated electrons are too sparse to explain the efficiency of the helicon source [*Chen and Blackwell*, 1999].

Given the weak experimental evidence for the Landau damping hypothesis, helicon research began to focus on alternative mechanisms for coupling RF power into helicon plasmas. The leading alternative candidate for helicon source efficiency is based on the coupling between helicon and slow electron-cyclotron waves. The slow electron-cyclotron wave is the other solution to the cold plasma-dispersion relationship for large perpendicular wavenumber, $k_{\wedge}$, at typical helicon source parameters [*Cho*, 2000]. These slow electron-cyclotron waves are referred to as Trivelpiece-Gould (TG) waves in the helicon literature. Initial experimental evidence for TG waves was provided by experiments that showed density peaks at specific very low magnetic field strengths (<100 G) [*Chen and Decker*, 1992; *Chen et al.*, 1996; *Chen and Chevalier*, 1992]. The possible role of electrostatic TG modes was first considered by Shamrai and Taranov when they introduced the concept of resonances and anti-resonances in a small aspect ratio helicon plasma operating at a driving frequency greater than the lower hybrid frequency, $w_{LH}^2 = w_{ce}w_{ci}w_p^2/(w_{ce}w_{ci} + w_p^2)$ [*Shamrai and Taranov*, 1994]. A resonance occurs when both the TG wave and helicon wave can exist in the plasma. Anti-resonances occur when both the TG wave and the helicon wave are evanescent. Shamrai and Taranov's calculations were consistent with the density peaks at small magnetic fields resulting from absorption of TG waves at the plasma edge [*Chen and Boswell*, 1997]. At high magnetic field strengths the TG waves are evanescent, but at low fields the TG waves can propagate throughout the plasma [*Keiter*, 1999].

## 1.2 HELICON RESEARCH AT WEST VIRGINIA UNIVERSITY

The West Virginia University helicon source program had its beginnings in an Institute of Electrical and Electronics Engineers (IEEE) meeting in Santa Fe NM in 1994. At that meeting, Earl Scime first learned of helicon sources. Noah Hershkowitz, who had a helicon source at the University of Wisconsin-Madison, encouraged Scime to build a helicon source and pursue basic plasma physics research. At that time, Scime was working in the field of space plasma physics. The next year at the Interrelationship between Plasma Experiments in the Laboratory and Space meeting in Banff, Canada, Scime realized that with a helicon source it was possible to create a high $b$ laboratory plasma to study magnetospheric plasma phenomenon. $b$ is the ratio of particle pressure to magnetic field pressure. The helicon source was ideal for generating the necessary high-density plasmas at low pressure and modest magnetic field strength. This was a departure from traditional helicon research which focused on plasma processing [*Chen*, 1994].

In December of 1994, Scime arrived at West Virginia University (WVU) and began the construction of a helicon source. The helicon source at WVU, known as HELIX (Hot hELicon eXperiment), is a large volume, steady-state source designed to operate at multiple frequencies. Historically, helicons were operated at a few select frequencies. Most experiments operated at a single driving frequency, often 13.56 MHz [*Perry and*

*Boswell*, 1989; *Chen*, 1991], or 27.12 MHz [*Sudit and Chen*, 1995]. Prior to 1997, only one helicon group reported results for two different RF frequencies in the same source [*R. T. S. Chen et al.*, 1995].

In the 1990's, helicon source groups at The Korean Atomic Energy Research Institute and at West Virginia University (WVU) began to study the effects of varying the driving frequency of helicon sources [*Kwak et al.*, 1997; *Keiter et al.*, 1997]. The Korean studies showed density jumps similar to those shown in Figure 2 when the frequency was varied rather than the magnetic field [*Kwak et al.*, 1997]. *Keiter et al.* [1997] showed that, as expected from the dispersion relation given in equation (2), over a range of frequencies the density is directly proportional to the inverse frequency. The group at WVU and at The Korean Atomic Energy Research Institute published these reports of frequency dependent effects in helicon sources nearly simultaneously. In the same work, *Kwak et al.* [1997] also reported enhanced density when the driving frequency was near the lower hybrid frequency.

A unique feature of the helicon source at WVU is the capability to non-invasively measure the ion velocity distribution function with laser-induced fluorescence (LIF). Only a few helicon research groups have had the capability to non-invasively measure ion temperatures in helicon plasmas with laser-induced fluorescence (LIF). Initial LIF measurements in helicon plasmas yielded ion temperatures perpendicular to the magnetic field from 0.06 eV up to 0.3 eV [*Nakano et al.*, 1993]. The helicon group at WVU was the first to report detailed measurements of ion temperatures in a helicon source as a function of magnetic field strength and neutral pressure. The ion temperatures of more than 0.5 eV reported from the WVU experiments were significantly higher than expected for a low temperature, high density, RF generated plasma [*Scime et al.*, 1998]. In addition, the WVU experiments also reported a significant ion temperature anisotropy $T_\perp / T_{parallel} > 1$ [*Scime et al.*, 1998]. Anisotropic ion temperatures are unusual given the high density of helicon sources. Ion temperatures of 1 eV are presented in this thesis.

Prior to these measurements, the ions in helicon plasmas were thought to be cold, i.e., near room temperature (0.02 eV) [*Nakano et al.*, 1993; *Chen*, 1998].

## 1.3 THE QUESTION OF ION TEMPERATURE IN HELICON SOURCES

Traditional models of high density, low temperature plasma sources assume that the ions are heated via electron-ion collisions [see for example *Chen*, 1998]. For electron-ion collisional equilibration the ion temperature is approximately room temperature and isotropic. The increase of the perpendicular ion temperature with increasing magnetic field (while the electron density and temperature remain constant) and the anisotropy of the ion temperature [*Scime et al.*, 1998] suggest that collisional equilibration with the hotter electrons cannot be responsible for all of the observed ion heating in helicon sources. The heating rate for ions due to collisional equilibration with electrons (including a loss term for ion energy confinement) is

$$\frac{d}{dt}\left(\frac{3n_i kT_i}{2}\right) = n_i n_E^{i/e} k\left(T_e - T_i\right) - \frac{3n_i kT_i}{t_{Ei}}, \tag{3}$$

where $u_E^{i/e}$ is the ion-electron collisional equilibration frequency [*Huba*, 1994], $t_{Ei}$ is the ion energy confinement time, and $n_i$ is the ion density. For steady-state parameters typical of the experiments reported here: $n_i = 1.0\times10^{13}$ cm$^{-3}$, $kT_e = 3.5$ eV, and $kT_i = 1$ eV, equation (3) reduces to the statement

$$t_{Ei} = 7.5\times10^{-5} \text{ s.} \tag{4}$$

The actual energy confinement can be estimated from the ratio of the stored thermal energy to the input RF power needed to obtain these plasma parameters. Assuming half of the 750 Watts of forward power used is actually coupled into the plasma, an upper limit on the energy confinement time is given by:

$$t_{Ei} = \frac{\left\langle nk\left(T_i + T_e\right)\right\rangle_{\text{Volume}}}{\text{Power/Volume}} \approx 3\times10^{-6} \text{ s.} \tag{5}$$

Since the collisional heating calculation requires an energy confinement time an order of magnitude larger, it is clear that ion-electron equilibration cannot be solely responsible for the 1 eV steady-state, ion temperatures. For an energy confinement time of $3\times10^{-6}$ s and the observed steady-state electron temperature, equation (3) predicts an ion temperature of 0.06 eV, in good agreement with the low ion temperature observations of *Nakano et al.* [1996]. In these calculations, important energy loss terms for ion cooling by elastic collisions and/or resonant charge exchange with neutrals are neglected. Inclusion of these effects would further reduce the expected steady-state ion temperature. Therefore, even if only a small fraction of the forward power (say 10%) is responsible for the observed plasma densities and electron temperatures, ion-electron collisional equilibration cannot explain the observed ion temperatures.

There have been no detailed theoretical studies of ion heating in helicon sources. However, a recent study suggests that absorption of ion acoustic turbulence in helicon sources could result in enhanced ion heating [*Akhiezer et al.*, 1998]. In a wide variety of plasma experiments, absorption of lower hybrid waves is used for ion heating [*Porkolab et al.*, 1977; *Chu et al.*, 1976; *Stepnov*, 1996; *McWilliams*, 1983]. Since several recent experiments report enhancements in plasma density near the lower hybrid frequency [*Kwak et al.*, 1997; *Yun et al.*, 1997; *Yun and Chang*, 1998], lower hybrid heating of ions may play a role in helicon sources.

As previously mentioned, the helicon source is an attractive plasma-processing device because it yields high-density plasma at low operating pressure. However, large perpendicular ion temperatures can cause over etching problems similar to those created by high neutral gas pressures. Commercial viability of the helicon source requires evidence that high-density plasmas can be generated with low ion temperatures.

The objective of the experiments presented in this dissertation is to identify an experimental configuration that maximizes plasma density while minimizing ion temperature in a helicon source. To accomplish this objective, a number of different antennas were constructed. The electron density and temperature and ion temperature created by each antenna were measured for a wide range experimental parameters. During the optimization of the helicon source, it was hoped that the dependence of ion temperature on experimental parameters might provide some insight into the ion heating mechanism. These experiments were performed in HELIX. HELIX and the diagnostics necessary for performing these experiments are discussed in chapter 2. The antennas and matching circuit used in these experiments are discussed in chapter 3. The electron density and temperature and ion temperature from the various antennas are presented in chapter 4, section 1. Magnetic fluctuations recorded by external sensing coils are presented in chapter 4, section 2. Since the helicon wavelength in the plasma is determined by the plasma parameters [*Light et al.*, 1995; *Keiter et al.*, 1997; *Ellingboe et al.*, 1996], it is expected that an antenna that matches the natural wavelength of the helicon wave will couple RF power to the plasma more efficiently. The magnetic fluctuation measurements enable comparison of the wavelength of the wave in the plasma to the antenna length. The magnetic fluctuation measurements may also provide some insight to the ion heating mechanism in the helicon source. The implications of the experimental results are reviewed in chapter 5.

## 2.0 EXPERIMENTAL LAYOUT

### 2.1 HELIX

The HELIX (Hot hELIcon eXperiment) vacuum chamber is a 1.57 m long, 0.15 m diameter, Pyrex tube with four 2.54 cm ports located 0.3 m from one end. The Pyrex tube is attached at one end to a large aluminum chamber (4.5 m long, 2 m inner diameter) through a stainless steel bellows (see Figure 3). The large chamber, LEIA (the Large Experiment on Instabilities and Anisotropies), is used for space simulation experiments. A 560 l/s turbomolecular drag pump is connected to the other end of the Pyrex chamber. Attached to far end of the large chamber are two 1600 l/s turbomolecular drag pumps. All three pumps are backed with diaphragm pumps to avoid contamination by hydrocarbons. The base pressure in the system is typically $1 \times 10^{-7}$ mTorr. The inlet for the working gas is mounted in the flange between the end of the Pyrex chamber and the 560 l/s pump. Typical operating gas pressures for argon range from 1 to 10 mTorr. For the experiments reported here, only argon gas was used.

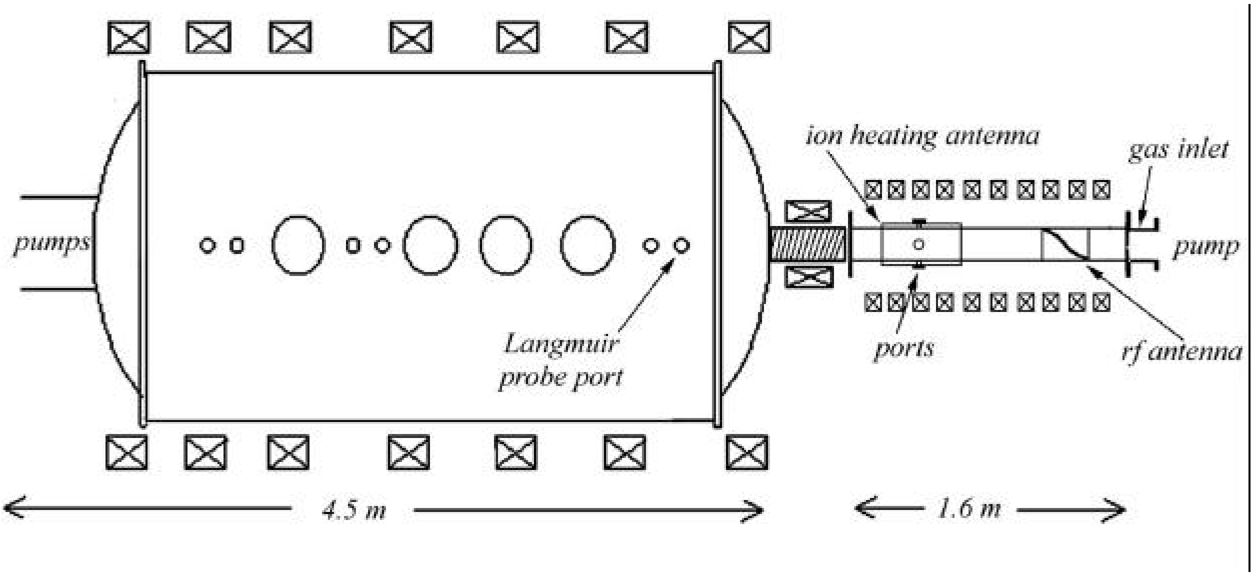

Figure 3. A schematic of HELIX and LEIA showing the position of diagnostics used in these experiments. LEIA is connected to HELIX (at right) with a bellows. Around the bellows, a coupling coil is shown. This coil was not used in these experiments.

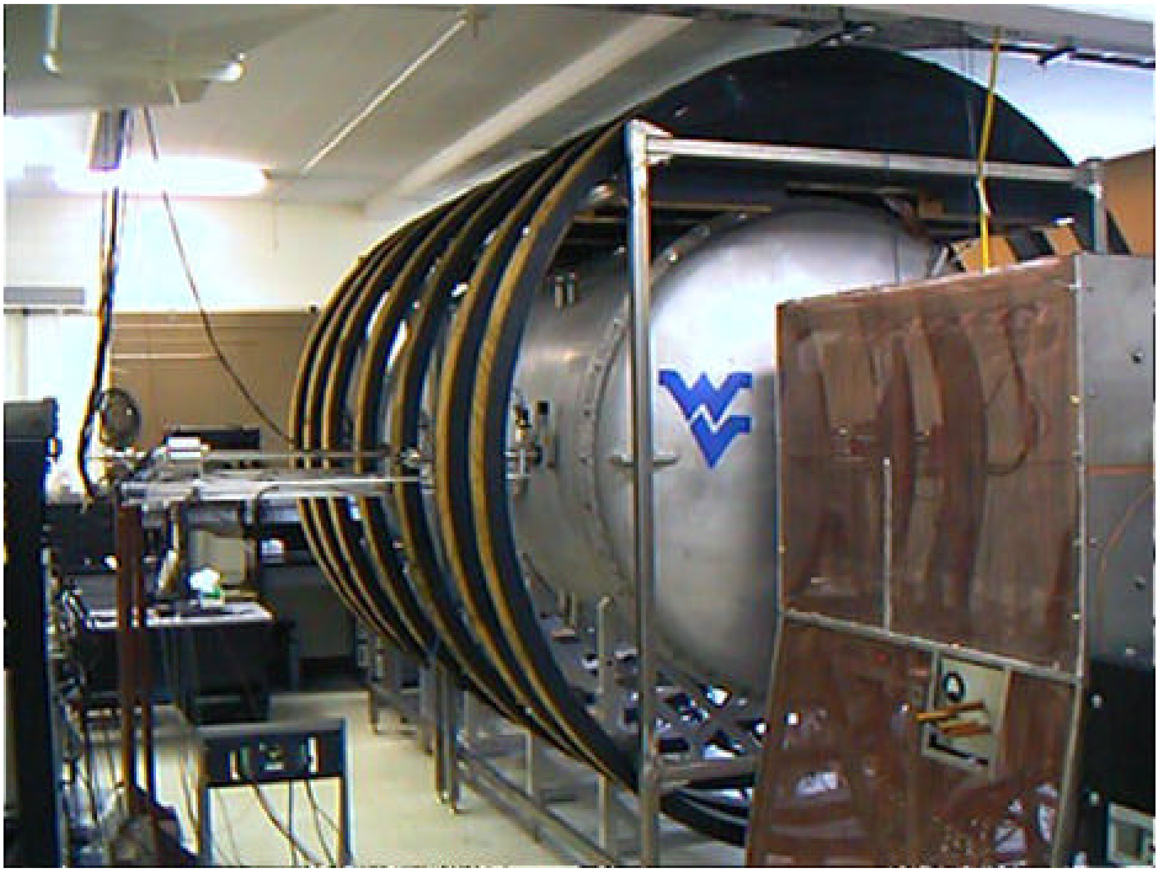

Figure 4. HELIX in the foreground connected to LEIA. The seven large electromagnets around LEIA are evident. The Langmuir probe is the first of the probes entering on the left side of LEIA.

The steady-state HELIX magnetic field is generated with ten electromagnets donated by the Max Planck Institüt in Garching, Germany. Each magnet, consisting of 46 internal copper windings with a resistance of 17 mΩ and an inductance of 1.2 mH, was originally positioned to produce a uniform axial magnetic field of 0 to 1300 G [*Keiter et al.*, 1997]. For these experiments, the second electromagnet of the set has been reversed to create a minimum-field region near one end of the RF antenna. A typical axial field profile calculated with three-dimensional magnetic field modeling code is shown in Figure 5. The code was benchmarked with experimental measurements and is accurate to within a few percent. The field-minimum configuration was selected based on past observations of increased densities with a field-minimum configuration [*Keiter*, 1999] and published reports of similar results by other helicon groups [*Chevalier and Chen*, 1993; *Guo et al.*, 1999]. The LEIA magnetic field is generated by seven electromagnets which were designed and built at WVU to create a uniform magnetic field in LEIA ranging from 0 – 70 G. For these experiments, the field in LEIA was held constant at 35 Gauss. The single electromagnet, referred to as the coupling coil in Figure 3, between the source chamber and the large chamber was not used.

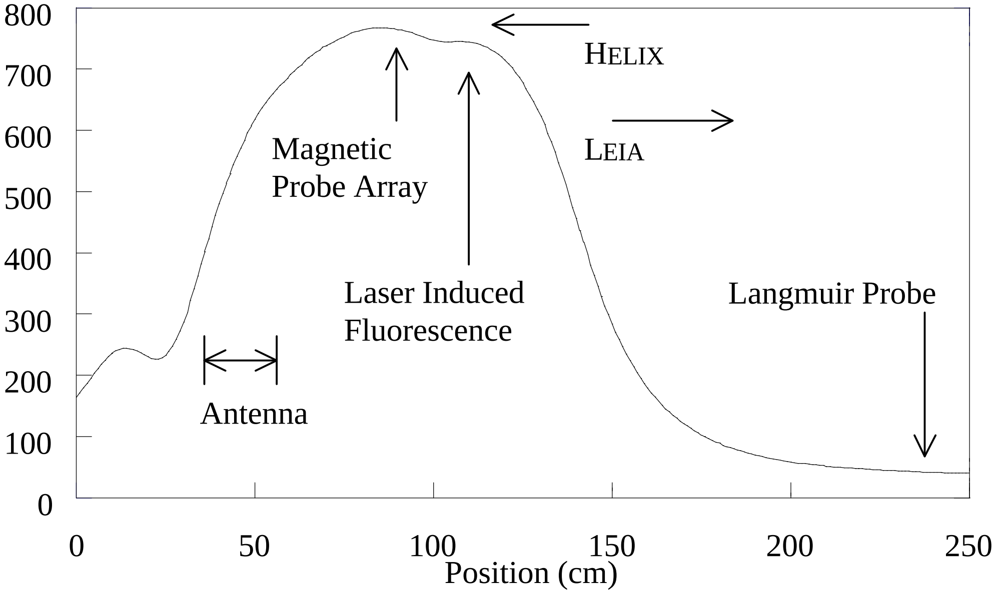

Figure 5. Typical magnetic field strength versus position in HELIX and LEIA. The position of the antenna and the diagnostics used in these experiments are indicated.

A Wavetek model-80 function generator with a frequency range of 0.3 MHz – 50 MHz generates the RF wave used to create the plasma. An ENI RF 1000 amplifier with a bandwidth of 0.3 MHz – 35 MHz amplifies the signal from the function generator. The forward and reflected power measurements and the details of the matching circuit are discussed chapter 3.0.

As shown in Figure 6, four ports on the glass tube are arranged in a four-way cross pattern. Two opposing ports are used for swept frequency (26 - 40 GHz) microwave measurements of the plasma density [*Scime et al.*, 2000]. Detailed measurements of the downstream plasma density were obtained with an RF compensated Langmuir probe placed in the LEIA chamber at the end of the source [*Keiter*, 1999; *Sudit and Chen*, 1994].

The Langmuir probe is mounted on a scanning stage for radial profile measurements of both electron temperature and plasma density. Because the magnetic field in the large chamber is only 10 - 70 G, this configuration simulates a typical plasma source connected to a large plasma-processing chamber.

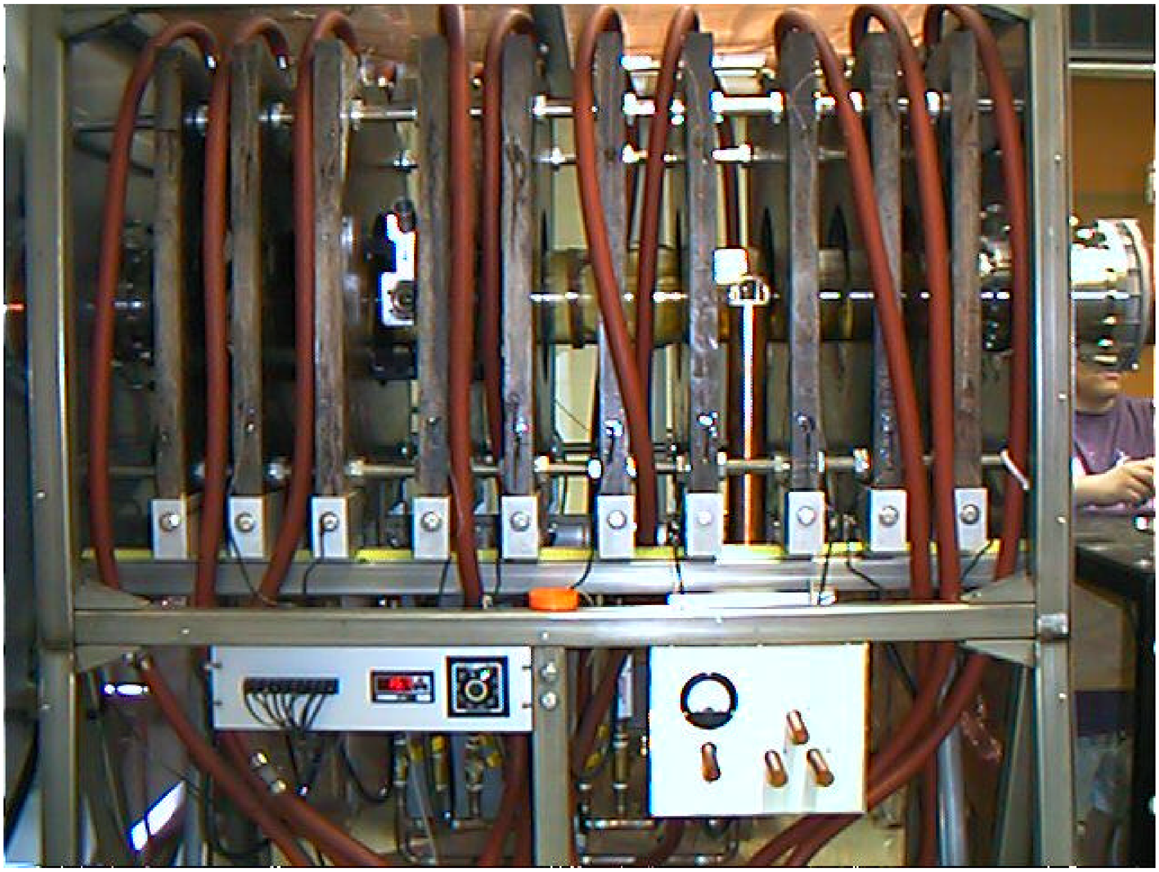

Figure 6. Photograph showing all ten HELIX electromagnets. Between the third and fourth magnets, counting from the right, are the leads to the antenna. The antenna leads are in a grounded copper tube. Below the leads is the box that contains the matching circuit discussed in chapter 3. Between the seventh and eighth magnets, the collection and injection optics for the laser-induced-fluorescence diagnostic are visible.

The typical operating parameters for HELIX are shown in Table 1. The range in magnetic field and driving frequency allow the source to operate with a driving frequency 0.25 – 1.5 times the lower hybrid frequency. Electron density and temperature, ion temperature, and magnetic fluctuations were measured over the entire frequency range, neutral pressure range of 2.5 – 7.2 mTorr, and RF power range of 300 – 750 W.

Table 1. Typical operating parameters in HELIX.

| **Parameter** | **Helicon Source (Ar)** |
|---|---|
| Plasma lifetime | steady-state |
| $n$ | $> 1 \times 10^{19}$ m$^{-3}$ |
| $B$ | 440 G - 1300 G |
| pressure | 3.2 mTorr |
| $T_e$ | ~ 5 eV |
| $T_i$ | ≤ 1 eV |
| $l_D$ | $5 \times 10^{-6}$ m |
| $r_i$ | $1 - 4 \times 10^{-2}$ m |
| $r_e$ | ~ $9 \times 10^{-5}$ m |
| $L_\perp$ (chamber diameter) | 0.15 m |
| $L_{\|\|}$ (chamber length) | 1.6 m |
| ion $b$ | ~ $4 \times 10^{-4}$ |
| $f_{\mathrm{ce}}$ | 1.2 - 2.7 GHz |
| $f_{\mathrm{ci}}$ | 16.7 - 49.7 kHz |
| $\nu_{in}$ | ~ 2.8 kHz |
| $\nu_{ii}$ | 26 MHz |
| $f_{\mathrm{pe}}$ | ~ 28 GHz |
| $f_{\mathrm{pi}}$ | 105 MHz |

## 2.2 DIAGNOSTICS

The electron temperature and density were determined with the Langmuir probe discussed in chapter 2, section 2.1. Ion temperature was measured with the LIF diagnostic detailed in chapter 2, section 2.2. The microwave interferometer described in chapter 2, section 2.3 was used to confirm that the downstream density measurements with the Langmuir probe are representative of the density in HELIX. Chapter 2, section 2.4 describes the array of fifteen magnetic sense coils used to measure the wavenumber and frequency spectrum of magnetic fluctuations at the edge of HELIX.

### 2.2.1 LANGMUIR PROBE

Langmuir probes are used extensively in plasmas to determine the electron temperature and density. A Langmuir probe is essentially a conductor that collects current when placed into plasma. The current collected by this conductor as the potential on the probe is varied is given by [*Hutchinson*, 1987],

$$I(V) = n_\infty e A_p \left( \frac{T_e}{m_i} \right)^{1/2} \left[ \frac{1}{2} \left( \frac{2m_i}{\pi m_e} \right)^{1/2} \exp\left( \frac{eV}{T_e} \right) - \frac{A_s}{A_p} \exp\left( -\frac{1}{2} \right) \right], \tag{6}$$

where $n_\infty$ is the electron density at infinity; $V$ is the potential of the probe tip relative to the plasma potential; $A_p$ is the surface area of the probe and $A_s$ is the surface area of the sheath created by the probe. The ratio of $A_s/A_p$ is a function of probe geometry, but to zeroth order this ratio is unity. The derivative of the probe current is,

$$\frac{dI}{dV} = \frac{e}{T_e} \left( I - I_s \right) + \frac{dI_s}{dV}, \tag{7}$$

where $I_s$ is the ion saturation current. The ion saturation current, illustrated in Figure 7 for a typical Langmuir probe trace, is the lowest current that the probe can draw. For the Langmuir probe trace shown in Figure 7, the source was operating at a frequency of 9.5 MHz, a power of 0.75 kW, a pressure of 3.6 mTorr, a magnetic field of 800 G in HELIX and 35 G in LEIA. Assuming $dI_s/dV \ll dI/dV$ the electron temperature is determined from,

$$T_e = e \frac{\left( I - I_s \right)}{\frac{dI}{dV}}. \tag{8}$$

Because electron saturation is not reached in typical Langmuir probe I-V sweeps for HELIX plasmas, there is a small systematic error in the electron temperature determination due to the use of the absolute probe potential in equation (8). As the electron temperature measurements play only a small role in these experiments, a more accurate $T_e$ measurement was not pursued. The electron temperature is determined from the slope of the Langmuir probe I-V characteristic in the electron retardation region. There are a number of well-known difficulties associated with this method [*Godyak et al.*, 1993], particularly in plasmas containing non-Maxwellian particle distributions. However, similar electron temperature measurements in previous experiments with this Langmuir probe were consistent with electron temperatures derived from measurements of the phase velocity of electrostatic ion cyclotron waves in the source [*Kline et al.*, 1999].

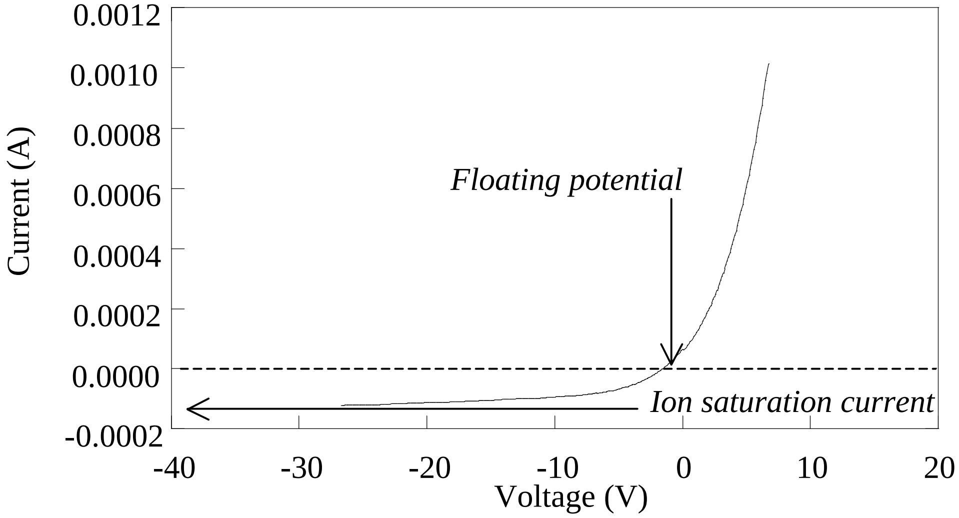

Figure 7. A typical Langmuir probe trace for a magnetic field of 800 G, pressure of 3.6 mTorr, and a power of 0.75 kW in HELIX. The magnetic field in LEIA was 35 G. The floating potential and ion saturation current are shown. Electron saturation is not reached.

The Langmuir probe developed by Keiter and Scime [*Keiter*, 1999], shown in Figure 8 and Figure 9, was used for these experiments. The I-V curve of the probe shown in Figure 7 was obtained with a Keithly 2400 sourcemeter. Although the Langmuir probe was placed downstream in the diffusion chamber and not in the helicon plasma source, the downstream measurements accurately reflect trends in the density in the Helix. A comparison of the downstream density measured with the Langmuir probe and the number of fringes observed with the microwave interferometer for pulsed operation of the source is shown in Figure 10. Each fringe from the microwave measurement represents a phase shift of $2p$ radians (roughly a density step of $3 \times 10^{12}$ cm$^{-3}$). The details of the microwave measurement are discussed in this chapter, section 2.3.

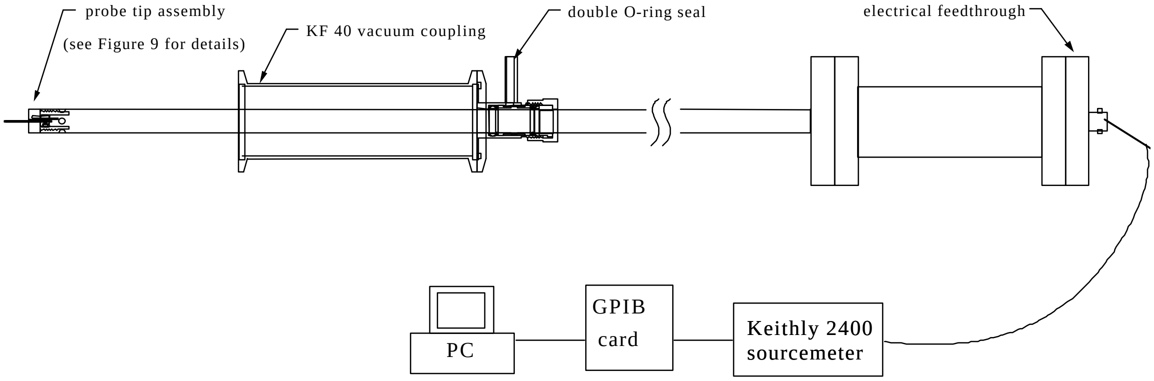

Figure 8. Schematic of the Langmuir probe and measurement circuit [*Keiter*, 1999].

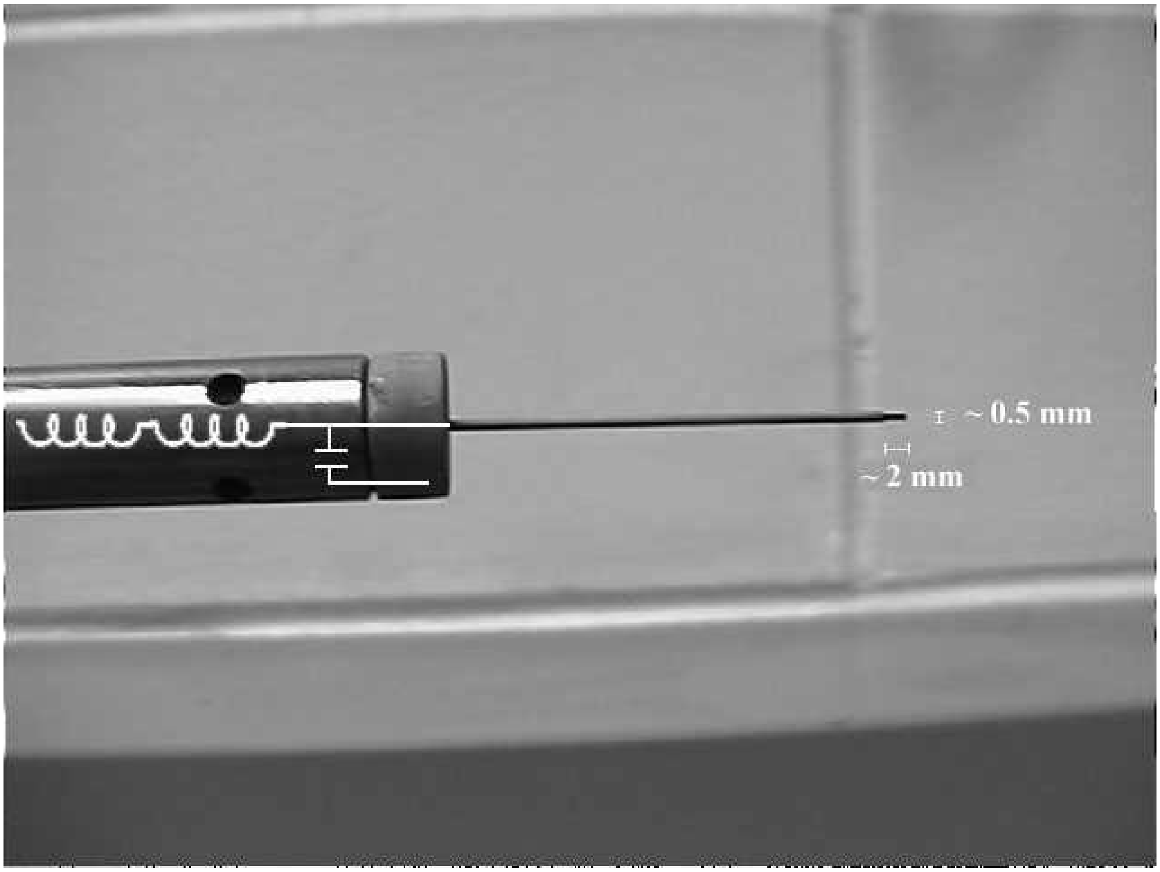

Figure 9. Photograph of the Langmuir probe head. The exposed graphite tip is 2 mm long and runs the length of the alumina tube into the boron-nitride cap. The capacitor between the graphite tip and the small secondary tip has a value of approximately 5 nF. Five inductors having values between 15 and 270 μH are placed in series behind the capacitor [*Keiter*, 1999].

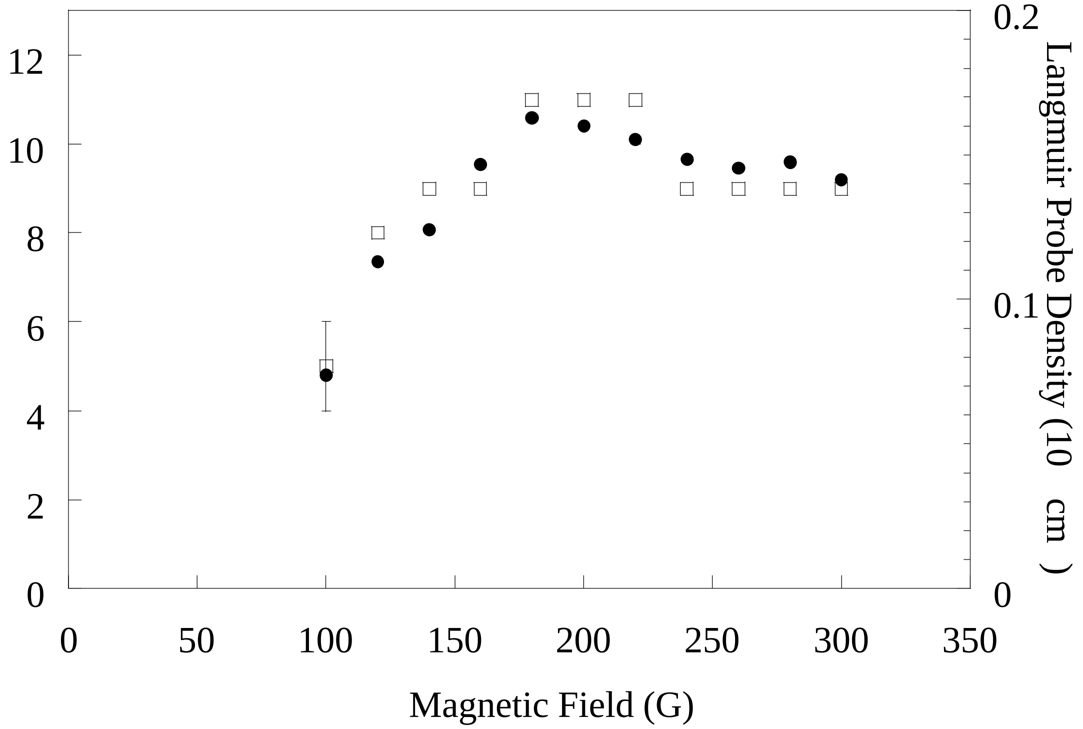

Figure 10. Comparison of the number of microwave interference fringes (open squares) for 33.6 GHz microwaves and the downstream density measured with a Langmuir probe (filled circles) during pulsed operation of the plasma source. A typical error bar representative of the statistical error in the number of fringes is shown for the 100 Gauss field data point. The statistical errors in the Langmuir probe data are smaller than the size of the data points used. Both diagnostics show the same relative changes in electron density as a function of source magnetic field strength.

Langmuir probe measurements in helicon plasmas are complicated by the large RF fluctuations in the probe sheath due to the driving wave. The RF fluctuations must be eliminated to obtain reliable electron temperature measurements. To short out high frequency fluctuations in the sheath, the Langmuir probe has a capacitor between the probe tip and a secondary tip. In series behind the primary probe tip are five inductors with values ranging from 15 μH to 270 μH. The inductors are RF chokes from Lenox-Fugle and are tuned to block a range of RF frequencies. The combination of the capacitor and inductors minimizes high frequency oscillations in the measured probe current. Langmuir probe measurements are also complicated because the probe tip becomes coated with a resistive film created by plasma deposition of residual hydrocarbons in the plasma. The coating on the probe tip affects the probe's I-V characteristic. This problem was resolved by cleaning the probe tip regularly during the experiments. A voltage of +100 V was applied to the probe tip for a few seconds. Electrons accelerated to the probe tip sputter off the resistive film.

### 2.2.2 LASER INDUCED FLUORESCENCE

The absorption and emission frequencies of an atom or ion moving relative to a radiation source are Doppler shifted by its velocity. In a typical LIF measurement, the frequency of a very narrow bandwidth laser is swept across a collection of ions or atoms that have a thermally broadened velocity distribution [*Hill et al.*, 1983]. The shift in the center frequency and the width of the absorption spectrum feature for the entire ensemble of atoms of ions is then used to determine the temperature and flow velocity of the particle distribution. The laser induced fluorescence (LIF) scheme used for measuring the ion distribution function in HELIX is depicted in Figure 11. For LIF measurements [*Stern and Johnson*, 1975; *Scime et al.*, 1998; *Keiter*, 1999] of the perpendicular ion temperature in the source, 611.5 nm laser light from a tunable ring dye laser is injected through the Pyrex vacuum chamber wall perpendicular to the HELIX magnetic field. The LIF system used in these experiments consists of a 6 W Coherent Innova 300 argon-ion laser that pumps a Coherent 899 ring dye laser. The ring dye laser wavelength is measured with a

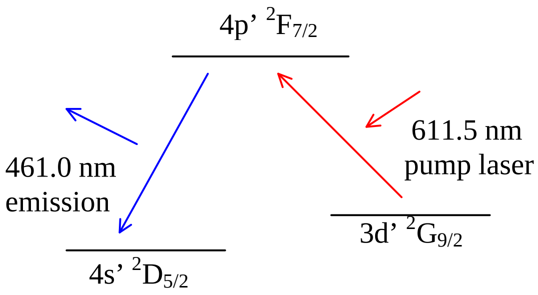

Figure 11. The argon ion LIF scheme used in these experiments. The initial state is a metastable state for singly ionized argon using the notation described in *Bashkin and Stoner* (1971).

Burleigh 1500 wavemeter. The Ar II quantum state transitions corresponding to the absorption (611.5 nm) and emission (461.0 nm) lines are $(3d^{'})^{2}G_{9/2} \rightarrow (4p^{'})^{2}F^{0}_{7/2}$ and $(4p^{'})^{2}F^{0}_{7/2} \rightarrow (4s^{'})^{2}D_{5/2}$ (Figure 11), respectively. As the dye laser sweeps through 10 GHz, roughly 0.01 nm, the fluorescent emission from the upper metastable level is measured with a filtered photomultiplier tube detector. The filter in front of the photomultiplier has a 1 nm bandpass centered on the emission line. The output of the dye laser is chopped near 1 kHz. The chopping signal is used as the reference for a Stanford Research SR830 lock-in amplifier that monitors the photomultiplier tube signal and isolates the fluorescence signal from the intense background emission at the same wavelength. The overlapping injection and collection spots localize the measurement region to a volume of 0.3 × 0.3 × 0.3 $cm^3$.

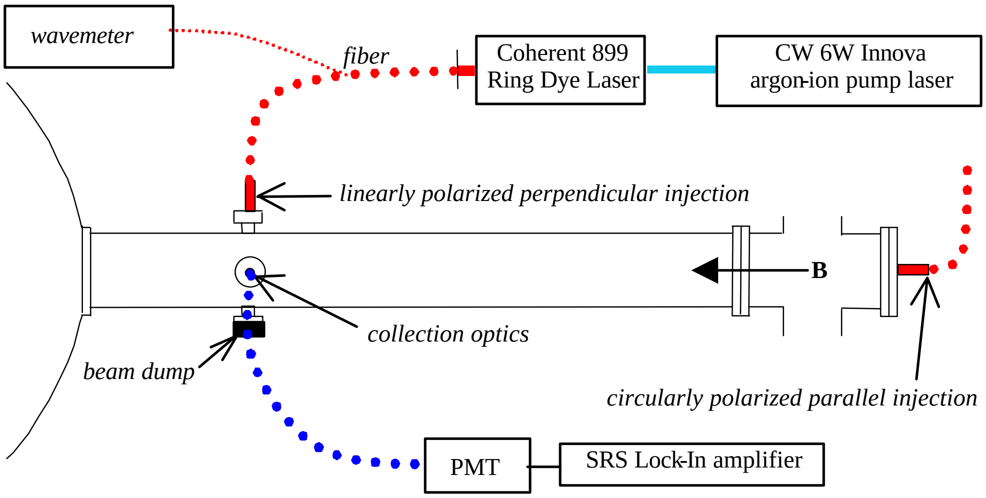

Figure 12. The experimental configuration for perpendicular and parallel LIF measurements.

The emitted light is collected perpendicular to the magnetic field through one of the four ports in the source chamber (Figure 12 and Figure 13). The injected light is linearly polarized before passing through the injection optics. Typical parallel and perpendicular ion velocity space distributions for an argon plasma are shown in Figure 14. Previous experiments [*Scime et al.*, 1998] have shown that, unless the source is operated at high pressure, the ion temperature in this source is highly anisotropic with $T_\perp >> T_\parallel$ (Figure 14).

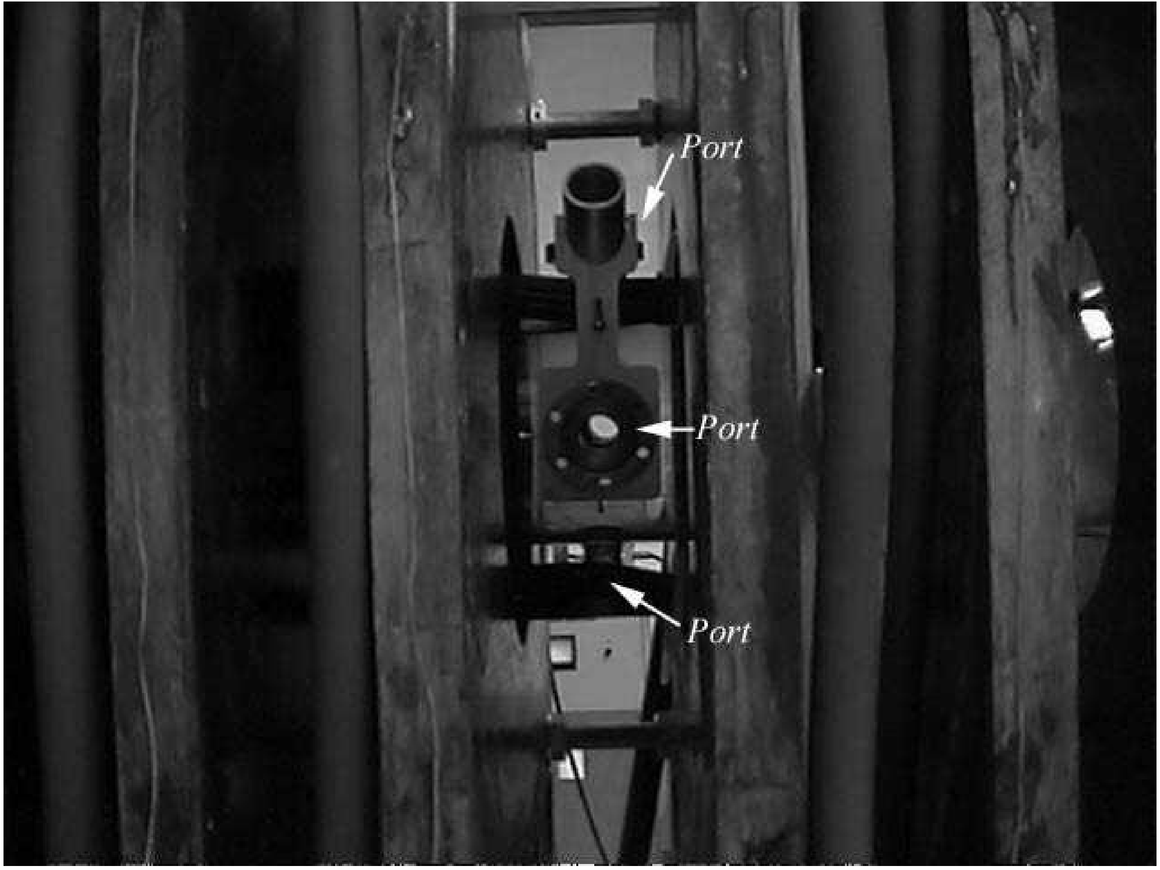

Figure 13. A photograph of the ports for laser induced fluorescence. This is the region between the seventh and eighth magnets as shown in Figure 6. This region is illustrated schematically in Figure 12.

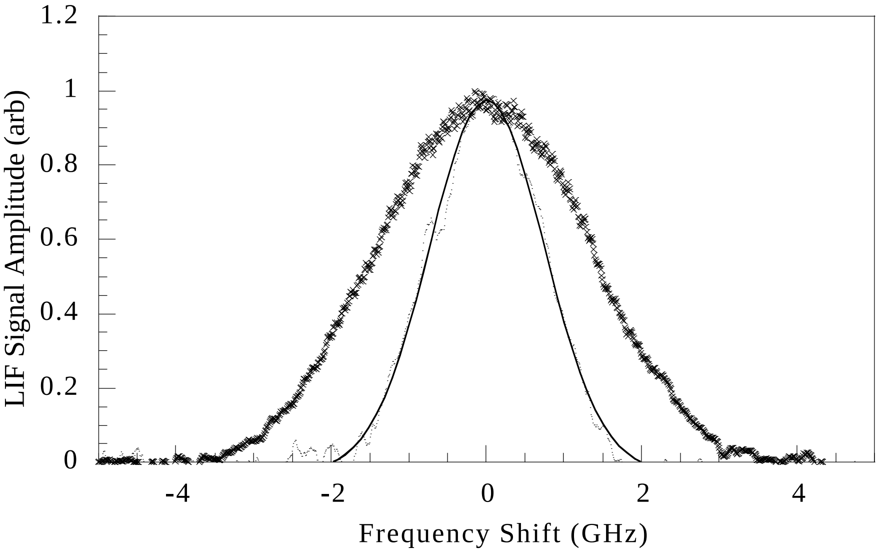

Figure 14. The parallel (dots) and perpendicular (X) argon ion velocity space distribution functions in HELIX. For this data, $T_{i\perp}$ = 0.28 eV, $T_{i\parallel}$ = 0.09 eV, and the fit to the parallel distribution function data is shown.

### 2.2.3 MICROWAVES

The microwave interferometer developed for HELIX and used in these experiments to corroborate the Langmuir probe density measurements is based on the "zebra-stripe" systems developed for pulsed plasma experiments in the 1950's and 1960's [*Heald and Warton*, 1965; *Hutchinson*, 1987]. Essentially, the zebra-stripe technique is a graphical means of counting fringes, i.e., phase shifts of 2π, that arise as the plasma density increases from zero in a pulsed experiment. At the heart of a standard zebra-stripe system is a swept frequency microwave source that is rapidly ramped through a narrow frequency band. The ramp period is short compared to the time span of the plasma discharge and the combination of a long reference leg and the frequency sweep generates a series of interference fringes or "zebra-stripes" that shift in overall phase during the plasma discharge. The zebra-stripes are due to the frequency dependent differences in time-of-flight for the microwaves between the reference and the plasma legs of the interferometer as the source frequency is varied.

The fundamental operational difference between the HELIX system and the classic zebra-stripe system is that, in a steady-state system, there is no overall shift of the fringe pattern as the plasma forms and the density increases. Instead, the overall phase shift and beat frequency of the net signal is measured with and without plasma in the plasma leg of the interferometer. The line averaged electron density can then be determined from a nonlinear fit to the frequency dependent phase shift pattern [*Scime et al.*, 2000]. In addition, the long waveguide sections used in zebra-stripe systems to generate a sufficient number of fringes from a small frequency variation are not required. In fact, in this new approach, making the lengths of the plasma and reference legs nearly equal enhances the relative effect of the plasma on the phase shift pattern. Another key feature of this diagnostic is that losses due to refraction and reflection are only significant if they reduce the transmitted signal to undetectable levels [*Scime et al.*, 2000].

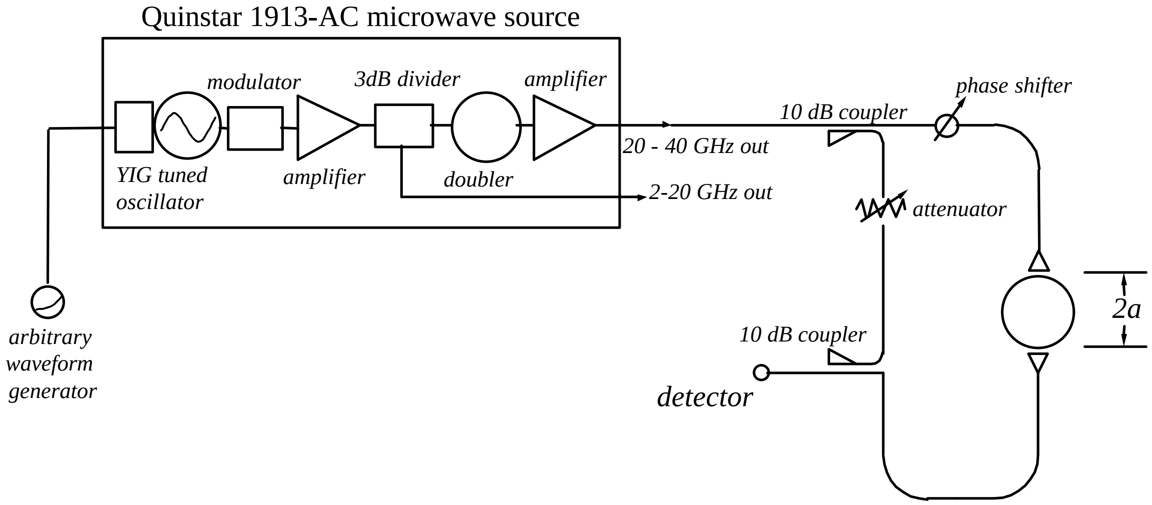

Figure 15. The geometry of the microwave interferometer system designed for HELIX [*Scime et al.*, 2000]

Given the geometry shown in Figure 15, the net time varying signal due to the superposition of each of the sinusoidal signals from each leg of the interferometer is given by:

$$M(t) = 2A\sin\left[w_m t + \frac{1}{2}\left(f_1 + f_p + f_2\right)\right]\cos\left[w_m t + \frac{1}{2}\left(f_1 - f_p - f_2\right)\right] + \\ 2(B-A)\sin\left[w_m t + f_p + f_2\right] \tag{9}$$

where $A$ and $B$ are the amplitudes of the plasma and reference leg signals respectively, $w_m$ is the microwave source frequency, $f_1$ is the phase shift due to dispersion in waveguide in the reference leg, $f_2$ is the phase shift due to dispersion in waveguide in the plasma leg, and $f_p$ is the phase shift due to dispersion in the plasma. Since the crystal detector measures time averaged power, the detector signal can be written as:

$$S(t) \propto 2A^2\cos^2\left[\frac{1}{2}\left(f_1 - f_p - f_2\right)\right] \tag{10}$$

where the signal amplitudes from each leg are assumed to be equal, $B = A$. Unequal signal strengths simply add a constant term to equation (10). The phase shifts in equation (10) are given by:

$$f_1(w) = \int_{reference\ leg} k_g\, dl,$$

$$f_2(w) = \int_{plasma\ leg} k_g\, dl, \tag{11}$$

$$f_p(w) = \int_{plasma} k_p\, dl$$

where $k_g = (1/c)\sqrt{w^2 - w_c^2}$ is the wavenumber in the waveguide, $w_c$ is the cutoff frequency in the waveguide, $k_p = (1/c)\sqrt{w^2 - w_p^2}$ is the wavenumber in the plasma, $w_p^2 = (4p\, n_e e^2 / m_e)$ is the plasma frequency, $w$ is the source frequency, $n_e$ is the plasma density, $e$ is the electron charge, and $m_e$ is the electron mass. If the plasma is pulsed on and off and the microwave frequency is held constant, the time dependent microwave signal will reflect the temporal evolution of the plasma density along the microwave system line-of-sight (Figure 16). Depending on the density profile, e.g., linear or parabolic, each fringe corresponds to a change in peak density of $3.4 \times 10^{12}$ cm$^{-3}$ or $2.3 \times 10^{12}$ cm$^{-3}$.

For these experiments, pulsed mode operation of the source combined with microwave interferometry at a fixed frequency was used to show that the trends in density in HELIX were evident in the Langmuir probe measurements performed in LEIA. A typical example comparing the trends in the Langmuir probe and microwave interferometer density measurements is shown in Figure 10. Similar results to those shown in Figure 10 were obtained for a wide range of driving frequencies and HELIX magnetic fields. For all of the antennas and parameters studied in these experiments, a similar correlation between the Langmuir probe and the microwave interferometer data was observed.

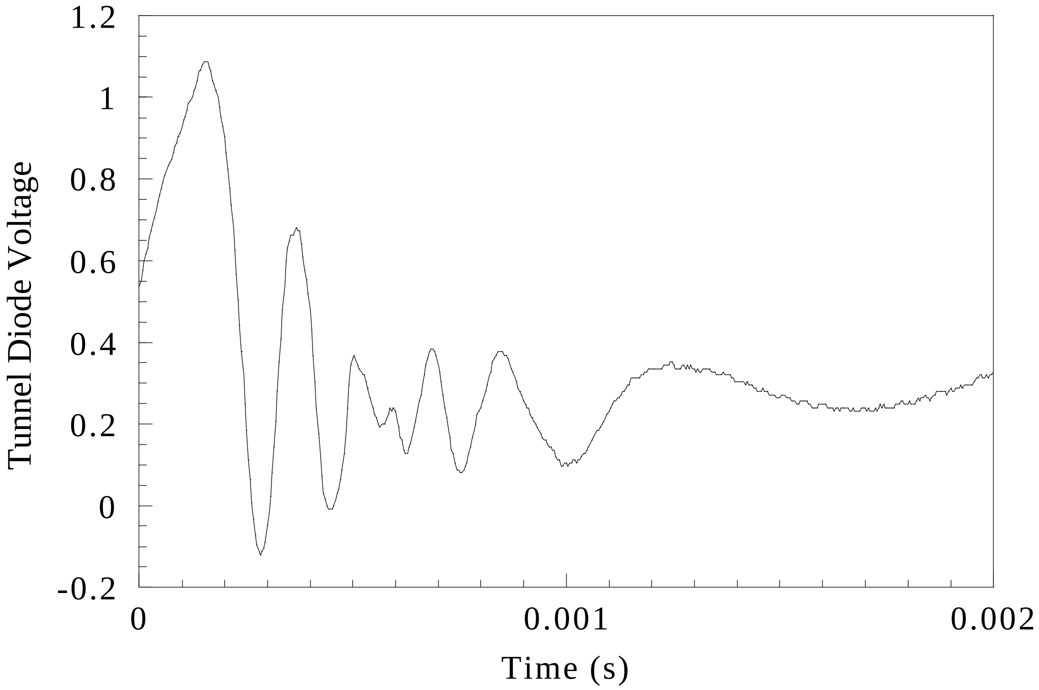

Figure 16. A typical microwave signal versus time for pulsed mode operation of HELIX. Seven full 2π phase shifts for a microwave frequency of 33.6 GHz are evident [*Scime et al.*, 2000]

### 2.2.4 MAGNETIC FLUCTUATION PROBES

Inductive magnetic loop probes, magnetic sense coils, are used to measure the frequency and wavelength of electromagnetic waves in HELIX near the RF driving frequency. Similar diagnostics are used extensively to measure magnetic fluctuations in many types of plasma experiments. The physics of an inductive probe can be explained in terms of the integral form of Faraday's law, $\oint_C \vec{E} \cdot d\vec{l} = -\int_S \dot{\vec{B}} \cdot d\vec{s}$ , where $\vec{E}$ is the electric field, and $\dot{\vec{B}}$ is the time derivative of the magnetic field. This can be simplified to yield, $V(t) = NA\dot{\vec{B}}(t)$, where *V(t)* is the voltage induced in the magnetic sense coil, *N* is the number of turns in each coil, and *A* is the area of each coil.

Although relatively simple to construct, a variety of complications arise in the implementation of inductive magnetic loop probes. The pickup of electrostatic fluctuations, also known as capacitive pickup, is a known difficulty [*Hutchinson*, 1987].

Electrostatic oscillations near the probe will cause the potential of the entire sense coil to fluctuate. If one end of the magnetic sense coil is grounded, this electrostatic oscillation will appear as a real measurement of induced åmf. Differential measurements across the coil can eliminate erroneous measurements due to electrostatic oscillations. However, at high frequencies (0.5 MHz – 50 MHz), differential measurements are problematic due to the lack of affordable and reliable differential amplifiers. Even if such differential amplifiers were available, electrostatic signals can become rectified and appear as real signals due to the capacitance and inductance of the cables between the coils and the amplifier. For this reason, electrostatic pickup should be eliminated as close to the sense coil as physically possible [*Light et al.*, 1995].

At low frequencies, some researchers shield the probe with a grounded conductor and record the signal from each end of the sense coil for later analysis [*Keiter*, 1999; *Assadi*, 1994]. This allows low frequency electromagnetic waves to reach the probe but blocks electrostatic fluctuations [*Keiter*, 1999]. This technique will not work at higher frequencies because the skin depth of the electromagnetic waves of interest becomes comparable to the shield thickness and the wave signal is strongly attenuated. With unshielded magnetic sense coils, performing every measurement twice and rotating the probe by 180° between measurements could eliminate electrostatic pickup. If referenced to a reproducible time-dependent signal, the inductive component of the signal will shift *p*-radians but the electrostatic pickup will remain unchanged [*Loewenhardt* et al. 1993]. The inductive signal is then determined by subtracting the two time series. Another technique used to eliminate electrostatic pickup involves the use of a high frequency, high-bandwidth, center-tapped transformer [*Loewenhardt et al.*, 1993; *Light et al.*, 1995]. An example of this type of magnetic probe was used by *Light et al.* [1995] to measure axial propagation of the helicon wave in a helicon source. The common mode electrostatic pickup by the magnetic sense coil, on the primary winding of the transformer, does not appear on the secondary winding of the transformer. By placing the transformer near the sense coil, excellent common mode rejection is possible for high frequency electrostatic pickup. Figure 18 shows a schematic of the coil and transformer circuit that were used for these experiments.

Additional complications arise when measuring high frequency waves (~10 MHz). Standard 50-Ω RG58 coaxial cables attenuate high frequency signals and would have performed poorly in these experiments. For these experiments, RG8 coaxial cable and high frequency connectors were used. For reference purposes, the loss per 100 meters as a function of frequency is shown in Figure 17 for RG58 cables. As can be seen in Figure 17, the losses in RG58 cables become significant around 1 MHz. The RG8 cables, however, begin to show significant attenuation at frequencies on the order of 5MHz [*Storm*, 2000].

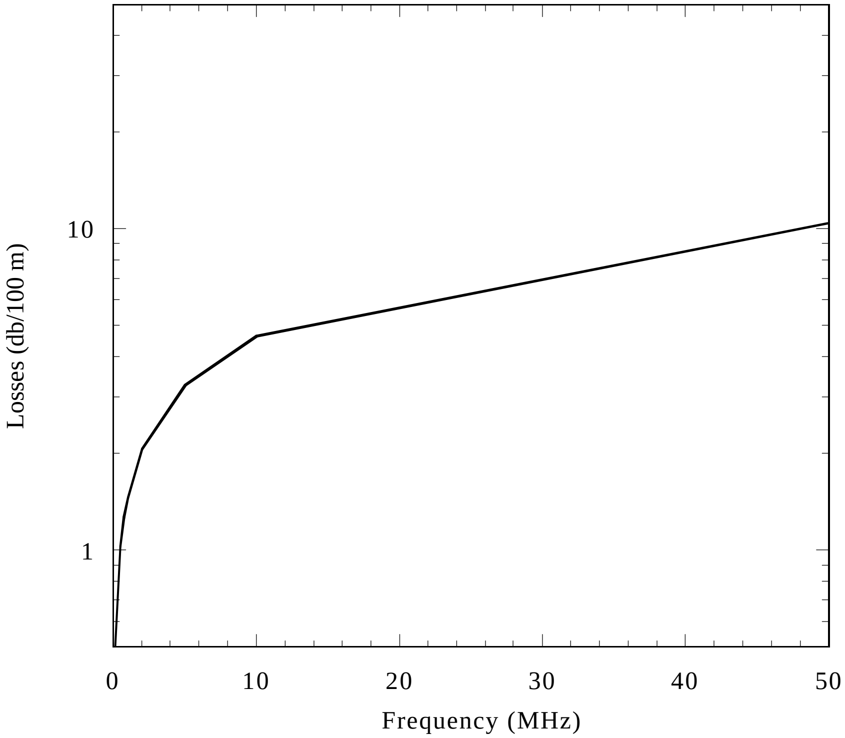

Figure 17. Loss as a function of frequency for RG58 coaxial cable

### 2.2.4.1 MAGNETIC PROBE DESIGN:

The magnetic fluctuation probes for HELIX are designed to detect fluctuating magnetic fields over the frequency range 500 kHz – 50 MHz. Each probe, depicted in Figure 18 along with the associated circuit, consists of 5 turns of 24-AWG copper-wire with a radius of 0.25-cm. The coil form for each probe is mounted directly to a grounded aluminum box containing the center-tapped transformer circuit to eliminate electrostatic pickup (Figure 19). The transformer used with the magnetic probes is a Mini-Circuits model TT1-6 with a frequency range of 0.004MHz - 500 MHz (Figure 20) and a gain of 1:1. The circuit design allows for a differential measurement of åmf induced in the coil.

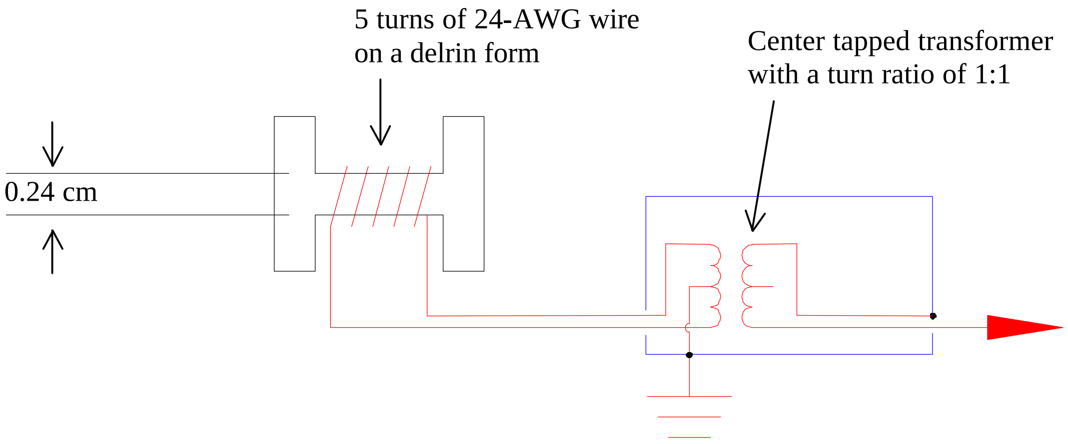

Figure 18. The magnetic sense coil and the transformer circuit. The transformer has a gain of 1:1 and the arrow indicates the cable to the digitizer which has an input impedence of 50 Ω.

There are a total of fifteen magnetic sense coils arranged to measure $\vec{k}_r$, $\vec{k}_z$ and $\vec{k}_q$ at the edge of HELIX. Three sets of four coils are located at the same axial position and measure the azimuthal dependence of $d\vec{B}_z/dt$, $d\vec{B}_r/dt$, and $d\vec{B}_q/dt$. There are four probes for each magnetic field component, spaced every 90°. Figure 21 and Figure 22 show the arrangement of the magnetic fluctuation probes around the source. A 30° offset separates the probe sets aligned to measure the different components of $\dot{\vec{B}}$. The probe azimuthal separation allows for determination of azimuthal mode numbers up to $m = 2$. Another set of three coils is positioned downstream to measure the $\hat{z}$ dependence of the fluctuating $B_r$, $B_z$, and $B_q$ magnetic fields. The distance between the coils separated in $\hat{z}$ was 4.83 cm. This allows for measurements of $\vec{k}_z$ up to 0.65 cm$^{-1}$.

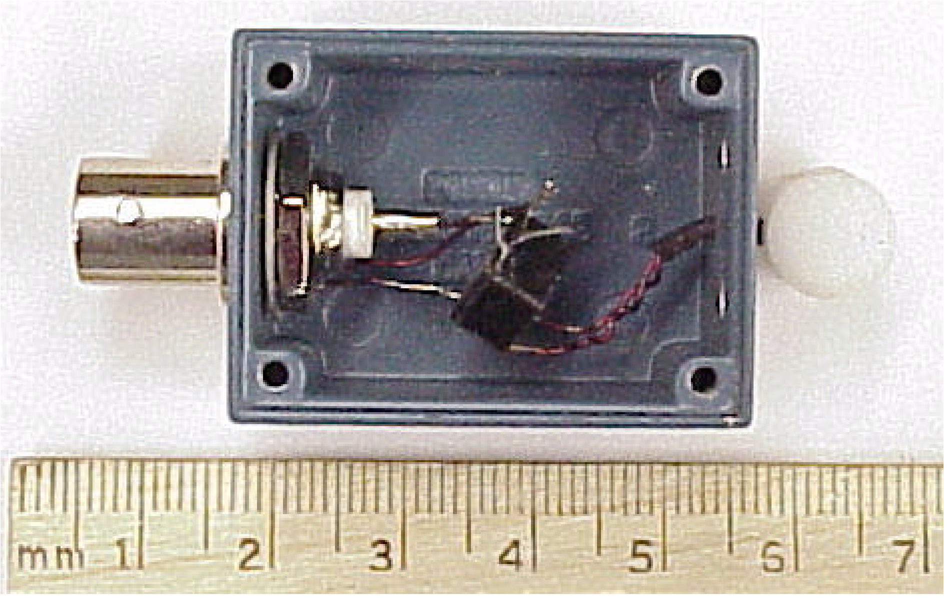

Figure 19. The magnetic sense coil and transformer assembly.

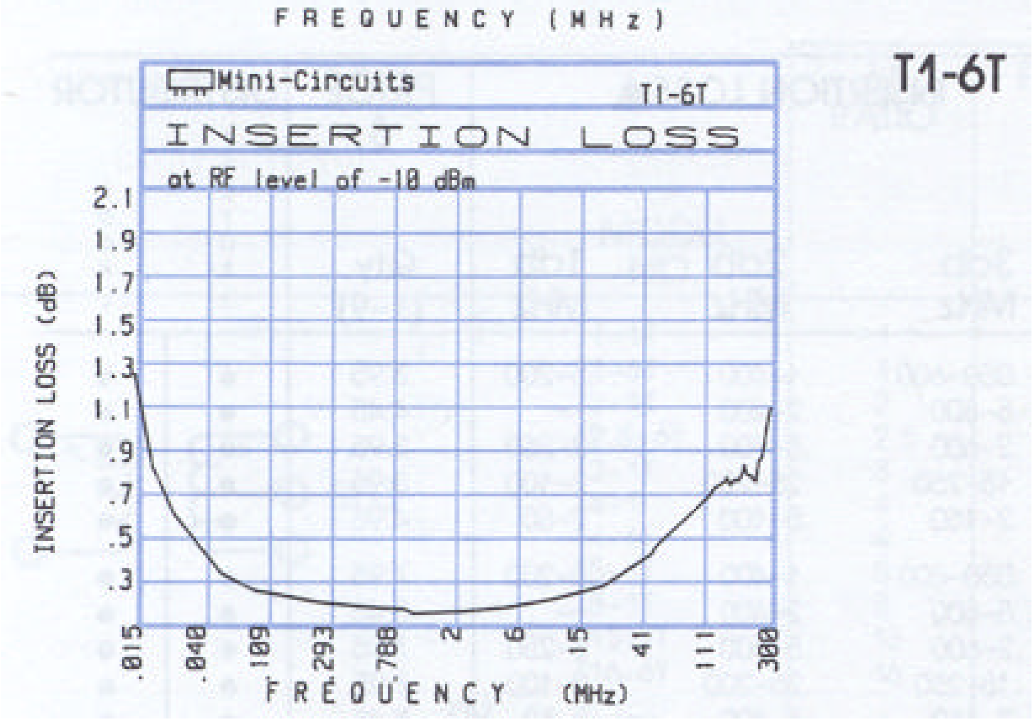

Figure 20. The insertion loss for the T1-6 transformers that were used in the magnetic fluctuation probe [*Mini-Circuits*, 2000].

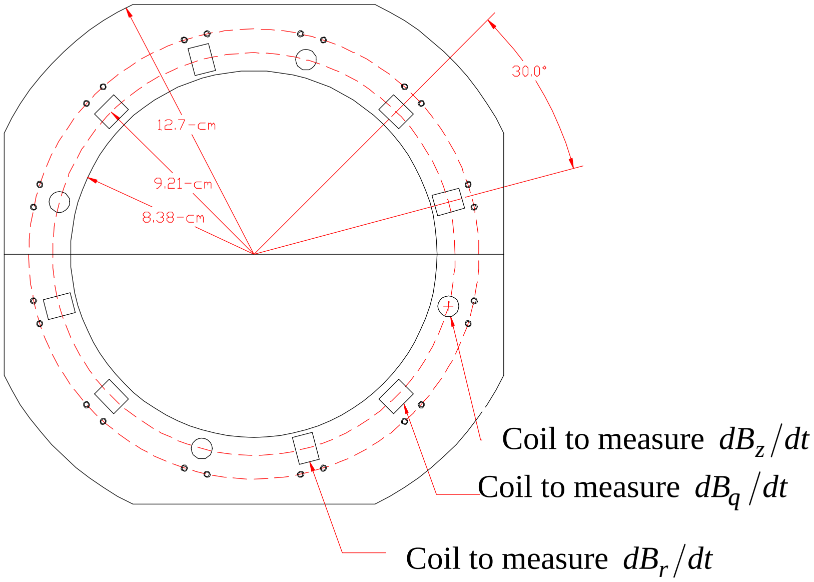

Figure 21. The ring designed to hold the magnetic fluctuation probes holds a total of twelve probes at the same $\hat{z}$ position. There are four probes separated by 90° to measure each component of $d\vec{B}/dt$. The coil sets for each component of $d\vec{B}/dt$ are offset by 30°.

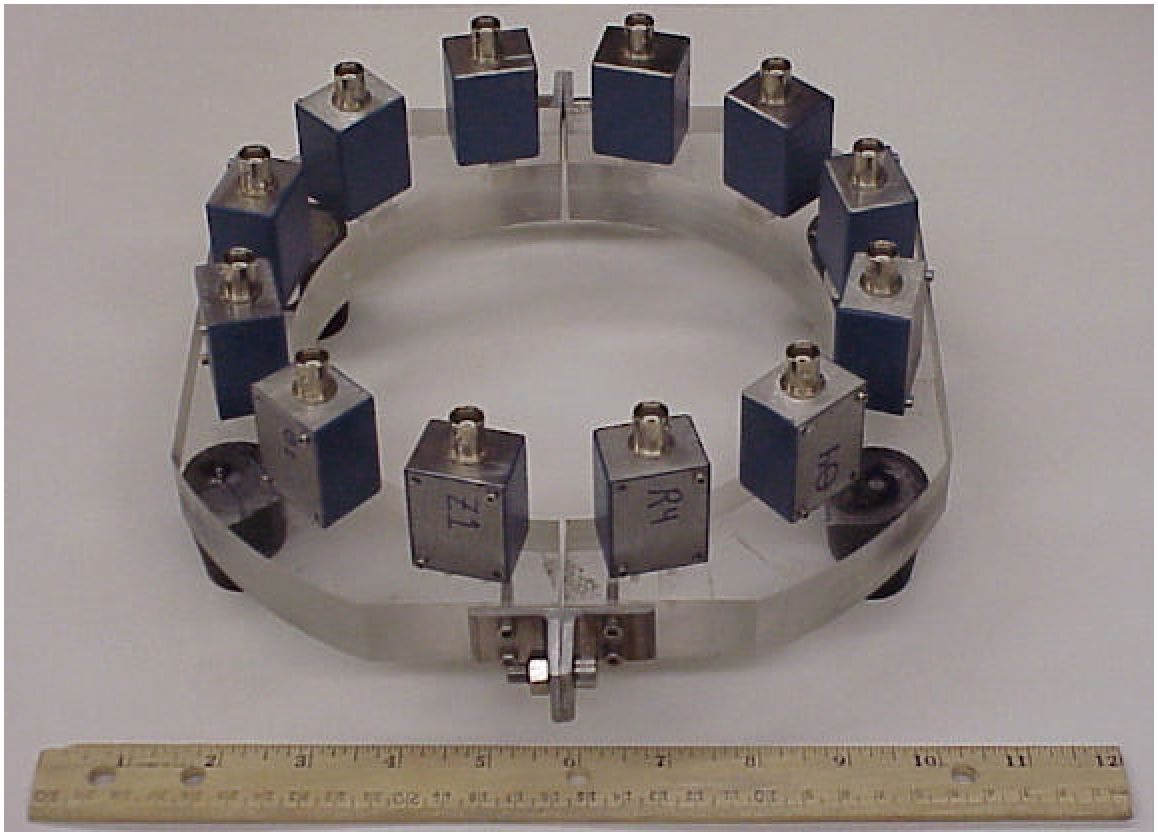

Figure 22. The magnetic probe array.

### 2.2.4.2 MAGNETIC PROBE CALIBRATION:

Every magnetic sense coil was calibrated along with the associated electronics to find the effective area and intrinsic phase shift as a function of driving frequency. The effective area replaces the term $NA$ in the equation $V(t) = NA\dot{\vec{B}}(t)$. The phase measurement is the inherent phase shift caused by the magnetic sense coil, the associated circuit, and 10 meters of RG8 coaxial cable. To perform the calibrations, a common fluctuating magnetic field reference signal was used. The reference coil constructed for the calibrations consists of 11 turns of 8 AWG wire from Industrial Electric Wire & Cable Inc., wrapped around a Plexiglas tube with a 3.8-cm inside diameter and a 5.1 cm outside diameter. The reference coil was placed in series with a 10 Ω shunt resistor and calibrated with a DC current. The magnetic field inside the coil versus the voltage drop across the shunt resistor is shown in Figure 23. The magnetic field inside the coil was measured with a Walker Scientific Inc. MG 50 Gaussmeter.

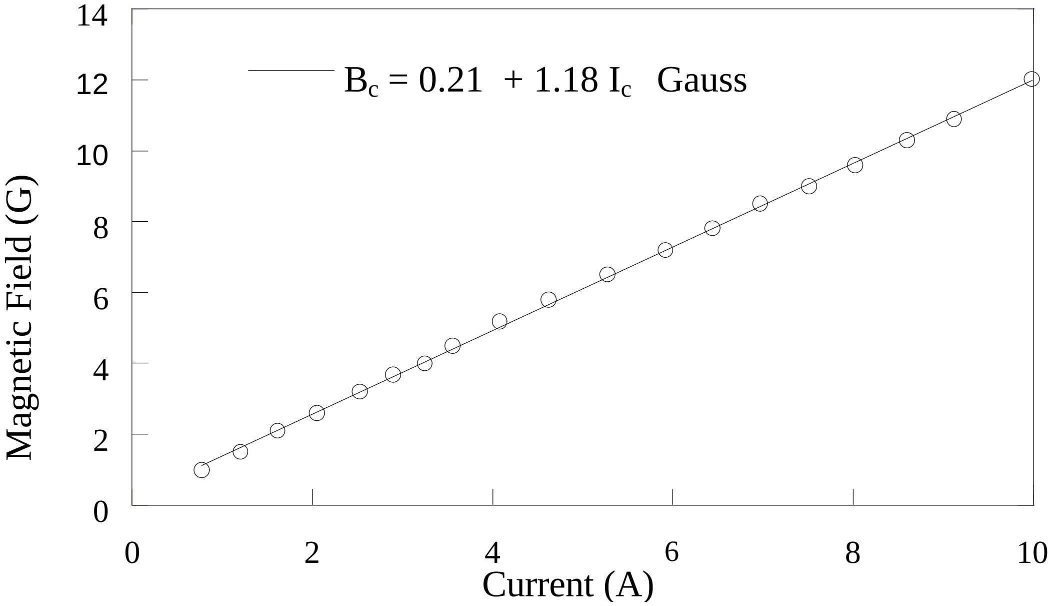

Figure 23. The magnetic field in the reference coil as a function of current through the shunt resistor. The linear fit was used to determine the magnetic field in the coil during the calibration of the magnetic sense coils.

For the magnetic sense coil calibration, each coil was placed inside the reference coil and the reference coil driven with a Wavetek model-80 50-MHz function generator.

The function generator was controlled with a PC computer through a GPIB interface. A calibration program (Appendix A) was written to command the function generator through a series of predetermined frequencies ranging from 0.5 MHz – 50 MHz. For every frequency, the voltage from the magnetic fluctuation probe and the voltage drop across the 10 Ω resistor in series with the reference coil was measured using a Tektronix TVS641 digitizer. The 5.2 μH inductance of the reference coil did cause resonant behavior in the calibration circuit. However, by measuring the reference coil current at each frequency, the resonant properties of the calibration circuit were taken into account. The calibration program then compared the two time series and calculated the effective coil area and the phase between the signals. The results of the calibrations are shown Figure 24 and Figure 25 respectively. Each magnetic sense coil was paired with a specific cable for the calibration. The same cable-sense coil pair was used during the measurements to avoid any signal phase shift that might arise as a result of differences in the cables.

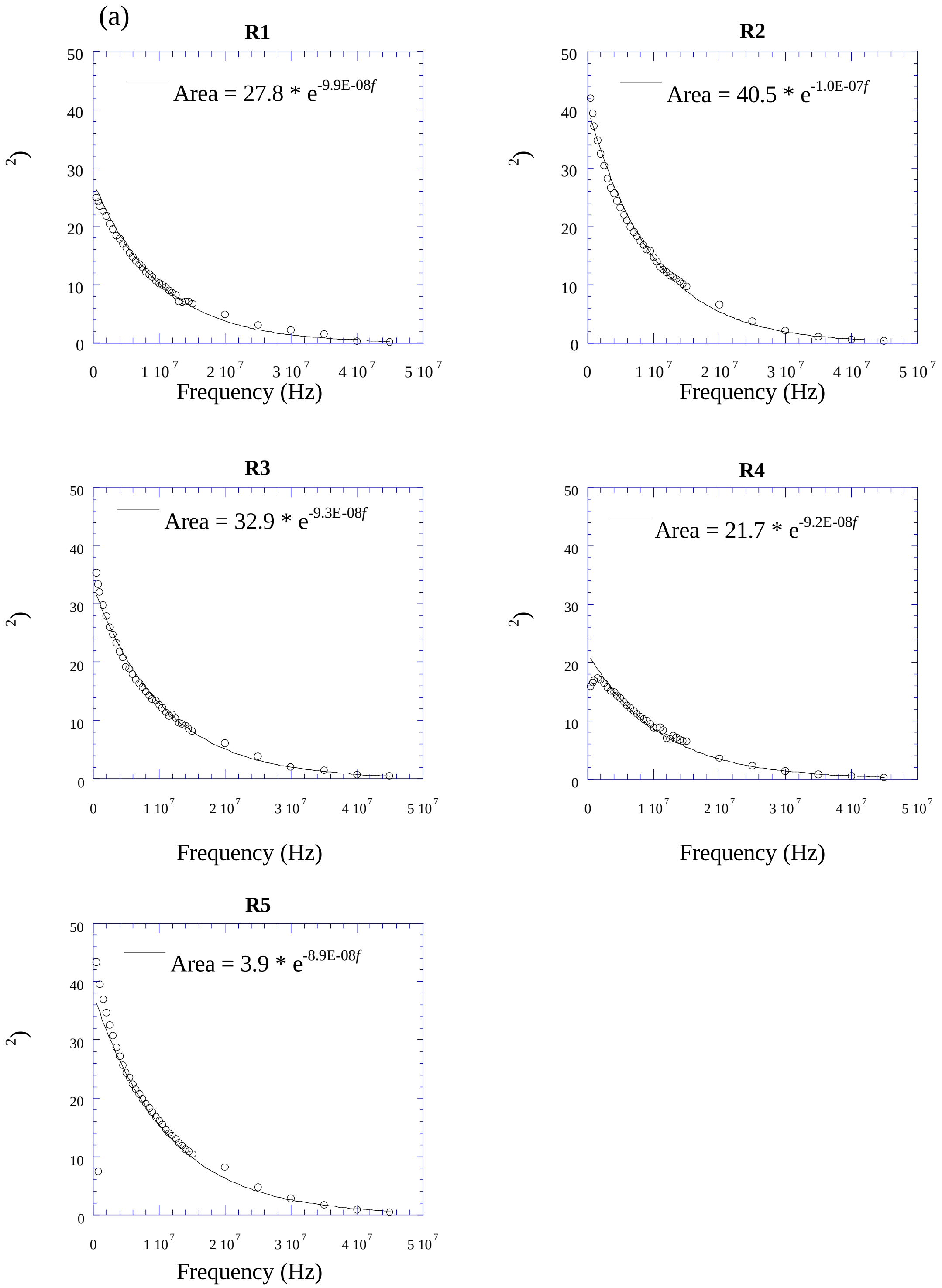
(a)
R1
Area = 27.8 * e$^{-9.9E-08f}$
R2
Area = 40.5 * e$^{-1.0E-07f}$
R3
Area = 32.9 * e$^{-9.3E-08f}$
R4
Area = 21.7 * e$^{-9.2E-08f}$
R5
Area = 3.9 * e$^{-8.9E-08f}$
2)
0
10
20
30
40
50
0
1 10$^{7}$
2 10$^{7}$
3 10$^{7}$
4 10$^{7}$
5 10$^{7}$
Frequency (Hz)

(b)

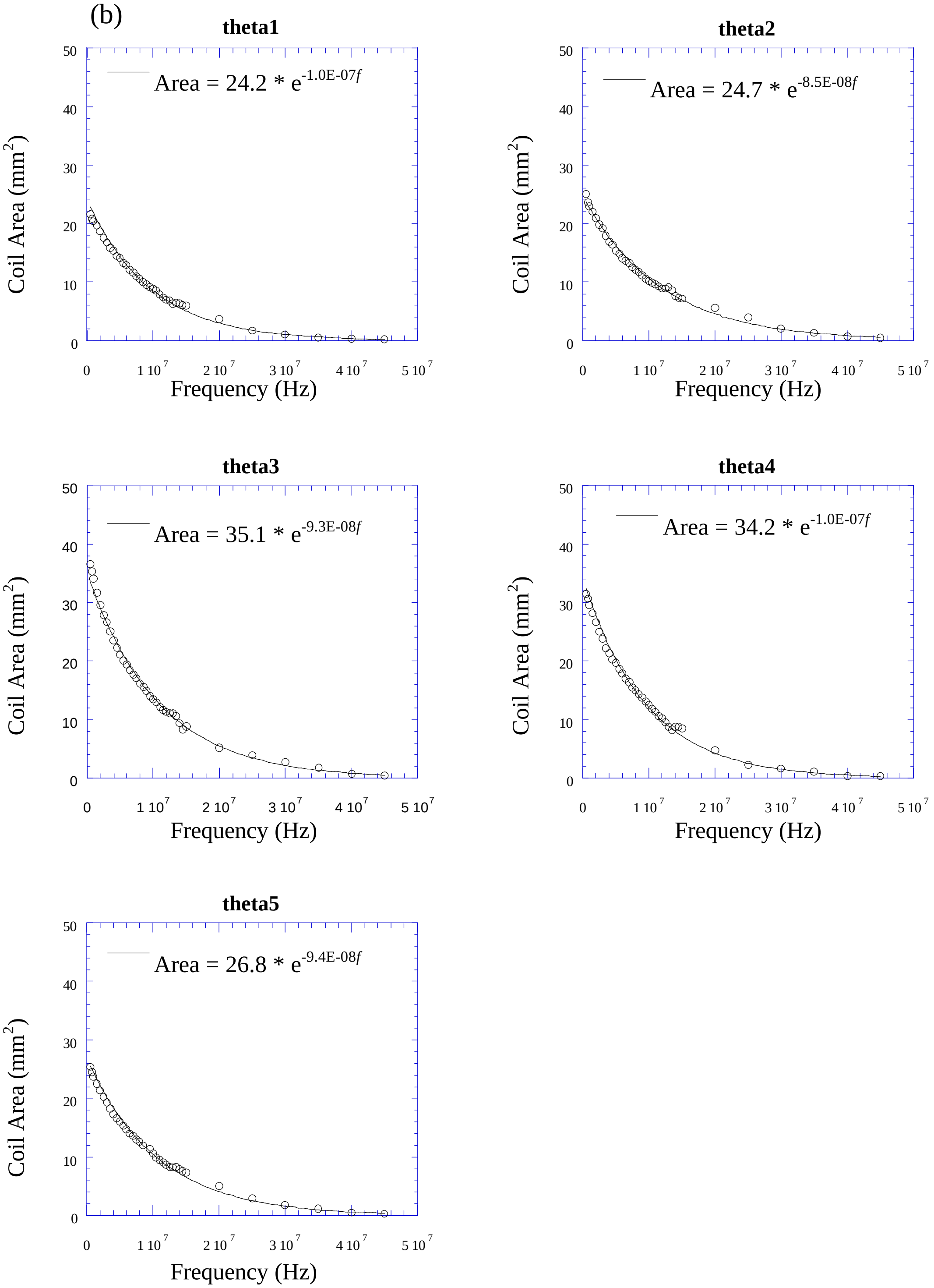

theta1
Area = 24.2 * e^-1.0E-07f
theta2
Area = 24.7 * e^-8.5E-08f
theta3
Area = 35.1 * e^-9.3E-08f
theta4
Area = 34.2 * e^-1.0E-07f
theta5
Area = 26.8 * e^-9.4E-08f
Coil Area (mm2)
0
10
20
30
40
50
Frequency (Hz)
0
1 10 7
2 10 7
3 10 7
4 10 7
5 10 7

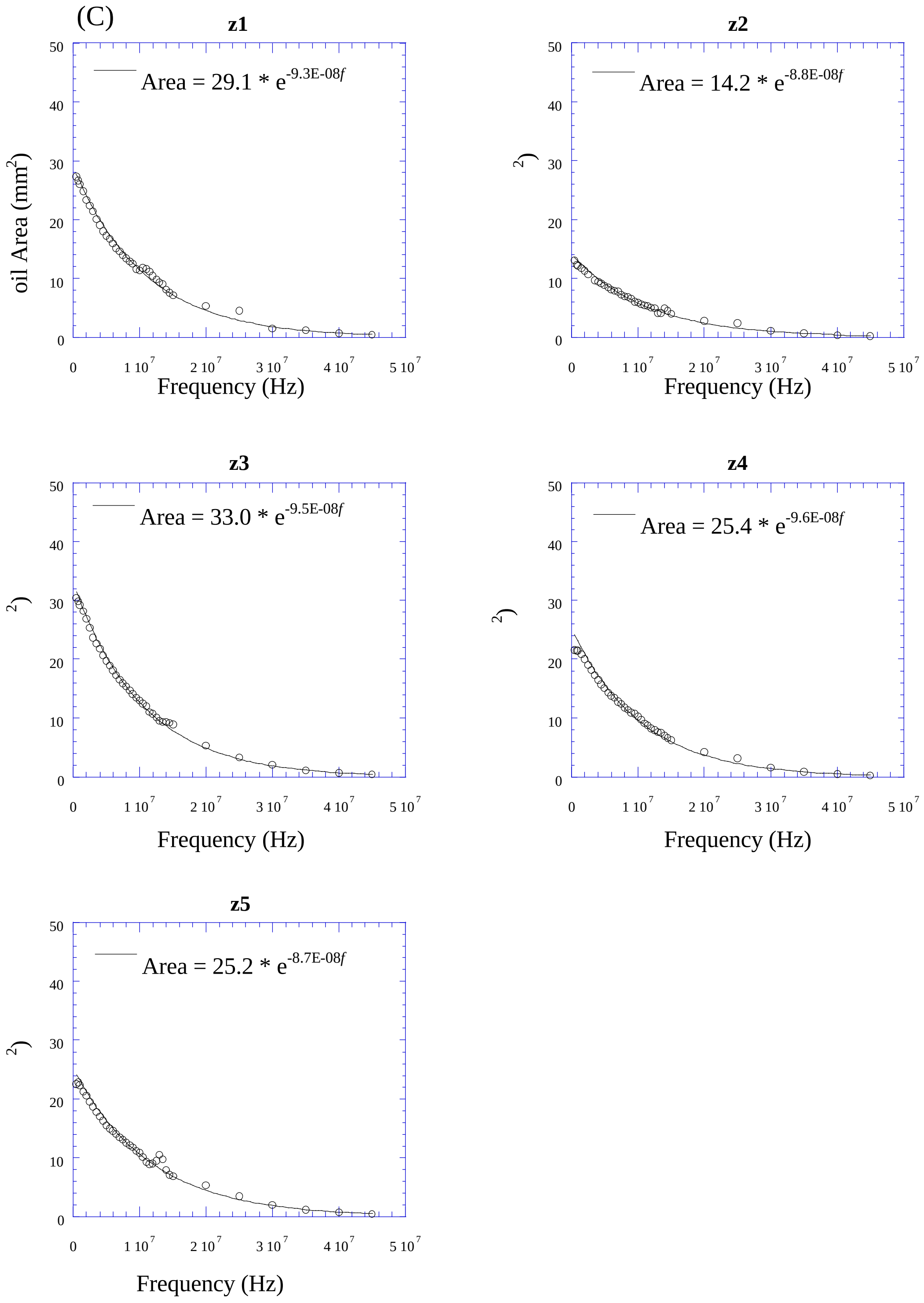

Figure 24. The effective coil area as a function of frequency for the fifteen magnetic fluctuation probes: (a) radial coils (b) theta coils (c) axial coils. Each coil labeled with the component of the wave magnetic field it measures. Probes 1-4 are located at the same axial position.

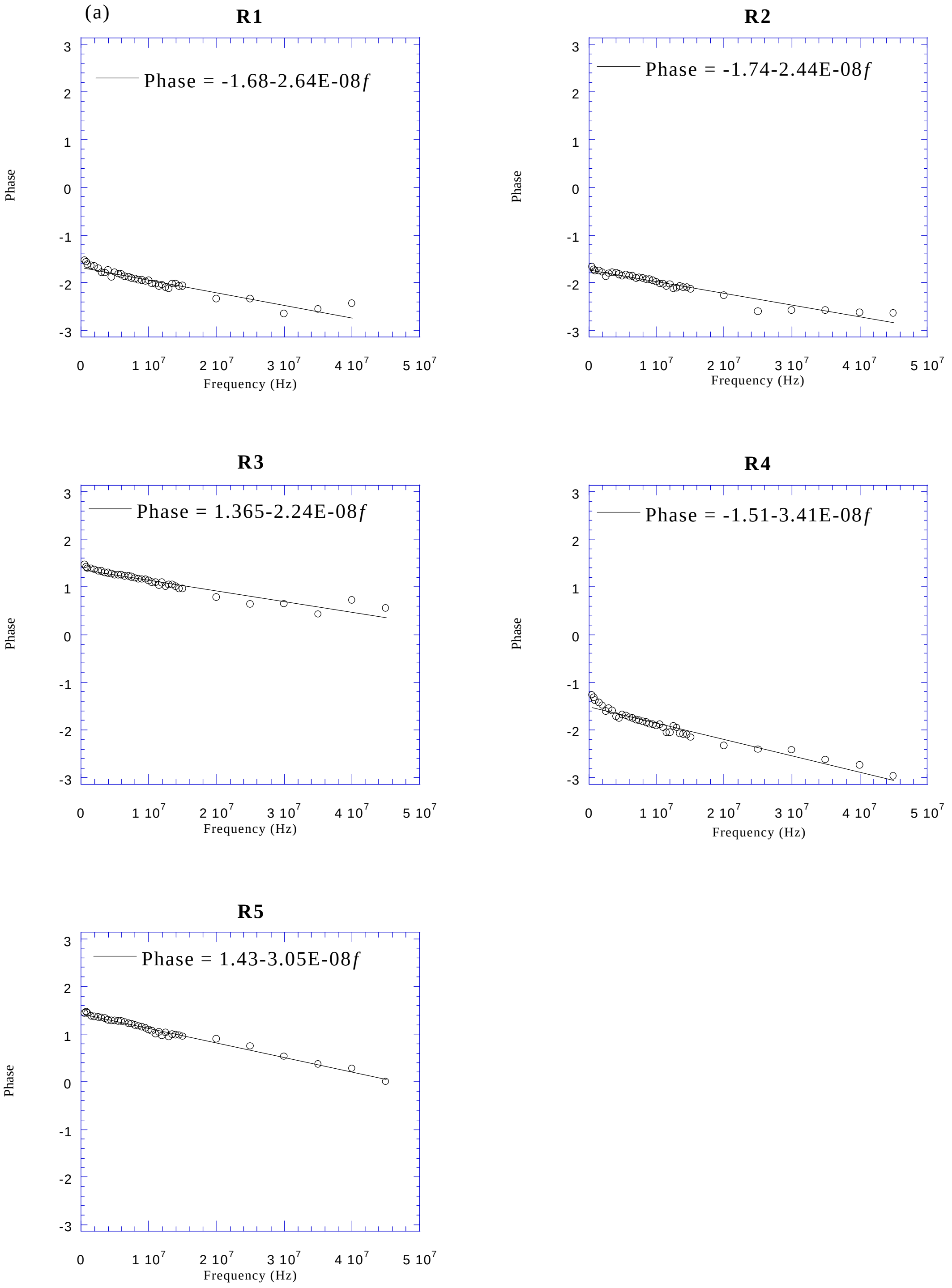
(a)
R1
Phase = -1.68-2.64E-08$f$
R2
Phase = -1.74-2.44E-08$f$
R3
Phase = 1.365-2.24E-08$f$
R4
Phase = -1.51-3.41E-08$f$
R5
Phase = 1.43-3.05E-08$f$
Phase
3
2
1
0
-1
-2
-3
0
1 10^7
2 10^7
3 10^7
4 10^7
5 10^7
Frequency (Hz)

(b)

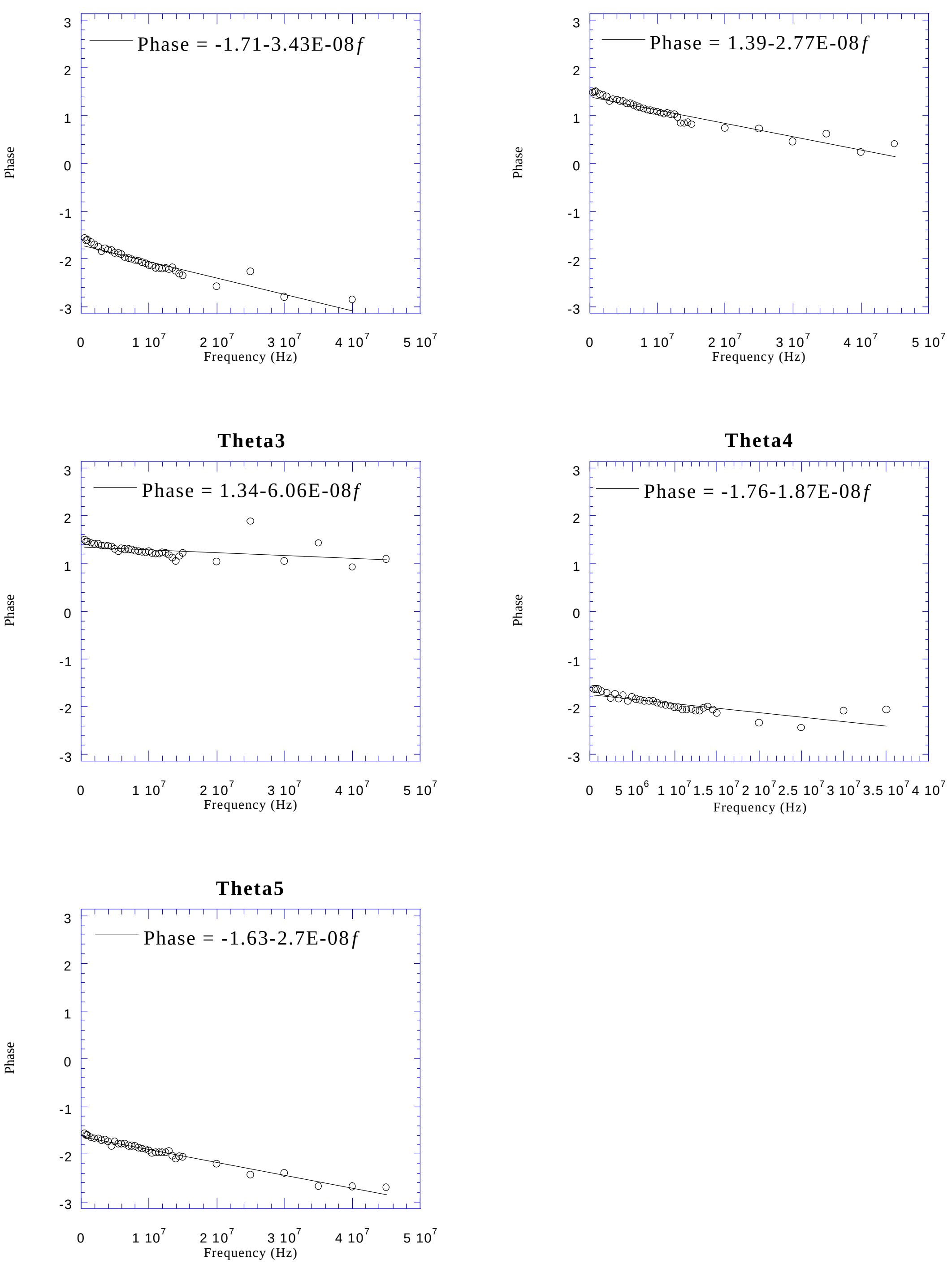
Theta1
Phase = -1.71-3.43E-08$f$
Theta2
Phase = 1.39-2.77E-08$f$
Theta3
Phase = 1.34-6.06E-08$f$
Theta4
Phase = -1.76-1.87E-08$f$
Theta5
Phase = -1.63-2.7E-08$f$
Phase
Frequency (Hz)
3
2
1
0
-1
-2
-3
0
1 $10^7$
2 $10^7$
3 $10^7$
4 $10^7$
5 $10^7$
5 $10^6$
1.5 $10^7$
2.5 $10^7$
3.5 $10^7$

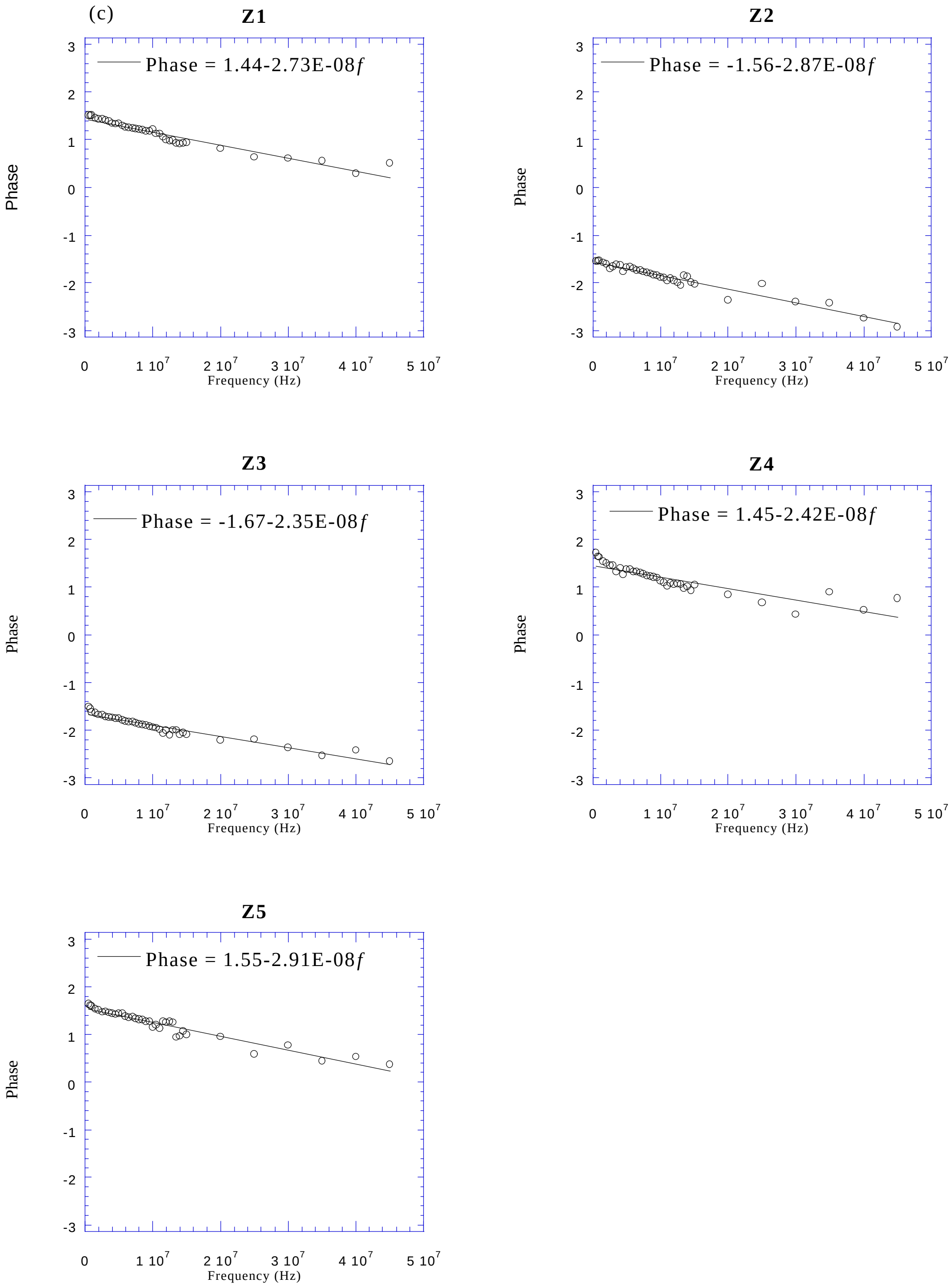

Figure 25. The effective phase as a function of frequency for the fifteen magnetic fluctuation probes: (a) radial coils (b) theta coils (c) axial coils. Each coil labeled with the component of the wave magnetic field it measures. Probes 1-4 are located at the same axial position.

### 2.2.4.3 MAGNETIC PROBE SIGNAL ANALYSIS:

Data from the magnetic probes was collected with an 8-bit Tektronix TVS641 waveform analyzer. For each measurement, 8192 points were collected at a digitization rate of 1gigasample/second. At these digitizer settings, magnetic fluctuations in the frequency range of 100 kHz – 50 MHz are temporally resolved. The general procedure required for analysis of magnetic probe signals is discussed in detail in Paul Keiter's Ph.D. thesis [*Keiter*, 1999]. However, in these experiments, a more reliable method developed by John Kline and Earl Scime was employed to correct for the inherent phase and coil area differences between magnetic sense coils. The code used to perform the data analysis in included in Appendix B.

To account for the inherent phase difference between the probes, the phase as a function of frequency for each measurement was determined from the real and imaginary parts of the FFT of the time series using the relationship:

$$\tan(q(w)) = \frac{\mathrm{Re}(\Phi(k,w))}{\mathrm{Im}(\Phi(k,w))}, \tag{12}$$

where $q$ is the phase of the signal, and $F(k,w)$ is the Fourier transformed signal. The corrected phase was obtained from the equation:

$$q_{corr} = q - q_{cal}, \tag{13}$$

where $q_{corr}$ is the corrected phase and $q_{cal}$ is the inherent phase of each magnetic probe measured during the probe calibration (Figure 25). The imaginary part of the Fourier transformed probe signal was then updated with this phase correction:

$$\mathrm{Im}'(\Phi(k,w)) = \mathrm{Re}(\Phi(k,w))\tan(q_{corr}). \tag{14}$$

The real and imaginary parts of $F(k,w)$ are then normalized:

$$\begin{aligned} \mathrm{Im}''(\Phi(k,w))_{corrected} &= \mathrm{Im}'(\Phi(k,w))\left(\frac{\mathrm{Re}^2(\Phi(k,w))+\mathrm{Im}^2(\Phi(k,w))}{\mathrm{Re}^2(\Phi(k,w))+\mathrm{Im}'^2(\Phi(k,w))}\right) \\ \mathrm{Re}''(\Phi(k,w))_{corrected} &= \mathrm{Re}(\Phi(k,w))\left(\frac{\mathrm{Re}^2(\Phi(k,w))+\mathrm{Im}^2(\Phi(k,w))}{\mathrm{Re}^2(\Phi(k,w))+\mathrm{Im}'^2(\Phi(k,w))}\right) \end{aligned} \tag{15}$$

to recover the original signal amplitude. Next, the magnetic probe signals were adjusted for the frequency dependent effective coil areas (Figure 24):

$$\begin{aligned} \mathrm{Im}\left(\Phi\left(k,w\right)\right)_{corrected} &= \mathrm{Im}''\left(\Phi\left(k,w\right)\right)\Big/\left(\frac{\mathrm{Area}(w)}{\sqrt{2}}\right) \\ \mathrm{Re}\left(\Phi\left(k,w\right)\right)_{corrected} &= \mathrm{Re}''\left(\Phi\left(k,w\right)\right)\Big/\left(\frac{\mathrm{Area}(w)}{\sqrt{2}}\right). \end{aligned} \tag{16}$$

Finally, the corrected FFT's were inverted and the phase and amplitude corrected time series for each coil were used in the wavenumber analysis routines discussed by *Keiter* [1999]. These routines described in *Keiter* [1999] use the phase shift between two probe signals to determine the two-dimensional local wavenumber and frequency spectrum, $\hat{S}_l\left(K,w\right)$, of waves in the plasma, i.e., a two-point correlation technique [*Beall et al*, 1982].

$$\hat{S}_l\left(K,w\right)=\frac{1}{M}\sum_{j=1}^{M} I_{(0,\,j\Delta K)}\left[K-K\left(w\right)\right]\times\frac{1}{2}\left[P_1\left(d,w\right)+P_2\left(d,w\right)\right], \tag{17}$$

where $P_1(d,w)$ and $P_2(d,w)$ are the power spectra for coils 1 and coils 2 respectively; *K* is the upper value of the current wavenumber bin, *jDK*; and the indicator function $I_{(0,h)}[x]$ is defined as

$$I_{(0,h)}\left[x\right]=\begin{bmatrix} 1 & 0\le xh \\ 0 & elsewhere \end{bmatrix} \tag{18}$$

*K*(*w*) has a range of $\pm p/2d$. *DK*, the bin size, is *p*/2*dM*, where $M$ is the number of points in the record and $d$ is the distance between the two probes. The power spectrum, or spectral density, of a signal is defined as:

$$P(x,w) = \frac{1}{T} < \Phi^{*}(x,w)\Phi(x,w) > \tag{19}$$

where * donates the complex conjugate and <> denotes an average over the time interval $T$. The power spectrum is essentially the square of the Fourier amplitude for a single coil timeseries, $f(x,t)$, at a single position in space.

$$\Phi\left(x,w\right) = \int_{-T/2}^{T/2} f\left(x,t\right) e^{-iwt} dt \tag{20}$$

The analysis, phase correction, and area correction algorithms were tested using fabricated signals and identical real input signals. During testing, a factor of two error in the original routines for the wavenumber calculation [*Keiter*, 1999] was found and corrected.

## 3.0 ANTENNA AND MATCHING CIRCUIT

A RF wave launched from an antenna creates the plasma in HELIX. Changes in the pressure, magnetic field, RF power and RF frequency alter the plasma and affect the load impedance of the antenna. A tunable matching circuit is necessary to compensate for any change in the impedance to prevent the reflection of RF power back to the RF amplifier. The matching circuit for HELIX is contained in the matching box shown in Figure 6. A Bird Electronics 100 W power meter at the input to the matching box monitors the reflected power. Adjusting the capacitors in the matching circuit each time a plasma parameter is changed minimizes the reflected power.

Since a key objective of these experiments was to maximize the density in a helicon plasma, minimizing RF power losses was critical. Numerous parts of the original matching circuit and antenna (Figure 26) became too hot to handle during routine operation of the source and often failed catastrophically [*Keiter et al.*, 1997]. This suggested excessive resistive losses in the circuit and antenna. Reports by helicon groups at Auburn University and the ANU of helicon mode operation at RF powers significantly lower than required in HELIX suggested that the matching circuit did not couple power to the plasma as efficiently as possible [*Boswell*, private communication; *Watts*, private communication]. Because of the thermal problems and the belief that the RF coupling could be improved, the matching circuit and antenna were reengineered prior to beginning the experiments discussed in this dissertation.

Figure 26 shows the original ***p***-matching circuit [*Keiter*, 1999]. This circuit was contained in a grounded steel box and consisted of four tunable capacitors. The load capacitor ($C_L$) was a Jennings CVCD 2000 capacitor tunable from 20 – 2000 pF. There were three tuning capacitors ($C_T$) wired in parallel. Two of the tuning capacitors were Jennings UCSL 250 capacitors tunable from 4 – 250 pF and the third tuning capacitor was a Jennings UCSL 500 tunable over the range of 5 – 500 pF. The capacitors in the matching box were connected using the center conductor removed from a military grade

RG8 coaxial cable. The outer insulator and the outer conductor were removed from the cable, but the dielectric was left on the center conductor as an insulator. Eyehooks were soldered to the ends of the RG8 center conductor facilitating easy electrical connections.

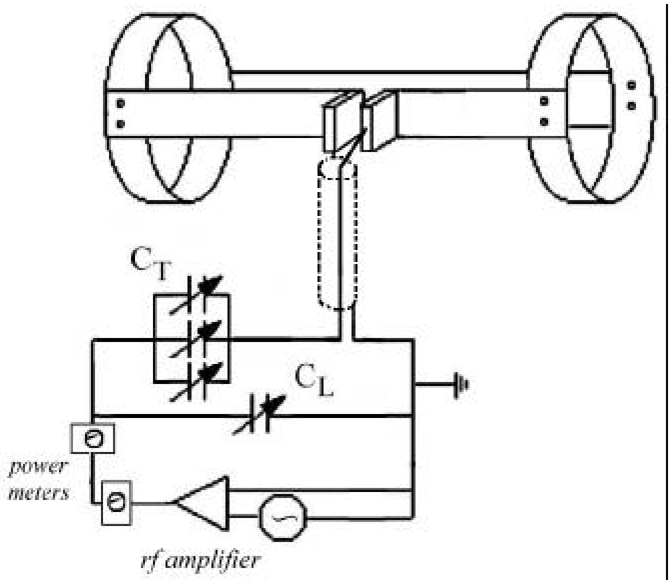

Figure 26. Original HELIX matching circuit and antenna. The connection between the matching circuit and the antenna is made with a RG8 coaxial cable. The cable shield is grounded at the box, forcing one lead to the antenna to be held at ground. The connection to the antenna is made in the center of the antenna.

The connection between the matching circuit and the antenna was made with the same RG8 high frequency coaxial cable. This cable was connected to the matching box by a type-N bulkhead connector mounted on the exterior of the matching box. In this design, the outer conductor of the cable was grounded to the matching box for mechanical simplicity. The electrical connection to the antenna was made by screwing the male type-N connector on the cable into a female type-N bulkhead connector. The center pin on the back of the female type-N fitting was soldered to the center conductor of a dismantled RG8 cable. The other end of the wire was soldered to an eyehook and attached to the antenna. The groundside of the female type-N fitting was connected to the other antenna lead in the same manner. Since the outer conductor of the coaxial cable was grounded, one lead of the antenna was fixed at ground. The antenna was constructed from six 0.03" thick, 0.75" wide copper straps. The copper straps were joined together around HELIX using #4 screws in four places.

### 3.1 MODIFICATIONS TO THE MATCHING CIRCUIT

Due to the proximity of the matching box to the electromagnets (Figure 6), the magnetic properties of the box were a concern and the steel matching box was replaced with an aluminum box. The new matching box was grounded directly to the RF amplifier, which is the sole ground for the entire experiment. HELIX is connected to this single ground point through the matching box. Having a single ground point is critical for minimizing RF pickup during these experiments.

The new matching circuit, shown in Figure 27, uses the same load and tuning capacitors as the original circuit in Figure 26. The original matching circuit had one lead to the antenna fixed at ground because of the mechanical design. The ground was moved when the circuit was reengineered so neither lead to the antenna was at a fixed potential. In this new configuration, the antenna is free to oscillate about the plasma potential. We theorized that fixing the antenna circuit to oscillate about ground limited the power coupling to the plasma. In the new circuit design, the option to replace the ground to the antenna was available if the design proved less efficient than the original circuit.

In addition to moving the ground on the circuit, every wire including the coaxial cable that connected the matching circuit to the antenna was replaced. Previously, all of the connections in the matching box were made with short sections of copper wire. In addition to the resistive losses in the wires, which limited the power available to couple to the plasma, the wires regularly failed and there was a significant possibility of damaging critical equipment during a short circuit.

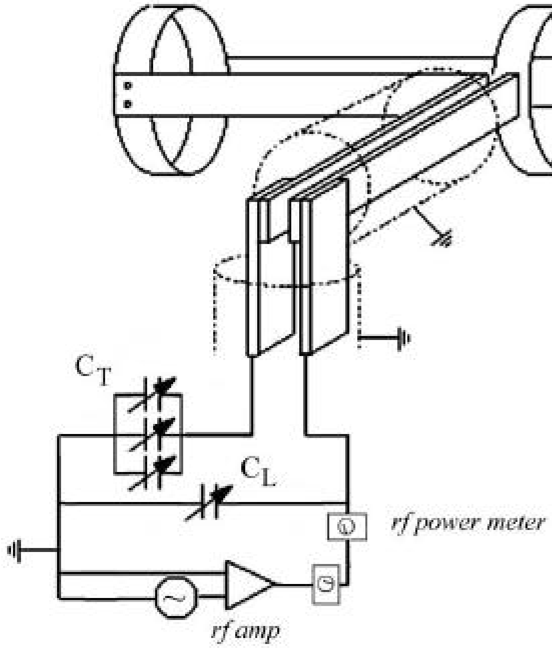

Figure 27. Modified matching circuit and antenna. The connection to the antenna is now made with copper bars and the connection to the antenna is at one end. The ground in the circuit has been moved so that neither end of the antenna is fixed at ground.

The wires inside the matching box were replaced with solid copper sheets. The capacitors were mounted on a single copper plate, represented by the ground in Figure 27. This 0.16 cm thick copper plate was mounted to the matching box using aluminum angle and stainless steel screws at four locations creating a solid ground connection. The copper plate was machined with one large hole for the tuning knob and three smaller holes for mounting each capacitor. The area around the mounting holes where the lead to the capacitor contacts the copper ground-plate was coated with silver to reduce the electrical resistance. The copper ground-plate and capacitors are clearly shown in Figure 28 and Figure 29. Phenolic knobs were machined to fit over the metallic knobs of the capacitor and extend through the ground plate and out the front of the matching box for easy adjustment. These adjustment knobs are visible in Figure 29 and are shown on the outside of the matching box in Figure 6.

The electrical lead at the back of the load capacitor was connected to another silver-coated, 0.16 cm thick copper plate. This copper plate was bent at a 90° angle allowing a direct connection to the transmission line. The input lead from the RF amplifier was silver soldered directly to this copper plate. A 0.08 cm thick copper plate was silver plated and mounted to the tuning capacitors. This thinner plate was similarly bent allowing direct contact with a transmission line. Both copper plates were coated with silver and connected to the appropriate transmission line with two stainless steel #6 screws. The copper plates, as shown in Figure 28 and Figure 29, eliminated the need for wires in the matching circuit.

The high-frequency coaxial cable with type-N connectors, that connected the antenna to the matching box, was replaced by two 2.54 cm by 0.635 cm copper bars. Silver plating was applied to the copper bar at all electrical contacts and the contacts were made over as large an area as possible. Each electrical contact was secured by at least two screws in order to ensure a low resistance connection. Figure 28 through Figure 30 show the inside of the redesigned matching box. The copper bars were separated with 2.54 cm long phenolic spacers to prevent arcing. Phenolic L-brackets were used to fasten the copper rods to the grounded matching box. Macor insulators were inserted between the copper bars and phenolic brackets in places where the conductors became hot during operation. The ceramic spacers can be seen in Figure 28 through Figure 30 on the L-brackets holding the antenna lead in place. Figure 31 shows the Teflon tube covered with a grounded copper sheet that was placed around the antenna leads to reduce RF radiation into the laboratory. The connection to the antenna and antenna design is discussed in the following section.

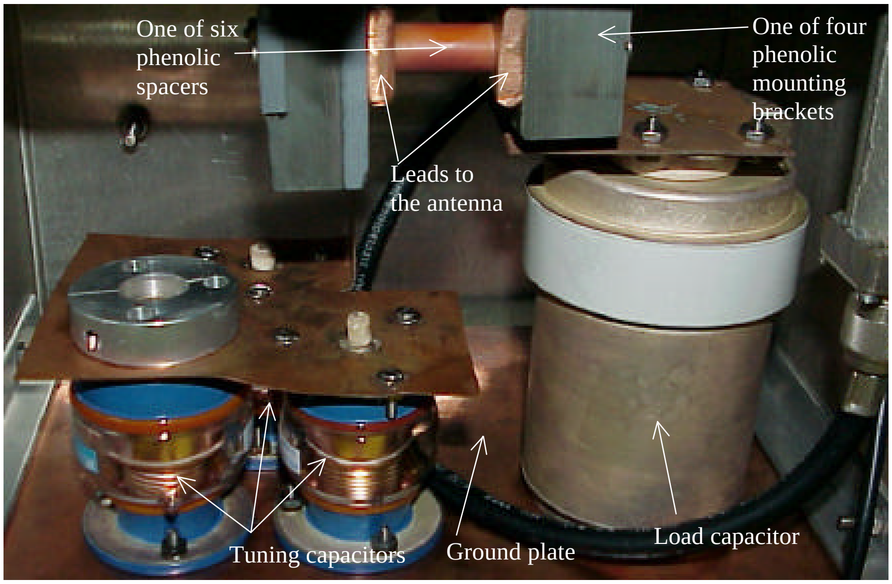

Figure 28. The inside of the matching box. All the electrical connections were made by silver plating large areas of copper and then mounting the capacitors directly to the copper.

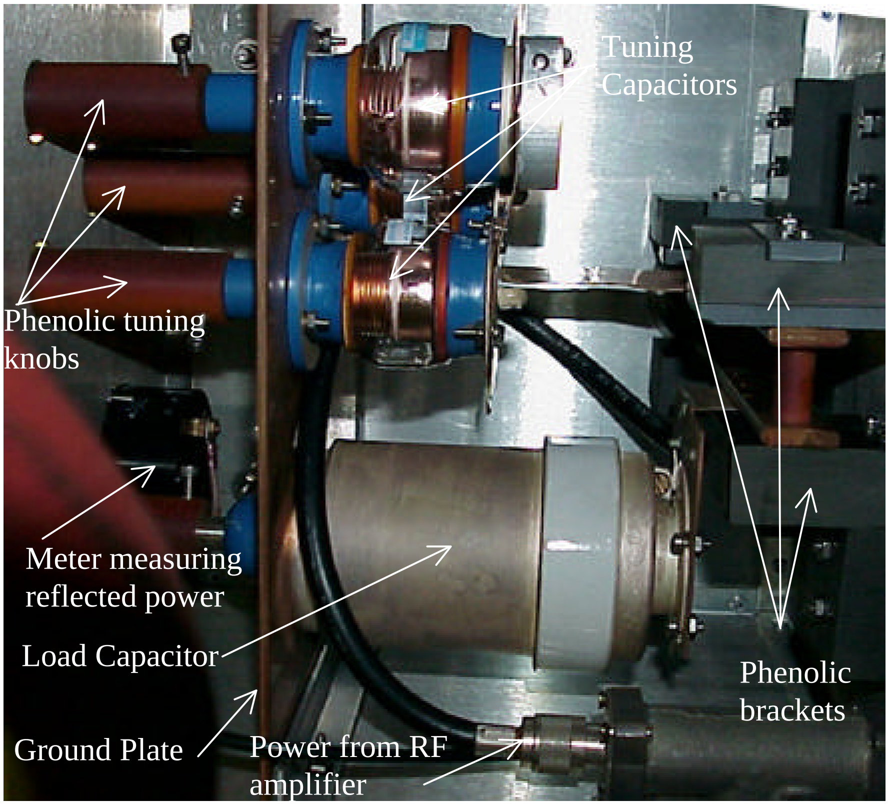

Figure 29. A view of the matching box showing the insulating rods that protrude out of the front of the box to adjust the capacitors. The coaxial cable entering from the bottom of the box is the input lead from the RF amplifier. An in-line Bird power meter in line measures reflected power between the matching circuit and the RF amplifier.

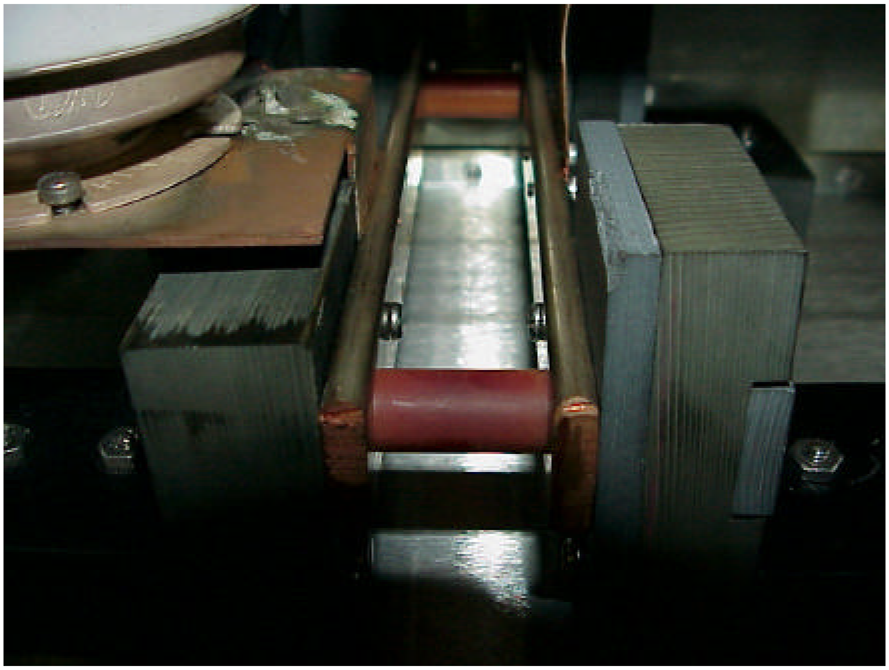

Figure 30. The transmission line to the antenna. Both leads are made of 2.54 cm by 0.62 cm copper bar. The connections to the copper rods are silver plated and joined over a large surface area to reduce resistive losses. The ceramic spacers between the phenolic block and the transmission line is visible.

Figure 31. The connection of the transmission line from the matching box to the antenna. The copper shields surrounding the antenna leads are grounded copper sheets wrapped around teflon tubing. This shielding reduces RF transmission into the lab.

## 3.2 MODIFICATIONS TO THE ANTENNA

The goal of redesigning the antenna was to couple power to the plasma more efficiently. In order to accomplish this objective, it was necessary to reduce resistive power losses in the antenna circuit. The original HELIX antenna was connected to a coaxial cable with a type-N connector through two wires attached to the center of the antenna (see Figure 26 and previous discussions). The antenna, coaxial cable, type-N connectors, and the wires to the antenna would get extremely hot during operation and could not be handled for at least an hour after the source had been turned off. The dielectrics in the cable and particularly in the type-N connectors routinely failed and caused short circuits in the antenna circuit.

The new antennas were machined from a single copper sheet. The old antenna was constructed by screwing six pieces of copper together at four different locations. Another flaw in the original design was an unfortunate lack of rigidity. Helical antennas did not maintain a fixed shape around the source. Over time, the connections around the source became loose and the antenna would gradually unravel. Detailed experiments involving different antennas were not feasible because an antenna could not be removed and later replaced in the same configuration. The new antenna design eliminated the need for many of the connections, which decreased the resistance, and prevented unraveling of the antennas.

Five new antennas were designed and tested with the above modifications. Three of the antennas were 19-cm long versions of the $m = 1$ (helical twist) antenna, one was a double-saddle, and one was a Nagoya III. The magnetic field direction was chosen so that the helical rotation of all of a $m = 1$ antennas was in the right hand direction along the field, i.e., the helical antennas are $m = +1$ antennas. The three $m = +1$ and the double-saddle antennas were constructed of 0.16 cm thick copper. The thicker copper was chosen to further limit the resistive loses inherent in the previous antenna design. The

Nagoya III was constructed of 0.051 cm thick copper. Two of the *m* = +1 antennas have 1.8 cm wide straps; one is 30 cm long and the other is 19 cm long. The other 19 cm *m* = +1 antenna, the Nagoya III and the double saddle antenna have 2.54 cm wide straps. A 2-dimensional CAD drawing of the 30-cm *m* = +1 antenna is shown in Figure 32. A similar CAD drawing was produced for each of the new antennas. Care was taken with each of the *m* = +1 antennas to guarantee the antenna would have the appropriate azimuthal shape after being wrapped around the glass vacuum chamber. After the CAD drawing for an antenna was complete, the pattern was transferred to a copper sheet for cutting with a jigsaw. The holes used for joining the antenna around the source were drilled and then the transmission line used to connect the antenna to the matching circuit were then both mechanically attached and silver-soldered onto the antenna.

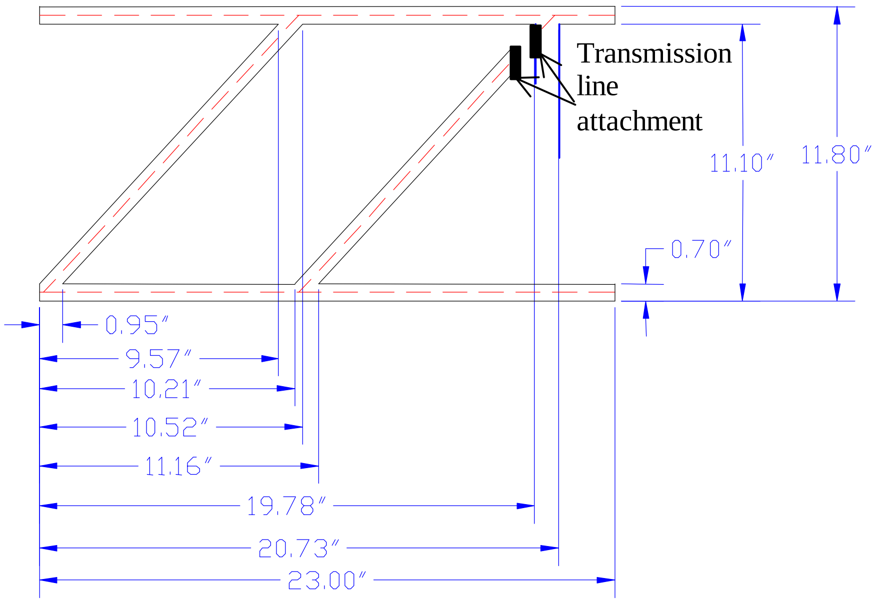

Figure 32. The 19-cm *m* = +1 antenna with 1.8 cm wide copper straps. The antenna was wrapped around HELIX and the left and right ends of the antenna joined together.

The first three antennas built and tested were the double saddle antenna, the 19 cm wide strap *m* = +1 (WSH19) antenna and the Nagoya III. For the double saddle and *m* = +1 antennas, a good match was not achievable below 8.1 MHz. With the original antenna, a match was possible down to 6.0 MHz. Since previous measurements had shown that plasma density is proportional to inverse driving frequency [*Keiter et al.*, 1997], it was believed that lower frequency operation would provide the highest possible densities. A key factor in matching antennas at different frequencies is the inductance of the antenna. The inductance of the original antenna was 0.73 μH while each of the new antennas had a smaller inductance. The 19 cm wide strap $m$ = +1 antenna inductance is 0.50 μH, the double saddle coil antenna inductance is 0.21 μH, and the inductance of the Nagoya III antenna is 0.20 μH. In an attempt to operate the source at lower frequencies, the 30 cm narrow strap (NSH30) $m$ = +1 antenna with an inductance of 1.02 μH was constructed. At the same driving frequencies and other source parameters, the 30 cm $m$ = +1 antenna actually yielded lower densities than the 19 cm wide strap $m$ = +1 antenna. Finally, the 19 cm narrow strap $m$ = +1 (NSH19) antenna with an inductance of 0.20 μH was constructed and has proven to generate the highest overall densities of any antenna. Although the wider straps along the discharge tube should lower the antenna inductance for the 19 cm wide strap $m$ = +1 antenna compared to the 19 cm narrow strap $m$ = +1 antenna, the inductance increase due to the wider straps around the discharge tube apparently dominates the antenna inductance and results in an overall increase in the inductance for the wider strap antenna. Given that the inductances of the narrow strap narrow strap 19 cm $m$ = +1, the Nagoya III, and the saddle coil antennas are nearly identical, the power coupled into the antennas for a fixed amount of forward RF power should be nearly identical. Therefore, differences in the densities and ion temperatures generated by these three antennas reflect the differences in the efficiency by which these antennas couple energy into the plasma.

Note also that the transmission line attaches at one end of the antenna. This configuration was chosen to eliminate the electric field discontinuity in the middle of the antenna that arises from the difference in phase between the two current feeds. When the feeds are in the middle of the antenna, the "cross-tube" electric field (between the straps running along the axis of the discharge) undergoes an abrupt change in middle of the antenna. In other words, the capacitive coupling properties of the antenna are different when the antenna is feed from one end instead of the middle.

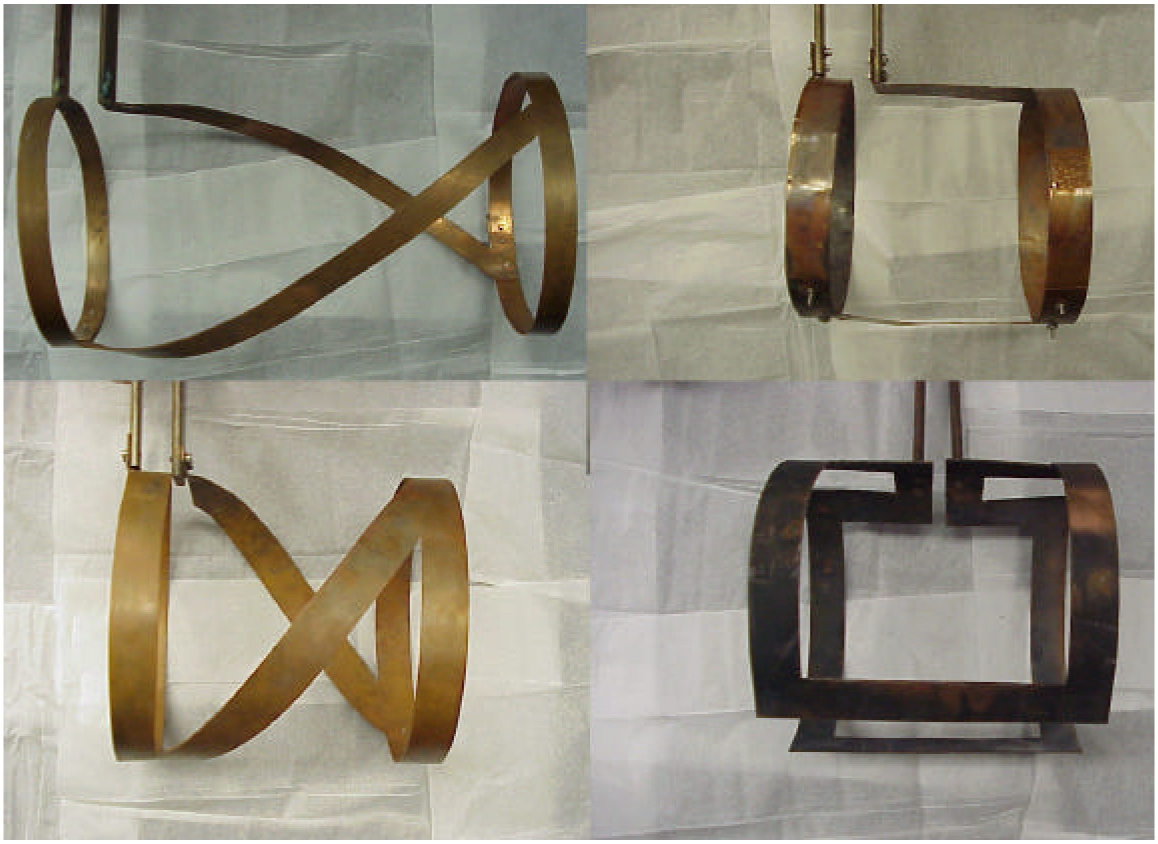

Figure 33. Starting at the top left and proceeding clockwise are the 30 cm *m* = +1 antenna, 19 cm Nagoya III antenna, 19 cm double-saddle antenna, and the 19 cm *m* = +1 antenna with 2.54 cm wide straps. The 19 cm *m* = +1 antenna with 1.8 cm straps is not shown.

The 30 cm long *m* = +1 antenna shown in Figure 32 was wrapped around HELIX in a cylindrical shape so that the right and left ends in Figure 32 were joined together. The ends were silver platted, overlapped by at least 3 cm, and screwed together using stainless steel #4 screws. Photographs of the double-saddle, Nagoya III, 19 cm *m* = +1 with 2.54 cm straps and 30 cm *m* = +1 antennas are shown in Figure 33. The 19-cm antenna with narrow straps (1.78 cm wide) is not shown. That the transmission line is connected at one end of the antenna can be seen for all but the double saddle coil antenna in Figure 33. The reengineered matching circuit and new antenna design eliminated all of the overheating problems that plagued the previous design. The Nagoya III antenna was the only antenna that became hot during moderate power (100 – 750 Watts) operation. Owing to a lack of 0.16 cm thick copper at the time of construction, the Nagoya III antenna was made from 0.051 cm thick copper. The extra resistive losses due to the thinner copper are the most likely cause of the extra heating of the Nagoya III antenna. Unlike the original antenna, heating of the Nagoya III antenna did not lead to short circuits because no plastic components were used in construction of the new antennas.

An unexpected side effect of the new, low resistance transmission line connecting the new matching circuit to the antennas was noticed during initial operation of the double-saddle antenna. At driving frequencies of 15 MHz, RF pickup by the HELIX magnet power supply resulted in the reporting of erroneous values of supply current by the power supply circuitry. There were even cases when the power supply current read negative. The RF pickup occurred over a narrow frequency range. Additional grounded RF shields around the transmission line (Figure 31) eliminated the RF pickup at 15 MHz and increased the density in LEIA by a factor of 1.26 for a driving frequency of 9.0 MHz, magnetic fields of 595 G in HELIX and 35 G in LEIA, and 400 W of forward power. The increase in density indicates that the addition of the RF shields prevented coupling of RF power to the magnet circuit and increased the power coupled to the plasma. The grounded shield was used for all of the data reported in this dissertation.

Qualitatively, the plasmas created in HELIX by the double-saddle, Nagoya III, and the original antenna tended to have dull, diffuse blue cores (the inner region of the discharge). The cores produced by the WSH19 antenna were brighter than the double-saddle antenna, but were not very bright. The NSH30 and the NSH19 antennas produced plasmas with intense, well-defined, blue cores (Figure 34). Because the overheating problems had been eliminated, all five antennas could be operated at higher RF power than the original antenna.

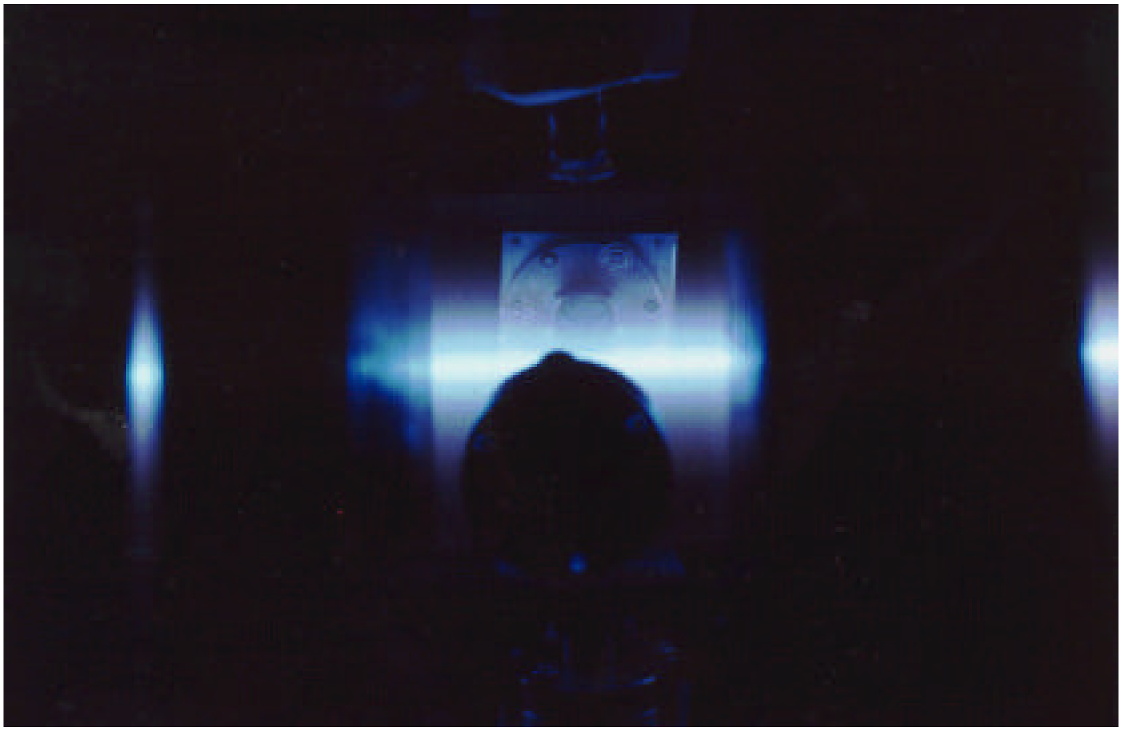

Figure 34. HELIX plasma with a well-defined, intense, blue core.

Preliminary density and temperature measurements for these new antennas are presented in the following section. In all cases, significant improvements in the power needed to achieve, "blue-core," helicon mode operation were observed.

### 3.3 PRELIMINARY RESULTS AND DISCUSSION

The five new antennas were installed and operating regimes for each antenna established. The range of frequencies for which a good match was achievable, less than 10% reflected power, was slightly different for each antenna. For most cases, the various antennas generated different densities and ion temperatures for identical input parameters. Since a key goal of this work was to design a source in which the plasma density could be maximized with minimal ion temperature, both density and ion temperature measurements were made over wide range of neutral pressures, RF powers, HELIX magnetic field strengths, and for those driving frequencies at which a good match was possible for all five antennas.

All of the new antennas with the reengineered matching circuit show increased density production over the original antenna and circuit design. Figure 35 compares radial density profiles for the modified matching circuit and antennas to a profile measurement for the original $m = +1$ antenna and matching circuit. The magnetic fields in HELIX and LEIA were 596 G and 35 G respectfully, the forward power was 400 W, and the fill pressure was 3.6 mTorr for all data in Figure 35. The driving frequency was 8.1 MHz for the NSH19 antenna and the double-saddle antennas but was 8.0 MHz for the other three new antennas and the original antenna. A good match was not achievable below 8.1 MHz for the WSH19 and the double-saddle antennas.

All of the new antennas produce a greater downstream, in LEIA, density than the original antenna (Figure 35). The density produced by the WSH19 antenna is a factor of five denser than the plasma produced by the original matching circuit and antenna. These data demonstrate that the reengineered matching circuit and antennas couple power into the plasma with greater efficiency than the original antenna and matching circuit.

The Langmuir probe was rebuilt for the NSH19 and for the NSH30 antenna measurements to remove a resistive layer on the probe tip. To avoid this problem in later measurements, the cleaning process described in chapter 2, section 2.1 was developed. Because of the probe reconstruction, there is an uncertainty (less than 50%) in the cross calibration between Langmuir probe measurements for the Nagoya III, double-saddle, and WSH19 antennas and the two narrow strap antennas. Therefore, this preliminary data cannot be used for quantitative comparison of the narrow strap antennas with the original antenna. However, the density measurements presented in chapter 4 used a single Langmuir probe, show that the NSH19 antenna produces plasmas of comparable density to the WSH19 antenna generated plasmas.

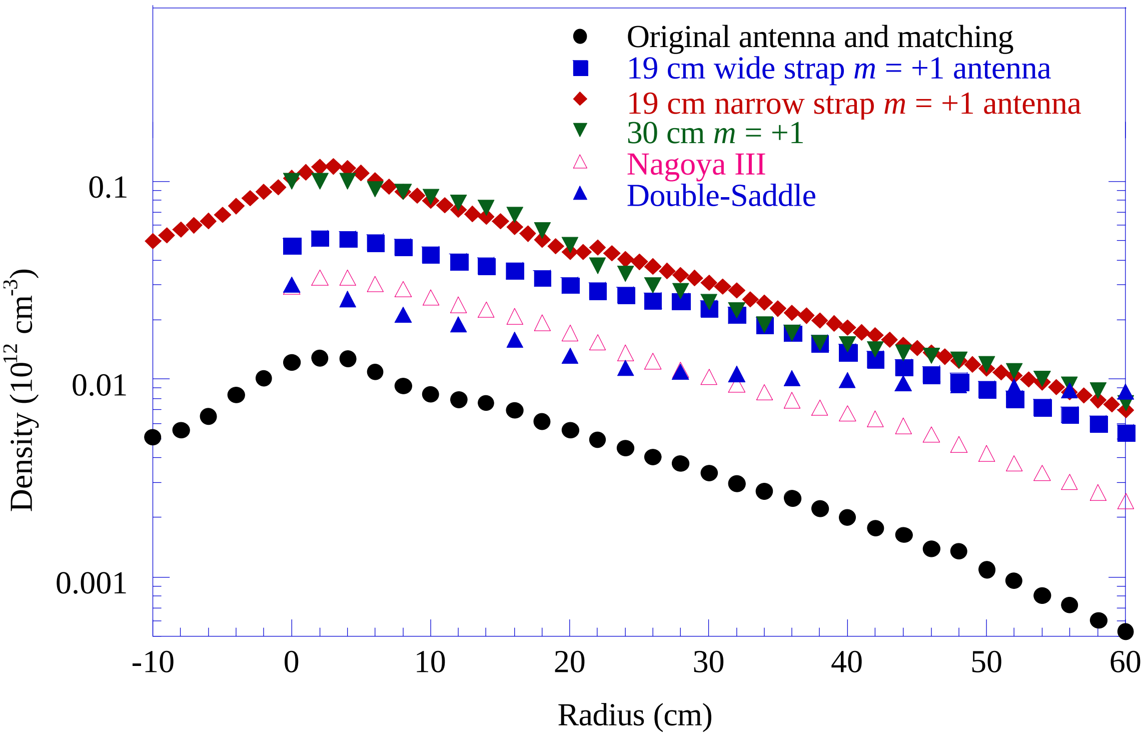

Figure 35. Electron density versus LEIA radius for the five new antennas and the original antenna and matching circuit. The RF power was 400W, the HELIX magnetic field was 596G, the LEIA magnetic field was 35G, and the neutral fill pressure was 3.6 mTorr. The driving frequency was 8.1 MHz for the 19 cm wide strap $m = +1$ and the double-saddle antennas and was 8.0 MHz for the other antennas.

For all five antennas, the density peak occurs at a radius of approximately 2 cm and the density profiles are similar. The 2 cm offset could be due to a number of factors: a real off axis peak in the plasma density, an error in zeroing of the Langmuir probe, a slight misalignment of the HELIX and LEIA magnetic fields, and a structural misalignment of HELIX and LEIA. After these preliminary experiments, an end-to-end realignment of the HELIX and LEIA vacuum chambers, and HELIX and LEIA magnetic fields, and the Langmuir probe was performed to eliminate any systematic errors in later profile measurements. Because the density profiles were so similar, measurements at a single radial position, $r = 0$, were used for the preliminary neutral pressure, RF power, magnetic field, and driving frequency parameter scans. Note that the inductances of the NSH19, Nagoya III, and double saddle are nearly identical. Since the forward power is the same for these three antennas, the power delivered to the antenna is the same.

The perpendicular ion temperature and downstream plasma density as a function of neutral pressure in the source are shown in Figure 36 for the five new antennas. For these measurements, the source magnetic field was held constant at 800 G, the RF frequency was 9.0 MHz, and the RF power was 500 W. Figure 36b and Figure 36c indicate that the Nagoya III and narrow strap antennas generate similar plasma densities, while the plasma densities obtained with the double saddle are approximately 30% smaller. More striking is the difference in ion temperatures between these three antennas. The maximum ion temperature achieved with the saddle coil and Nagoya III antennas is 0.25 eV, while the peak ion temperature for the NSH19 cm antenna is 0.6 eV. The ion temperatures for the NSH19 antenna are larger by a factor of two for all pressure values in the scan.

The trends in the electron density versus pressure shown in Figure 36d and Figure 36e for the WSH19 and NSH30 antennas are consistent with the results for the NSH19 antenna. The larger error bars for these data sets are due to uncertainties in the cross-calibration between the Langmuir probes used for the NSH30 and WSH19 antennas and for the double saddle, Nagoya III, and NSH19 antenna measurements. The drop in density and increase in perpendicular ion temperature at low pressure for all five antennas was observed in previous measurements [*Scime et al.,* 1998]. The leveling off in density above a threshold pressure is also consistent with previous measurements in HELIX [*Scime et al.*, 1998] and other helicon sources [*Kim and Chang*, 1996].

Noticeably different are the ion temperatures for the WSH19 antenna. Both narrow-strap antennas (the 19 cm and 30 cm), yield similar ion temperatures. However,

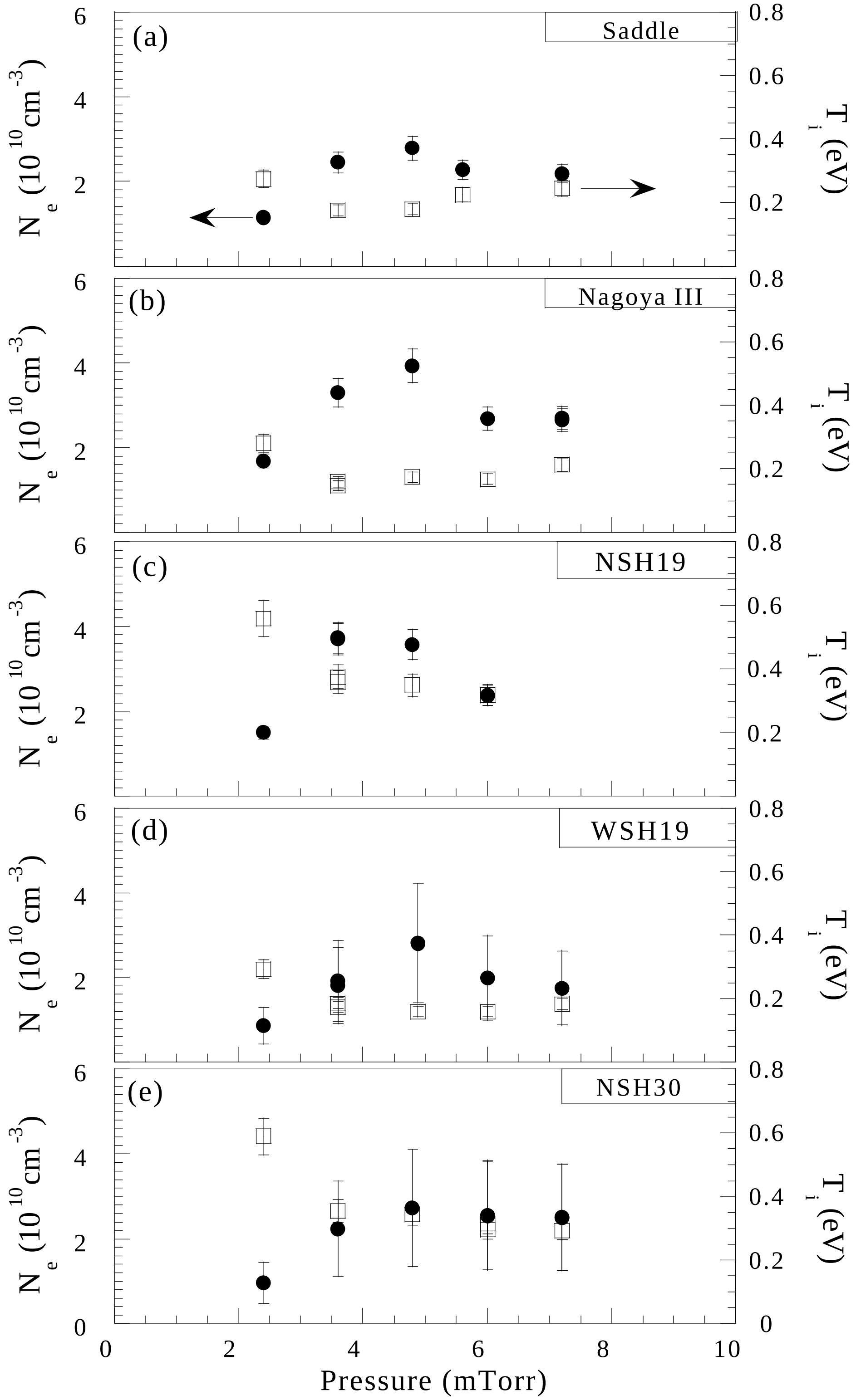

Figure 36. Downstream plasma density (solid circles) and perpendicular ion temperature in the source (open squares) versus neutral pressure. A) 19 cm double saddle antenna. B) 19 cm Nagoya III antenna. C) 19 cm *m* = +1 antenna with narrow straps (NSH19). D) 19 cm *m* = +1 antenna with wide straps (WSH19). E) 30 cm *m* = +1 antenna (NSH30).

the WSH19 ion temperatures are significantly lower at all pressures. It is important to note that at the lowest pressure value, the visual structure of the plasma changed considerably and it is unlikely that the source remained in the helicon mode.

For the same magnetic field of 800 G, RF frequency of 9 MHz, and a pressure of 3.6 mTorr, the downstream plasma density and perpendicular ion temperature versus RF power are shown in Figure 37. For all five antennas, both the density and perpendicular ion temperature increase with increasing RF power. Again, of the three antennas with the same inductance, the NSH19 antenna yields the highest densities and ion temperatures. Of the three different $m = +1$ antennas, the two antennas with narrow straps yield similar densities and ion temperatures.

For the same RF frequency of 9 MHz, pressure of 3.6 mTorr, and an RF power of 500 Watts, the perpendicular ion temperature and downstream plasma density versus the magnetic field strength in the source are shown in Figure 38. Of the three antennas with the same inductance, the NSH19 antenna still yields the highest densities and ion temperatures. Although the densities for the Nagoya III antenna are 20 - 30% lower than for the NSH19 antenna, the ion temperatures are 70% lower. The magnetic field scaling and RF power scaling results indicate that the plasmas densities achieved with the NSH19 antenna at 500 Watts can be attained with the Nagoya III antenna operating at 750 Watts, but with perpendicular ion temperatures a factor of two lower. Therefore, if low ion temperatures are desired, supplying more power to antennas that couple less efficiently to the plasma may provide the best solution.

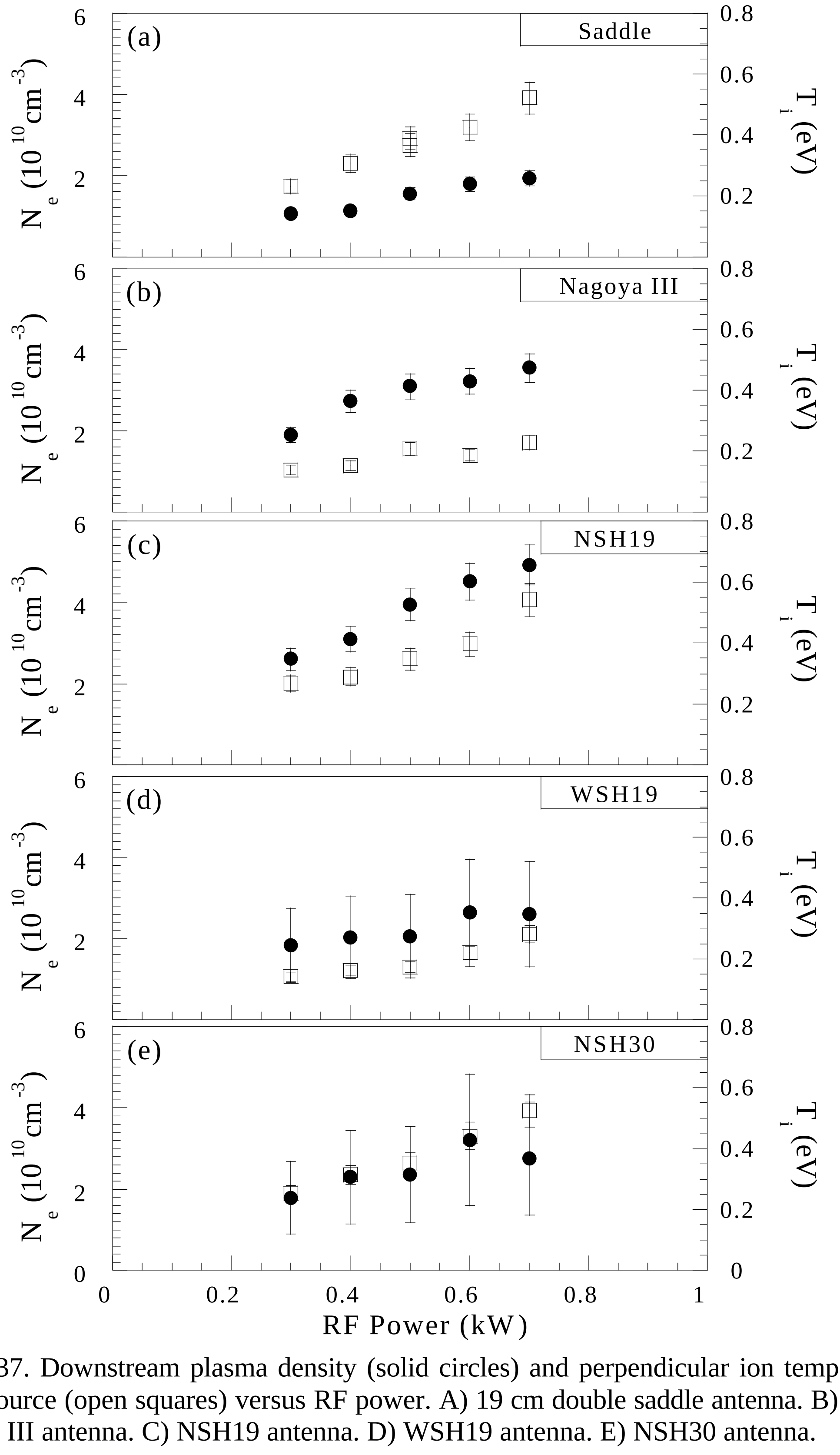

Figure 37. Downstream plasma density (solid circles) and perpendicular ion temperature in the source (open squares) versus RF power. A) 19 cm double saddle antenna. B) 19 cm Nagoya III antenna. C) NSH19 antenna. D) WSH19 antenna. E) NSH30 antenna.

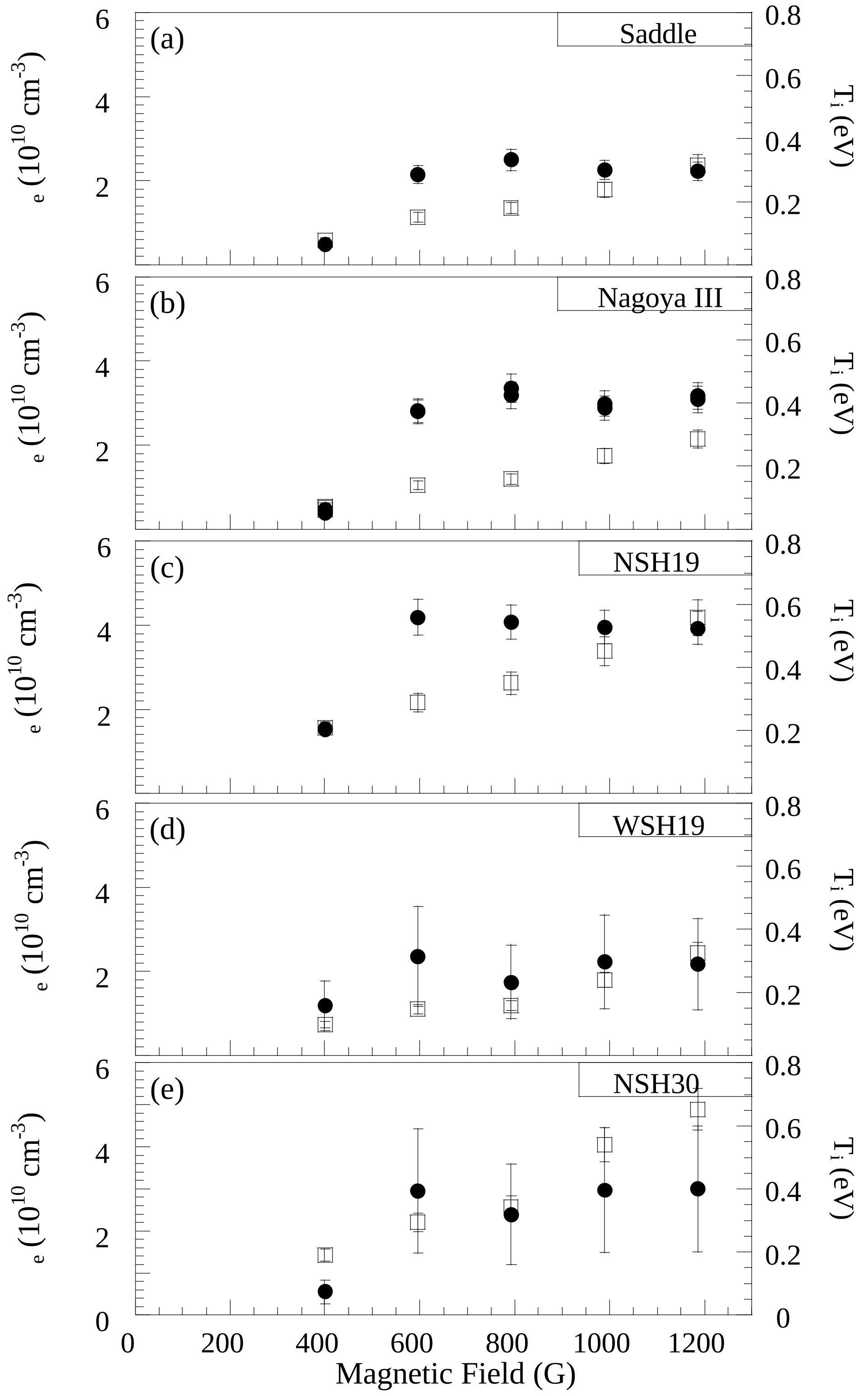

Figure 38. Downstream plasma density (solid circles) and perpendicular ion temperature in the source (open squares) versus HELIX magnetic field. A) 19 cm double saddle antenna. B) 19 cm Nagoya III antenna. B) 19 cm Nagoya III antenna. C) NSH19 antenna. D) WSH19 antenna. E) NSH30 antenna.

In contrast to reports from other groups of peaks in plasma density at particular RF frequencies [*Yun et al.*, 1997; *Kwak et al.*, 1997; *Cho*, 2000], previous measurements in HELIX showed clear evidence of monotonically increasing plasma density with decreasing RF frequency [*Keiter et al.*, 1997]. To re-examine the RF frequency dependence of the plasma density in HELIX, RF frequency scans such as the one shown in Figure 39 were performed. For these experiments, the magnetic field was 800 G, the RF power was 500 W, and the pressure was 3.6 mTorr. The data shown in Figure 39 do not indicate a strong dependence of density or ion temperature on driving frequency and appear to contradict the previous density measurements reported by *Keiter et al.* [1997]. However, the data presented in Figure 39 are over a narrow range of frequencies (7.5 to 10 MHz), at a single pressure, and a single magnetic field strength. Figure 40 shows data from a frequency scan at a higher pressure of 6.6 mTorr, a magnetic field of 600 G, and an RF power of 750 W. For these parameters, the linear dependence of plasma density on inverse driving frequency is clear. According to the helicon wave dispersion relationship, equation (2), the plasma density required for helicon wave propagation in a uniform plasma should be inversely proportional to RF frequency. Equation (2) can be rewritten in units typical of the experimental parameters

$$f[Mhz] = \frac{3.128B[G]}{l_{\parallel} l\,[\mathrm{cm}] n_e [10^{13}\mathrm{cm}^{-3}]}, \tag{21}$$

where $l^2 = l_{\parallel}^2 + l_{\perp}^2$ and $l_{\parallel}$ and $l_{\wedge}$ are the parallel and perpendicular wavelengths of the helicon wave, respectively, $B$ is the source magnetic field strength, $f$ is the RF frequency, and $n_e$ is the plasma density. Below 4 - 5 mTorr, the linear dependence of density on inverse RF frequency is not observed at a magnetic field strength of 600 G.

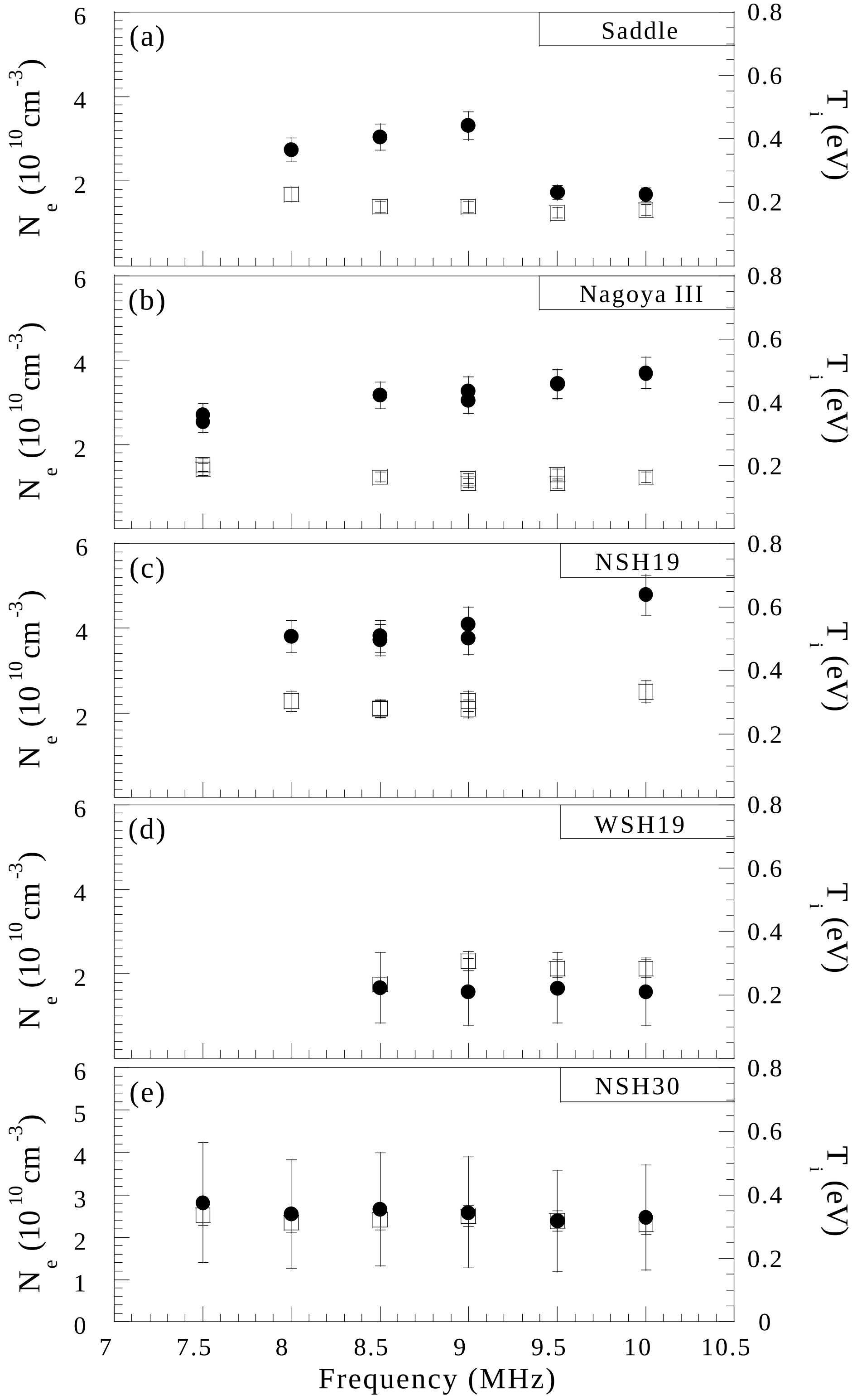

Figure 39. Downstream plasma density (solid circles) and perpendicular ion temperature in the source (open squares) versus RF frequency. A) 19 cm double saddle antenna. B) 19 cm Nagoya III antenna. B) 19 cm Nagoya III antenna. C) NSH19 antenna. D) WSH19 antenna. E) NSH30 antenna.

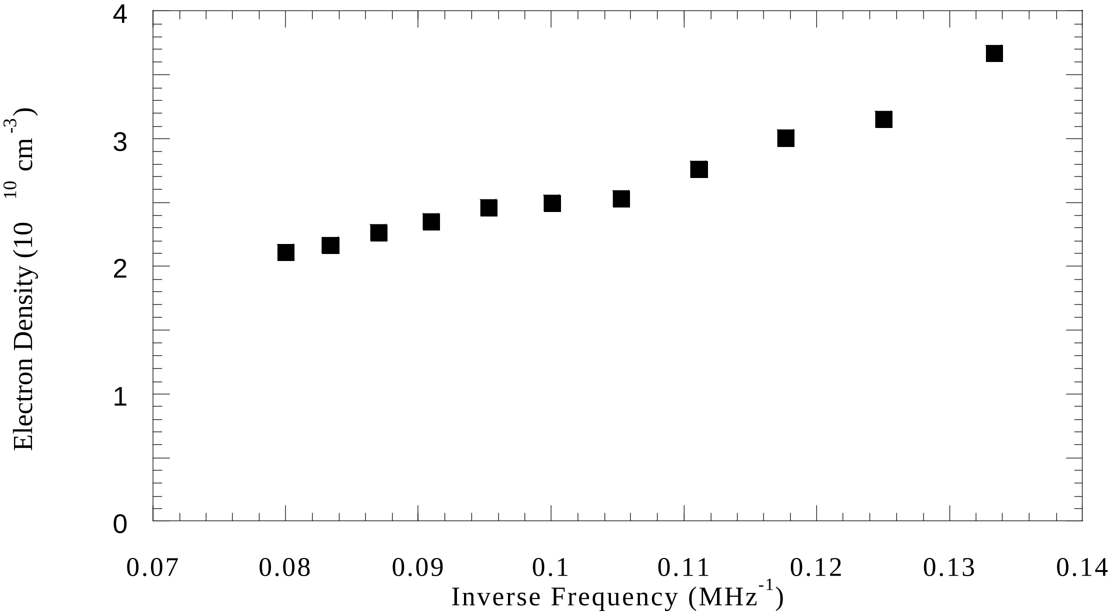

Figure 40. Downstream plasma density versus inverse RF frequency for the NSH30 antenna, a neutral pressure of 6.6 mTorr, a magnetic field of 600 G, and a forward power of 750 W.

# 4.0 EXPERIMENTAL RESULTS

A key objective of the experiments presented in this dissertation is to identify an experimental configuration that maximizes plasma density while minimizing ion temperature in a helicon source. The preliminary results discussed in chapter 3 were promising because they indicated that for particular choices of antenna and experimental parameters, the density of the plasma can be increased without a significant change in ion temperature. For example, the pressure scan data of Figure 36 show an increase in plasma density for the Nagoya III antenna at 4.0 mTorr without an associated increase in ion temperature.

The preliminary data also indicated the ion temperature scales strongly with magnetic field, while the plasma density reaches a plateau above which there is little increase with increasing magnetic field (see Figure 38). This suggests the mechanism responsible for ion heating is distinct from the process of plasma production. In fact, it is only during the RF power scans when the overall energy coupled into the plasma increases that both the plasma density and ion temperature increase simultaneously (see Figure 37). Given the preliminary frequency dependent density measurements shown in Figure 40 and the strong dependence of ion temperature on magnetic field, additional experiments were conducted to carefully examine both the effects of magnetic field and RF frequency on the plasma density, electron temperature, and ion temperature in the combined HELIX source plus expansion chamber system. All measurements were performed at an RF power of 750 Watts and a neutral pressure of 3.6 mTorr. The higher RF power was chosen in order to maintain the discharge in the helicon mode over as wide a parameter range as possible.

The ion temperature, electron temperature, and plasma density measurements presented in this chapter were collected over a wide range of magnetic fields and RF frequencies. The driving frequency was varied from 8.5 MHz to 15.0 MHz in fourteen 0.5 MHz steps and the magnetic field was varied from 400 G to 1200 G in eleven 80 G steps. At each setting, the perpendicular and parallel ion temperatures were measured with LIF. Depending on the signal to noise level, each ion temperature measurement reported represents an average of between ten to twenty individual measurements. In all cases, the ion temperature was anisotropic and the parallel ion temperatures showed the same trends as the perpendicular ion temperatures. Therefore, only the perpendicular ion temperature measurements are discussed in detail. Every density measurement reported is also an average of ten to twenty individual Langmuir probe scans. The number of Langmuir probe sweeps used in each average density value was the same as the number of LIF measurements performed at the same source parameters. The ion temperature, electron temperature, plasma density, and magnetic fluctuation measurements were then repeated for four different antennas: the wide strap 19 cm $m$ = +1 (WSH19), the narrow strap 19 cm $m$ = +1 (NSH19), the 30 cm $m$ = +1 (NSH30), and the Nagoya III. To ensure self-consistency, the same Langmuir probe was used for all the measurements and was cleaned between runs as described in chapter 2. To confirm that the downstream density measurements accurately reflected trends in the source density, pulsed plasma measurements of the source density (see Figure 10) were made at many of the magnetic field and RF frequency values. In all cases, the downstream Langmuir probe and microwave interferometer measurements were consistent.

The result of these detailed experiments was a collection of over four thousand ion temperature, electron temperature, and plasma density measurements for each antenna. Previous studies of driving frequency effects in helicon sources were restricted to course frequency scans at one or two magnetic field values [*Keiter et al.*, 1997; *Kwak et al.* 1997] or a coarse magnetic field scans at one or two RF frequencies [*Keiter et al.*, 1997; *Kwak et al.* 1997; *Yun et al.*, 1997]. Therefore, the experiments reported here are for the first high-resolution investigation of the combined effects of driving frequency and magnetic field strength in a helicon source.

In addition to the ion temperature, electron temperature, and plasma density measurements, measurements of the fluctuating magnetic field at the edge of the source were acquired from fifteen magnetic sense coils distributed azimuthally and axially. The magnetic fluctuation measurements enable determination of the parallel and perpendicular wavenumbers at the edge of the source using the techniques described in chapter 2. For all four antennas, measurements of the parallel and perpendicular wavenumbers based on $B_r$, $B_q$, and $B_z$ were acquired at each magnetic field value (400 G to 1200 G in 80 G steps) for driving frequencies of 8.5 MHz, 11.5 MHz, and 15.0 MHz. For the NSH19 antenna, $k_z$ measurements were performed at all magnetic field and driving frequency values. For the WSH19 antenna, measurements of $k_z$ were performed at all values of the driving frequency and for magnetic field strengths from 400 G to 1200 G in 160 G steps. Typically, fifty time series records of 8192 points were recorded for each magnetic fluctuation measurement. Acquisition and storage of the magnetic fluctuation data required approximately 10 minutes for each wavenumber measurement. The magnetic fluctuation data set fills thirty-two, 600 Mbyte compact disks.

### 4.1 DENSITY AND TEMPERATURE MEASUREMENTS

The ion temperature in the source, downstream plasma density, and downstream electron temperature versus source magnetic field and RF frequency are shown in Figure 41 for four antennas: the WSH19, the NSH19, the NSH30, and the Nagoya III. The electron temperature is determined from the slope of the Langmuir probe I-V characteristic in the electron retardation region. Looking at the first column of Figure 41, it is clear that the maximum ion temperature for all four antennas occurs in the region of smallest RF frequency and largest magnetic field strength. Here again, the Nagoya III antenna consistently yields the smallest ion temperatures (by a factor of two or more). Evident in the four ion temperature plots is a boundary between higher and lower ion

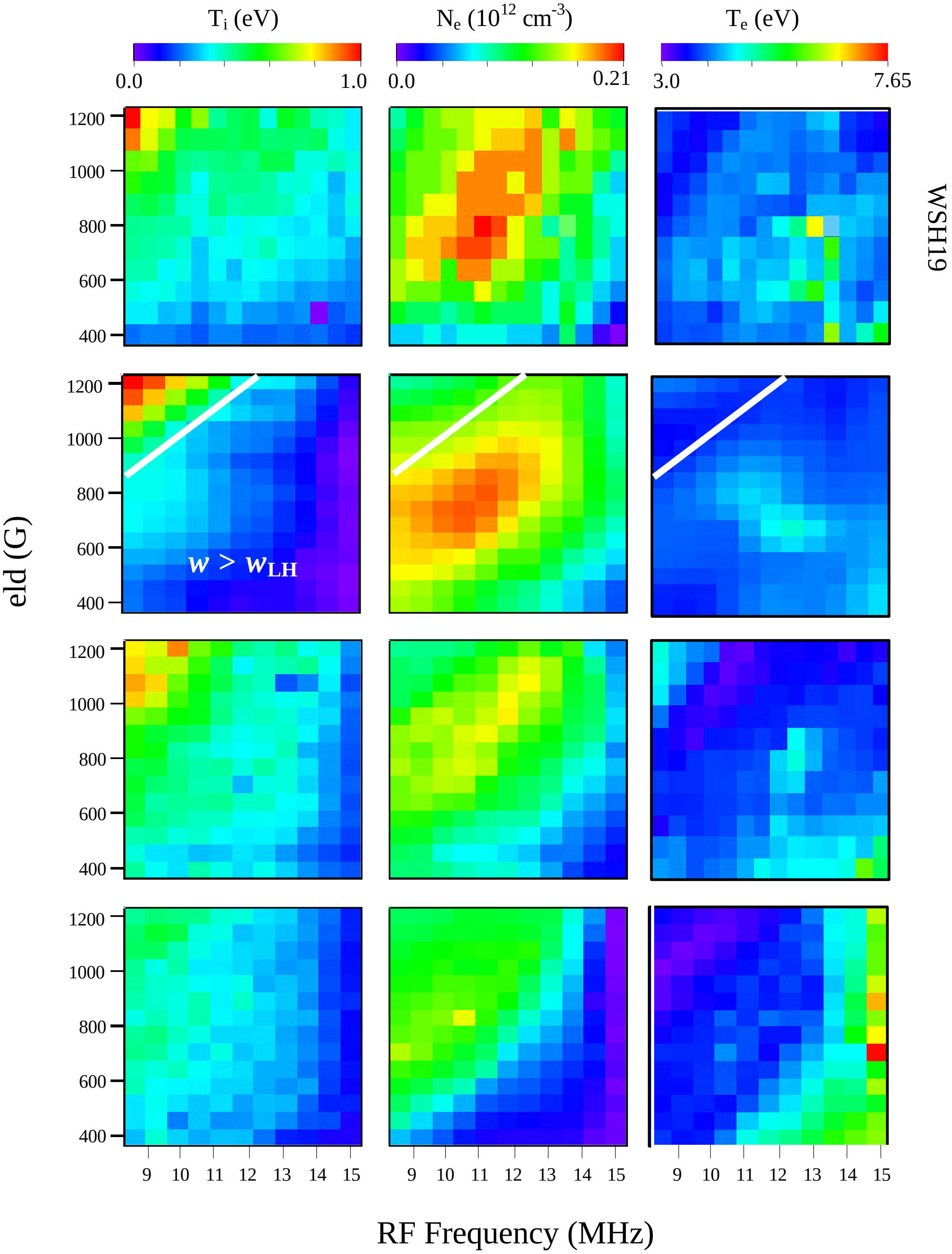

Figure 41. Perpendicular ion temperature, downstream electron density, and downstream electron temperature versus magnetic field strength and rf frequency for the WSH19 antenna, the NSH19 antenna, NSH30 antenna, and the Nagoya III antenna. All plots of each parameter are on the same color bar scale that is shown at the top of each column. The gas pressure was 3.6 mTorr and the RF power was 750 Watts for all of the measurements.

temperatures that follows a line of increasing frequency for increasing magnetic field. This trend is clearest in the NSH19 antenna measurements (second plot in first column of Figure 41). Not only does the NSH19 antenna generate the highest ion temperatures, the rate of decrease in the ion temperature as the RF frequency rises or the magnetic field decreases is greater than for the other antennas, i.e., $dT_i/df$ and $dT_i/dB$ is largest.

The contours of constant ion temperature in the NSH19 antenna data run parallel to the curve along which the RF frequency equals the lower hybrid frequency, $w_{LH}$ , in the source (shown as a white line in all of the plots for the NSH19 antenna). $w_{LH} \cong \sqrt{w_{ce}w_{ci}}$ for these plasma parameters, where $w_{ce}$ and $w_{ci}$ are the electron and ion cyclotron frequencies respectively. Because the bulk of the ion heating occurs for RF frequencies close to or slightly below the lower hybrid frequency and the constant temperature contours parallel the lower hybrid frequency curve, lower hybrid waves or the decay of lower hybrid waves into other waves may be responsible for the ion heating in helicon sources. It should be noted that the contours of constant ion temperature also run parallel to the curve for ion cyclotron frequency, but the RF frequencies used here are hundreds of times greater than the ion cyclotron frequency (Table 1)

These ion temperature measurements are consistent with previous observations of increasing ion temperature with increasing magnetic field [*Scime et al.*, 1998]. However, missing in those experiments was any indication of a correlation between ion temperature and RF frequency. The correlation between ion temperature and RF frequency was overlooked because those RF frequency experiments were performed at a single magnetic field of 800 G. The ion temperature data shown in Figure 41 indicate that at 800 G, there is only a modest variation in ion temperature with RF frequency. It is only at the greater magnetic field strengths that the correlation between ion heating and RF frequency is evident.

The downstream density measurements (second column of Figure 41) for all four antennas indicate that the shorter $m$ = +1 antennas (NSH19 and WSH19) yield higher densities than the NSH30 antenna. Assuming that the measured parallel wavenumbers of the helicon wave in helicon sources are on the order of $p/L_A$, where $L_A$ is the antenna length of a half-wavelength antenna [*Light et al.*, 1995; *Light and Chen*, 1994], this result is consistent with the dispersion relationship commonly cited in the literature for small aspect ratio helicon sources ($L >> a$, where $L$ is the length of the system and $a$ is the plasma radius) [*Keiter et al.*, 1997]

$$n(r) = \frac{B_o k_{||}}{w m_o e a(r)} \tag{22}$$

where $a(r)^2 = k_{||}^2 + k_{\perp}^2$, $k_{||}$ and $k_{\perp}$ are the parallel and perpendicular wavenumbers respectively, $k_{\perp} >> k_{||}$ because of the aspect ratio of the source and the length of the antenna, $B_o$ is the source magnetic field, $w$ is the driving frequency, $m_o$ is the free space permeability, $e$ is the electron charge, and $n$ is the electron density. According to equation (22), antennas that launch shorter wavelength waves along the field (larger $k_{||}$) should match at higher plasma densities. The only difference between equation (22) and equation (21) is that equation (22) has been written in the form commonly used in the helicon source literature.

Note also that the Nagoya III yields the smallest densities, by a factor of two, of any of the four antennas. In fact, at low magnetic fields or high RF frequencies, the Nagoya III plasmas drop out of the helicon mode entirely. The dramatic drop in density for these parameters corresponds to a sharp rise in the electron temperature (see the third column of Figure 41 for the Nagoya III electron temperature measurements). The edge of the region for which the Nagoya III plasmas are in the helicon mode also parallels the lower hybrid frequency curve.

Most striking in the electron density measurements is the clear peak in density for RF frequencies just above the lower hybrid frequency. Looking again at the data for the NSH19 antenna, the correlation between lower hybrid frequency and peak density production is unmistakable. The correlation does not extend to the highest frequencies studied. This suggests that other experiments operating at frequencies above 13 – 14 MHz, will not see enhanced density production unless they operate at much higher magnetic fields than is typical. This is consistent with previous observations of a higher power threshold for the helicon mode at higher RF frequencies *Keiter et al.* [1997]. If only the data at higher frequencies than the density peak are used, the plasma density data in Figure 41 are also consistent with the *Keiter et al*. [1997] measurements of a linear dependence of density on inverse driving frequency. The *Keiter et al.* [1997] experiments were for a Nagoya III antenna operating at a magnetic field of 600 G. The density data for the same conditions has been extracted from Figure 41 and is shown in Figure 42 for comparison. At higher frequencies (smaller 1/*f*), the linear dependence of plasma density

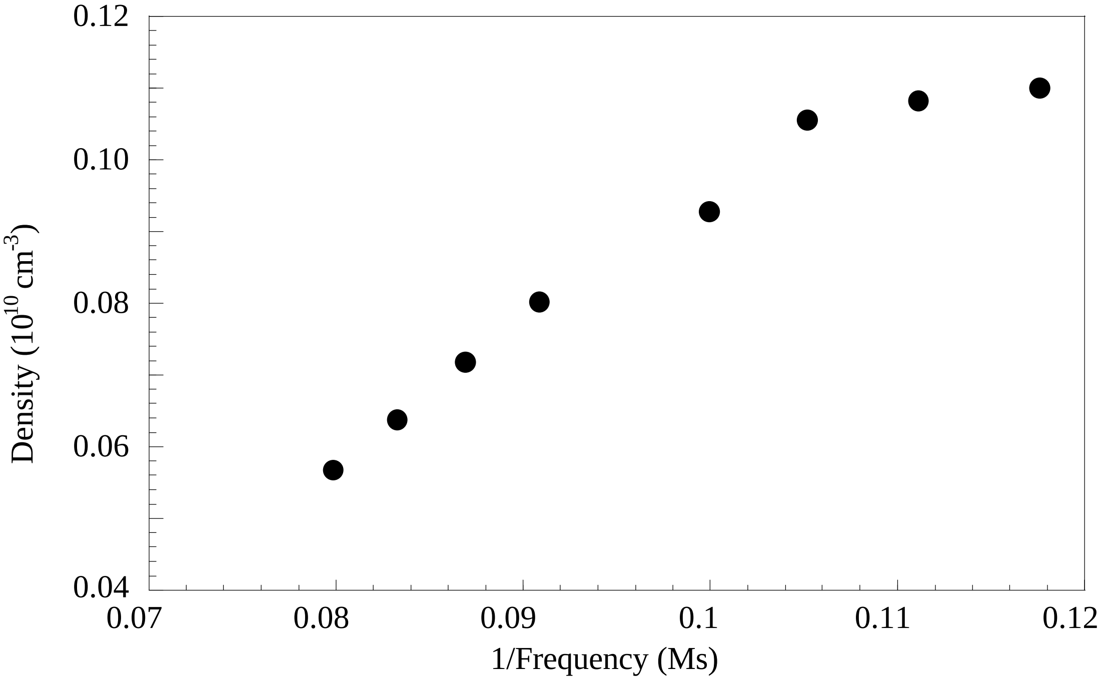

Figure 42. Electron density verses inverse frequency for the Nagoya III antenna at 600 G.

on inverse driving frequency, i.e., the helicon dispersion relationship, is unmistakable in Figure 42. At the lower frequencies, the density reaches a plateau. The constancy of the density at the lower frequencies suggests that the helicon dispersion relationship is not appropriate for helicon sources operating near the lower hybrid frequency.

Correlations between density production and the lower hybrid frequency have been observed since the beginning of helicon source research [*Boswell*, 1984; *Zhu and Boswell*, 1989; *Yun et al.*, 1997, *Cho*, 2000]. The role of lower hybrid resonances in helicon sources has received some emphasis in recent years as resonance absorption of RF power at the lower hybrid frequency has been suggested as a possible mechanism for the efficient operation of helicon sources [*Cho*, 2000; *Borg and Boswell*, 1998]. The helicon wave has no resonance for typical helicon source parameters and therefore collisional damping or more exotic collisionless wave damping mechanisms are often invoked to explain the RF power absorption in helicon plasmas. However, the bounded electron cyclotron wave that appears at frequencies above the lower hybrid frequency in the cold plasma dispersion relationship when finite electron mass is included (often referred to as the “slow” or “Trivelpiece-Gould” wave in the helicon source literature) is believed to exist as an edge mode in helicon sources [*Shamari and Taranov*, 1995] and does have a resonance at the lower hybrid frequency [*Cho*, 2000]. These observations support the conclusion that, although the helicon wave may play some role in density production in helicon sources, the lower hybrid resonance dominates the RF power absorption in helicon plasmas operating at low RF frequencies.

Except for the 30 cm $m = +1$ antenna, none of the electron temperature measurements show any significant increase in the region of highest ion temperatures. That neither the electron density nor the electron temperature is enhanced at the same parameters where the ion temperatures are greatest, provides further evidence that collisional equilibration with the hotter electrons is not responsible for the observed ion temperatures. For the most part, the maximum electron temperatures are observed at the highest RF frequencies and the smallest magnetic field. Because the common electron temperature color bar in Figure 41 is dominated by the Nagoya III antenna measurements, the electron temperature data for the WSH19 antenna is plotted again in Figure 43 with a color bar scaled to the WSH19 antenna data range. Two regions of higher electron temperatures can be seen in the data. The region of high electron temperatures at low magnetic field strength and high driving frequency corresponds to the parameters at which the discharge drops out of the helicon mode. However, the other region of high electron temperature occurs in the helicon mode. In fact, a region of enhanced electron temperature for the same magnetic fields and driving frequencies can be seen in the electron temperature data for all three *m* = +1 antennas (Figure 41). This localized enhancement of electron temperature suggests that, for the proper choice of operating parameters, a helicon source can be optimized to generate hot electrons. The ability to control the electron distribution function in a helicon source could lead to new methods of controlling plasma chemistry in helicon sources.

Figure 44 shows the same data as Figure 41, but with an x-axis corresponding to the ratio of the lower hybrid frequency to the RF frequency. The color bars of each plot in Figure 44 have also been adjusted to provide maximum contrast. As can be seen in Figure 44, the normalized RF frequency at which the peak electron density occurs increases with increasing magnetic field. The majority of the highest density values lie in the range $0.5w_{LH} < w < 1.25w_{LH}$. The constant ion temperature contours (looking at the NSH19 antenna data) form vertical bars. Until we can extend the operating range of the source to higher magnetic fields or lower RF frequencies, we cannot say if the ion temperature continues to increase as frequency ratio increases. The enhanced contrast of the individual plots for the *m* = +1 antennas also brings out a correlation between electron temperature and electron density that was not obvious in Figure 41. Here again,

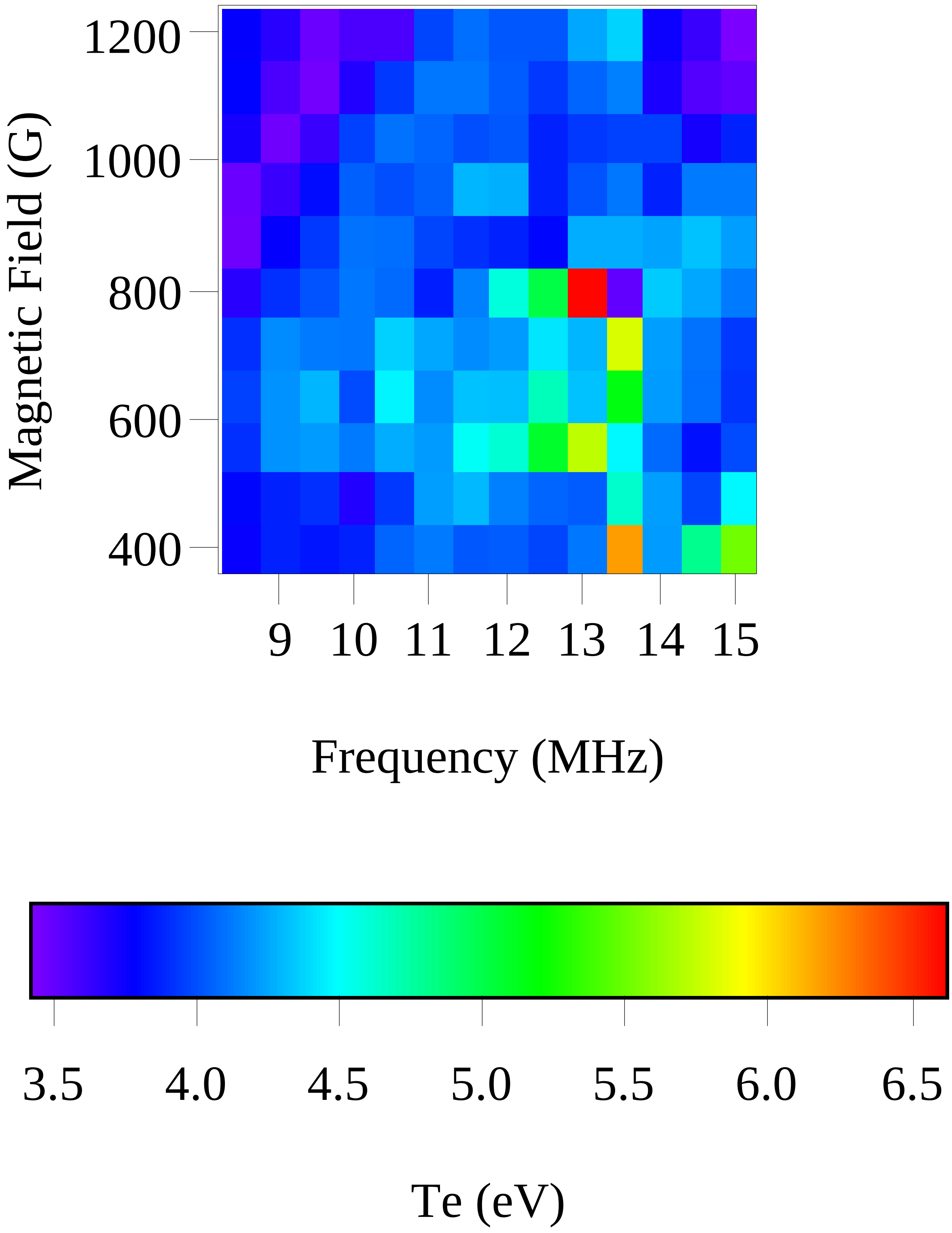

Figure 43. Electron temperature versus magnetic field and driving frequency for the WSH19 antenna. Two distinct regions of hotter electrons are evident.

however, there is no evidence of increased electron temperature at the parameters for which the ion temperatures are greatest. On close examination, the trend of increasing electron temperature for a constant relationship between magnetic field strength and RF frequency (the peaks running from the bottom left to upper right of the temperature plots of Figure 44) can be seen in Figure 41 as patterns of enhanced electron temperature running from the lower right to upper left in the electron temperature plots. This trend is particularly clear in the NSH19 antenna plots in Figure 44 and Figure 41.

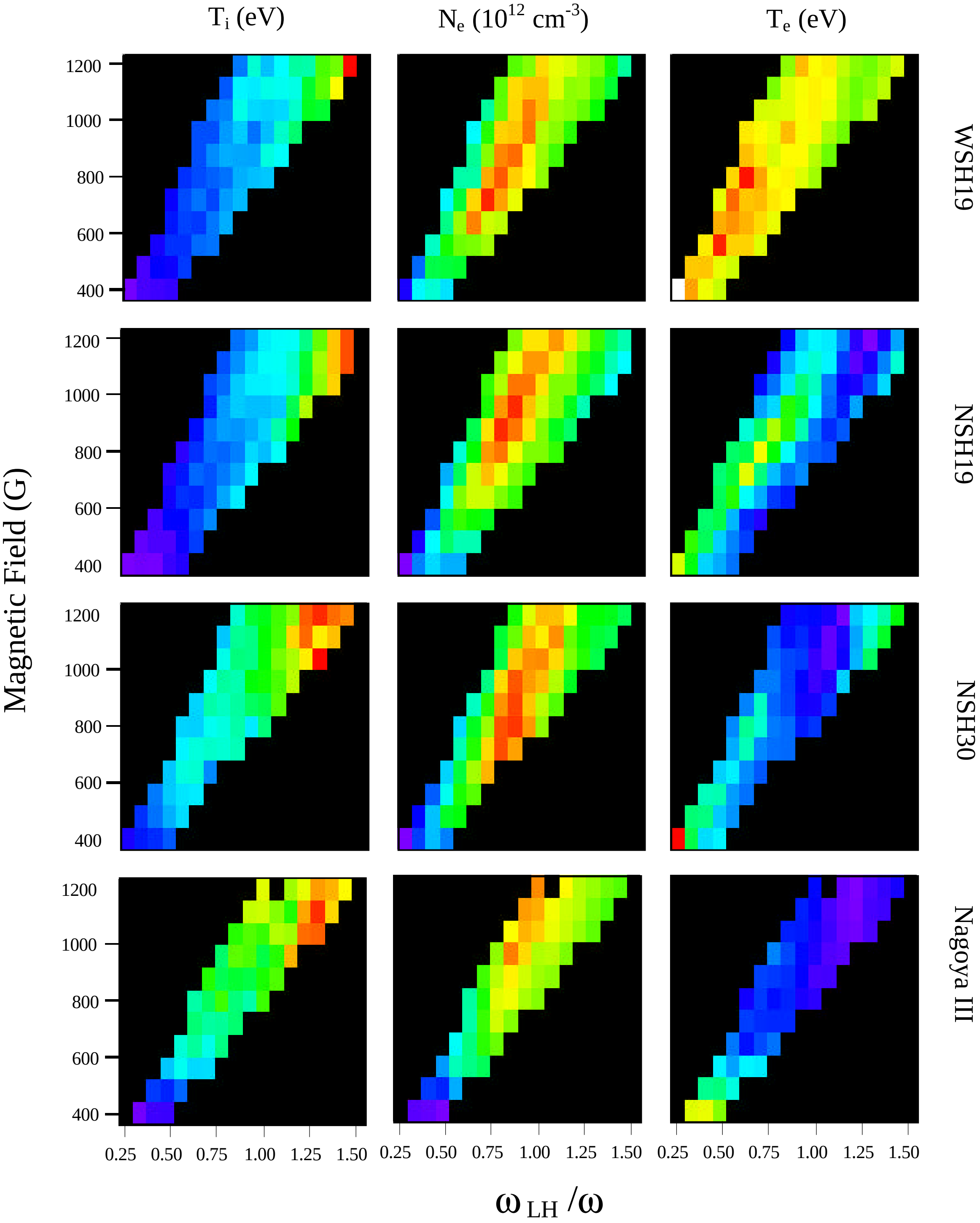

Figure 44. Perpendicular ion temperature, downstream electron density, and downstream electron temperature versus magnetic field strength and ratio of lower hybrid frequency to RF frequency for the WSH19 antenna, the NSH19 antenna, NSH30 antenna, and the Nagoya III antenna. The color bar for each plot has been individually adjusted to provide maximum contrast. The gas pressure was 3.6 mTorr and the RF power was 750 Watts for all of the measurements.

## 4.2 MAGNETIC FLUCTUATION MEASUREMENTS

Magnetic fluctuations at the edge of HELIX were recorded using the magnetic probe array discussed in chapter 2. For these measurements, the digitization rate was set at 1 gigasample/s to keep the Nyquist frequency of 500 MHz above the 300 MHz corner frequency of the transformer in the sense coil circuit (Figure 20). This prevents aliasing of high frequency signals. Frequency and wavenumber spectra were only calculated for magnetic fluctuations in the frequency range 0 - 50.0 MHz because the calibration of the sense coils was limited to frequencies below 50 MHz. The frequency resolution was 122 kHz because the TVS641 digitizer has a maximum $2^n$ record length of 8192 points. As discussed in chapter 2, the spacing between the sense coils determines the maximum wavenumber that can be resolved. The wavenumber resolution is determined by the number of bits available to resolve the amplitude of the fluctuations and the record length. Because the digitizer only had eight bits to cover the input voltage window, the input voltage window was optimized to the peak-to-peak voltage for every magnetic fluctuation measurement. Unless otherwise stated, all measurements of wavenumber and frequency spectra reported are the average of fifty successive wavenumber and frequency spectra recorded at identical parameters. By using an ensemble average of fifty measurements for each set of parameters, multiple wavenumbers can be resolved and the signal to noise is improved by a factor of $1/\sqrt{50}$ [*Assadi*, 1991].

An example of the two-dimensional local wavenumber and frequency spectrum of $\dot{B}_z$, equation (17) in chapter 2, at the edge of HELIX generated by the NSH19 antenna is shown in Figure 45. For this data, the parameters were a magnetic field of 1070 G, a neutral pressure of 3.6 mTorr, and a driving frequency of 9.0 MHz. The data in Figure 45 are from two $\dot{B}_z$ sense coils separated along the *z*-axis by 4.83 cm. Two distinct parallel wavenumbers for the 9.0 MHz driving wave and its harmonics are evident at these parameters. A logarithmic color scheme for the amplitude was used in Figure 45 because the range in intensity spans many orders of magnitude. Note that these source parameters are the same as those that result in enhanced ion heating (Figure 41).

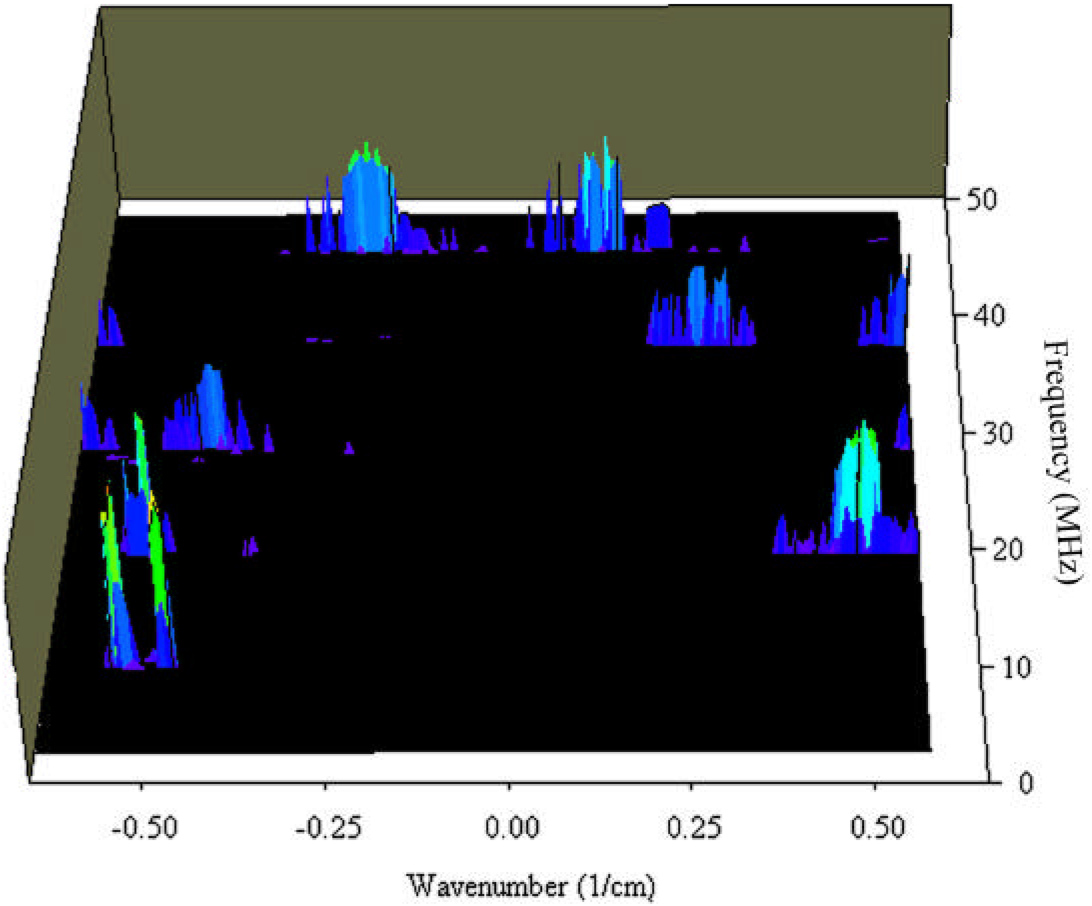

Figure 45. Two-dimensional local wavenumber and frequency spectrum for the NSH19 antenna for a magnetic field of 1070 G and a driving frequency of 9.0 MHz. The color bar for the intensity scale is logarithmic with red corresponding to the largest amplitudes.

The two-point correlation technique used for this analysis fails when large wavenumber, small wavelength, waves are present in the plasma. Waves with wavelengths shorter than twice the distance between the sense coils, 4.83 cm, are aliased. Thus, large wavenumber waves appear to correspond to waves with lower wavenumber magnitudes. An example of this effect can be seen in Figure 45 where waves at the driving, or fundamental, frequency appear around a wavenumber of -0.55 $cm^{-1}$ (left hand side of the figure). Given the orientation of the magnetic sense coils and the relative position of the sense coils and the antenna, a wave traveling away from the antenna parallel to the magnetic field should appear at a positive wavenumber in Figure 45 (right hand side of the figure). That aliasing is occurring can be seen in the wavenumber peaks for the second harmonic of the driving wave at 27.0 MHz. The positive wavenumber peak for the second harmonic is clearly wrapping around and appearing at negative wavenumbers because an overall phase shift of $\pi$ (maximum wavenumber) occurs. These high positive wavenumber waves then appear to have an artificially reduced wavenumber magnitude and a negative direction of propagation. The close spacing of the two wavenumber peaks for the 9.0 MHz driving wave and the dramatic change in sign for the wavenumber peaks of the first and second harmonics also suggest aliasing of short wavelength waves occurs during the measurement. Because the direction of wave propagation is known *a priori*, the extra $\pi$ phase shift between the sense coil signals can be ignored and the actual wavenumber determined even though the coils were spaced too far apart to correctly resolve the wavelength of the wave. Thus, waves at the fundamental frequency in Figure 45 have a positive wavenumber of 0.75 cm$^{-1}$, not a wavenumber of -0.55 cm$^{-1}$.

The parallel wavenumber at the RF driving frequency measured for each antenna as a function of magnetic field for a driving frequency of 8.5 MHz, an RF power of 750 W, and a pressure of 3.6 mTorr is displayed in Figure 46. The wavenumbers used in Figure 46 were determined directly from plots such as Figure 45. At low magnetic fields, the parallel wavenumbers for the NSH19 and WSH19 antennas are 0.25 cm$^{-1}$ and 0.35 cm$^{-1}$respectively. The $m = +1$ antenna design is often referred to as a half wavelength antenna [*Chen*, 1994] because the $p$ phase difference in the voltages between the ends of the antenna is expected to launch into the plasma a wave twice as long as the antenna. If the NSH19 antenna launched a 38 cm helicon wave as expected, the wavenumber at the fundamental frequency would be 0.16 cm$^{-1}$. Clearly, the antenna is not determining the wavelength of the wave in the plasma. Since the measured parallel wavelength is roughly half the wavelength expected for the antenna, the data suggest a shorter $m = +1$ antenna might result in improved power coupling to the plasma. Both the NSH30 and Nagoya III antennas launch waves with wavelengths significantly smaller than twice their length (Figure 46). Both of these antennas yield smaller plasma densities and lower ion temperatures than the shorter $m = +1$ antennas (Figure 41).

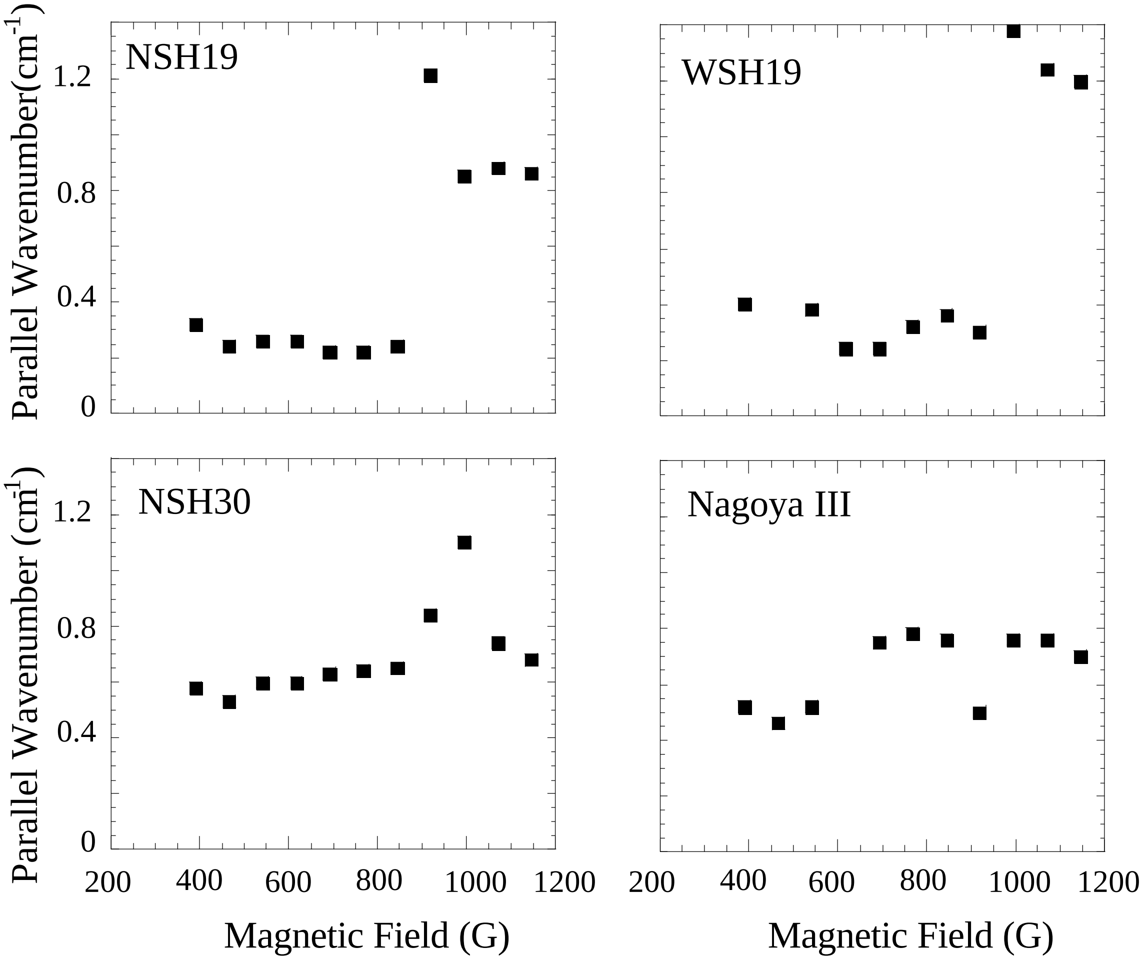

Figure 46. Wavenumber as a function of HELIX magnetic field for a driving frequency of 8.5 MHz and a fill pressure of 3.6 mTorr. Clockwise the top left are wavenumber measurements for the WSH19, the NSH19, the NSH30, and the Nagoya III antennas.

The axially spaced sense coils were separated by 9.5 cm for the NSH30 antenna wavenumber measurements. This spacing results in a maximum, non-aliased, wavenumber measurement of 0.33 $\text{cm}^{-1}$, but increased wavenumber resolution. The larger sense coil spacing was used because the NSH30 antenna was expected to launch waves with wavenumbers of 0.10 $cm^{-1}$ and the increased wavenumber resolution was thought to be required. Initial analysis yielded wavenumber measurements of -0.06 $cm^{-1}$ at 400 G. Because the propagation direction implied by a negative wavenumber is towards the antenna, the same arguments used for the NSH19 antenna are also applicable to the NSH30 antenna measurements. With correction for aliasing, the NSH30 antenna wavenumber measurements at 400 G become 0.6 $cm^{-1}$.

The wavenumber plots for all three $m = +1$ antennas show a clear transition from low wavenumber to a much higher wavenumber between magnetic fields of 920 G and 1000 G. At the transition, the wavenumber increases approximately a factor of four for the NSH19 and WSH19 antennas. Above 1000 G, the wavenumbers for NSH19 and WSH19 antennas drop to a nearly constant value that is significantly higher than the wavenumber measured at low magnetic fields. For example, at 1200 G the parallel wavenumber measured for the NSH19 is 0.85 $cm^{-1}$ compared to 0.25 $cm^{-1}$ at 600 G. As the magnetic field is increased above 920 G, the wavenumber measured for the NSH30 antenna increases sharply up to 1.1 $cm^{-1}$ and then drops back down to 0.6 $cm^{-1}$ as the magnetic field is raised above 1000 G. As the magnetic field increases, the wavenumber for Nagoya III antenna increases from 0.5 $cm^{-1}$ to 0.75 $cm^{-1}$ at 680 G, then is constant until 850 G, drops at 920 G, and increases back up to 0.75 $cm^{-1}$ for the remainder of the magnetic field scan.

The transition in parallel wavenumber that occurs between magnetic fields of 920 and 1000 G is unambiguous in the data for all three helical antennas. This magnetic field range corresponds to the same magnetic field range (for 8.5 MHz) at which strong ion heating becomes noticeable in the ion temperature data for all three helical antennas (Figure 41). For all four antennas, and over the range of magnetic field strengths investigated, the measured wavenumbers were greater than expected given the length of the half-wavelength antennas. The transition to higher wavenumbers at the same parameters as enhanced ion temperatures are observed suggests that even shorter antennas may more efficiently couple energy into the ions.

The azimuthally separated magnetic sense coils were also used to record the magnetic fluctuations at the edge of HELIX. For the NSH19 and Nagoya III antennas, the two-dimensional local wavenumber and frequency spectrum at the RF driving frequency versus wavenumber is presented in Figure 47 for two azimuthally separated coils oriented to detect $\dot{B}_r$. The wavenumber spectrum for the Nagoya III antenna peaks near -0.15 cm$^{-1}$ for all magnetic fields. The expected wavenumber for an $m$ = +1 azimuthally mode is -.13 cm$^{-1}$ given the 7.5 cm radius of HELIX and the orientation of the sense coils. The azimuthal wavenumber spectrum generated by the NSH19 antenna is broader than the spectrum generated by the Nagoya III antenna for all magnetic field strengths except 390 G. At 390 G, the plasma created with the Nagoya III antenna was visually consistent with an inductive, not helicon mode of operation [*Ellingboe et al.*, 1996]. For magnetic fields greater than 390 G, the mode spectrum at the fundamental frequency for the Nagoya III is dominantly an $m$ = +1 wave. Surprisingly, the helical NSH19 antenna, which should ideally only launch an $m$ = +1 wave, generates a broad azimuthal wavenumber spectrum. At magnetic fields of 690 G, 1070 G and 1146 G, two distinctly different wavenumbers appear in the wavenumber spectrum for the NSH19 antenna (Figure 47 and Figure 45).

The two-dimensional local wavenumber spectrum can also be summed over all wavenumbers to compare the power spectra generated by the different antennas. A series of power spectra for the NSH19 antenna, which yields the highest ion temperature and density, and the Nagoya III, which yields the lowest peak ion temperature and density, are compared in Figure 48. In Figure 48, the power spectra have been divided by $w^2$ to convert the $\dot{\vec{B}}$ power spectra into power spectra of the magnetic field fluctuations, $\vec{B}$. Both antennas were driven at 8.5 MHz, at a power of 750 Watts, a neutral pressure of 3.6

mTorr, and have nearly identical inductances. Thus, the same forward power was

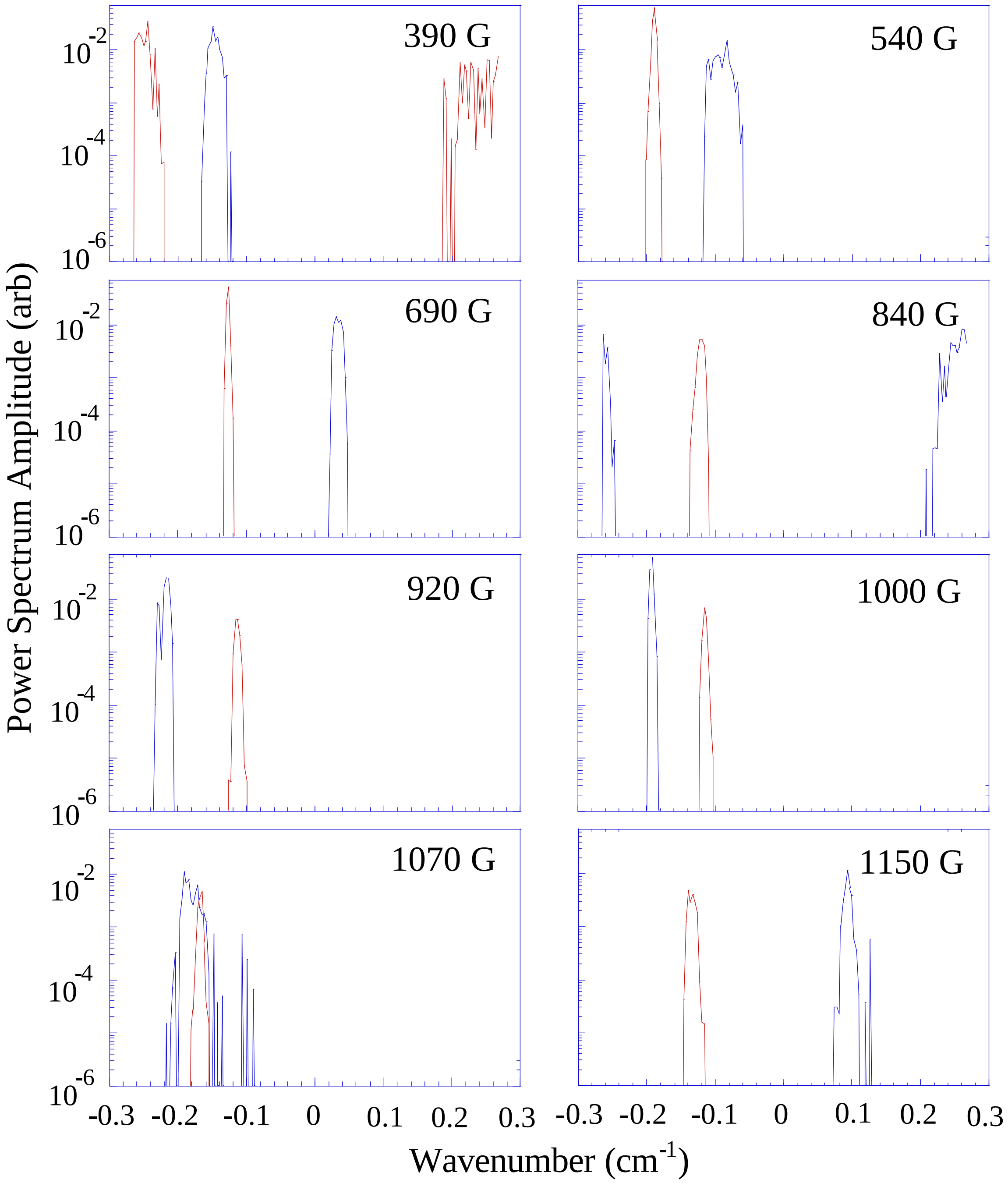

Figure 47. Amplitude of the two-dimensional local wavenumber and frequency spectrum at the RF driving frequency for the r1 and r2 magnetic sense coils versus wavenumber of the Nagoya III (red) and NSH19 (blue) at several magnetic fields. The driving frequency was 8.5 MHz, the pressure was 3.6 mTorr, and the RF power was 750 Watts.

delivered to both antennas. Power spectra are shown for magnetic fields of 390 G, 540 G, 690 G, 840 G, 1000 G, and 1150 G. Not only does the azimuthal wavenumber spectrum of the NSH19 antenna at 8.5 MHz change significantly with increasing magnetic field, the amplitude of the power spectrum at 8.5 MHz also changes with magnetic field. As the magnetic field increases from 1000 G to 1150 G, the amplitude of the power spectrum at the second harmonic increases sharply for both antennas. At 1150 G, the second harmonic has nearly the same amplitude as the fundamental. This transition occurs at the same magnetic fields as the transition in parallel wavenumber (Figure 46).

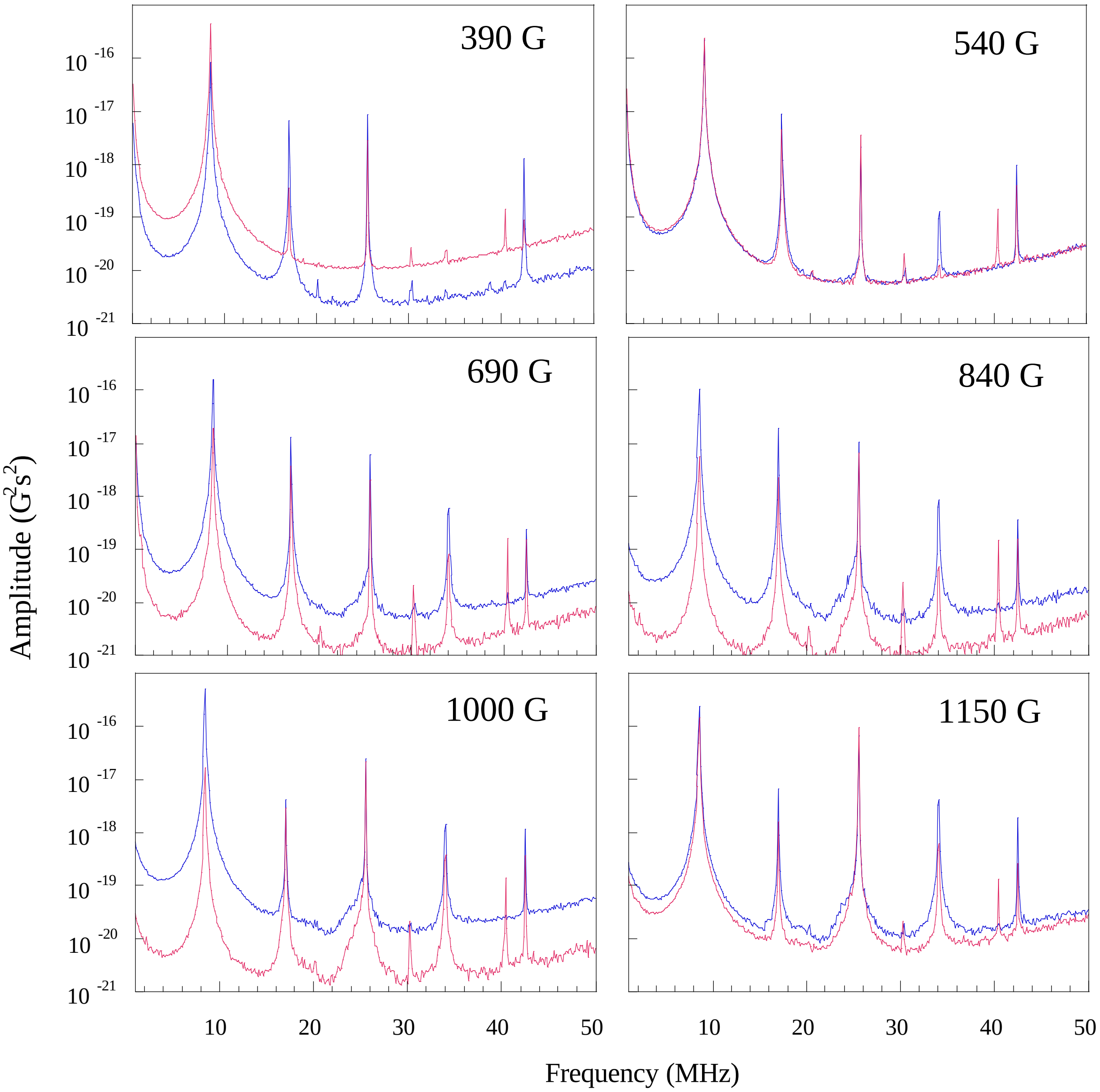

Figure 48. An average of fifty power spectra for the Nagoya III (red) and NSH19 (blue) antennas at various magnetic field strengths for a pressure of 3.6 mTorr, a driving frequency of 8.5 MHz, and a RF power of 750 W.

At 390 G, the power at all frequencies for the Nagoya III antenna is greater than the power for the NSH19. It is worth noting that at 390 G, the Nagoya III antenna also generates higher ion temperatures than the NSH19 antenna (Figure 41). At 540 G, the power at all frequencies is the same for both antennas (Figure 48). At 540 G the ion temperatures generated by both antennas are also equal (Figure 41). Above 540 G, the spectral power for the NSH19 antenna is significantly larger than for the Nagoya III except at the maximum field of 1150 G. From 540 G to 1000 G, the difference in power at all frequencies increases with increasing magnetic field.

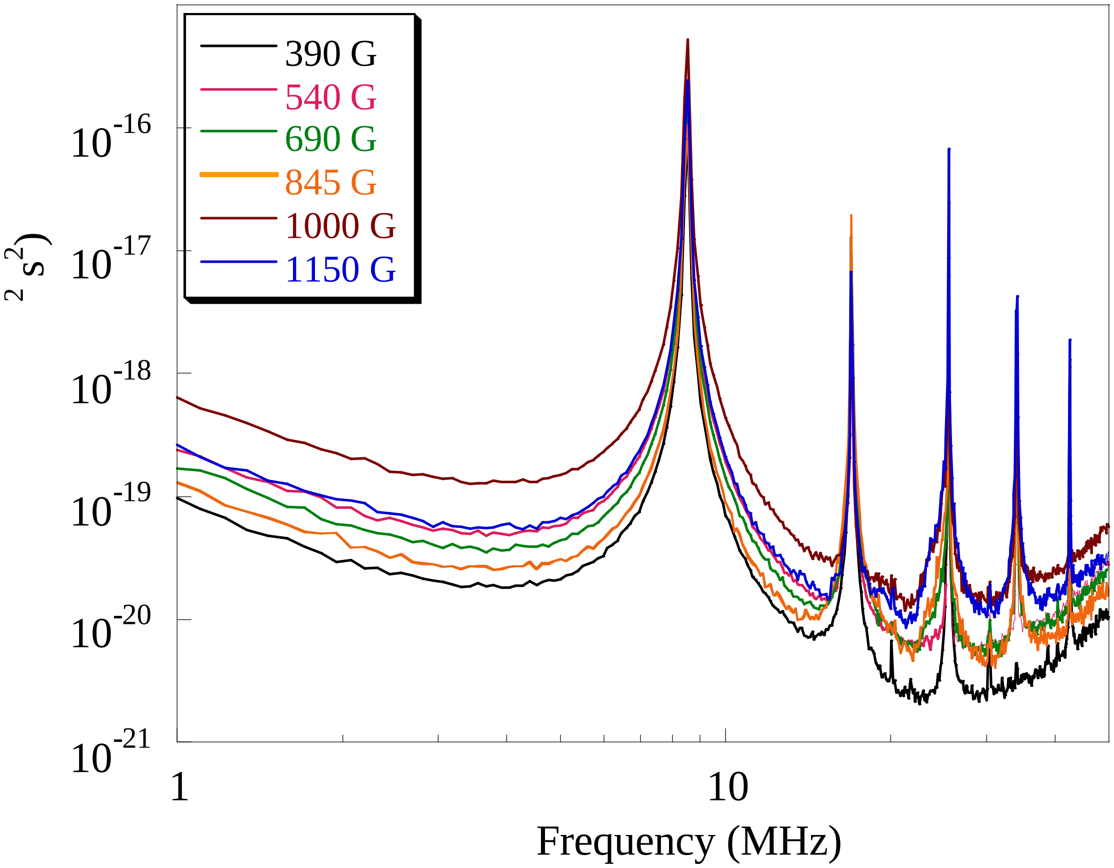

Figure 49. Power spectrum for the NSH19 antenna as a function of magnetic field strength for an RF power of 750 W, a driving frequency of 8.5 MHz and a pressure of 3.6 mTorr.

At 1150 G, the power at all frequencies is the nearly same for both antennas, but the power spectrum for the NSH19 antenna shows significant broadening around harmonics of the fundamental frequency. Just the power spectra for the NSH19 antenna are shown as a function of magnetic field in Figure 49. At a magnetic field of 1150 G, the power at the driving frequency drops slightly, resulting in similar amplitudes for the fundamental and second harmonic. Broadening of the harmonics with increasing magnetic field strength can also be seen in Figure 49. Enlarged to more clearly show the spectral broadening, the portion of the power spectrum for the second harmonic as a function of magnetic field is shown in Figure 50 for the NSH19 antenna. Note that the broadening of the second harmonic is asymmetric. The spectral widening is greater for lower frequencies than higher frequencies. Given that the highest magnetic field strengths correspond to the highest ion temperatures for a driving frequency of 8.5 MHz, these data suggest a correlation between spectral broadening of the harmonics, the drop in power spectral amplitude at the fundamental, and intense ion heating.

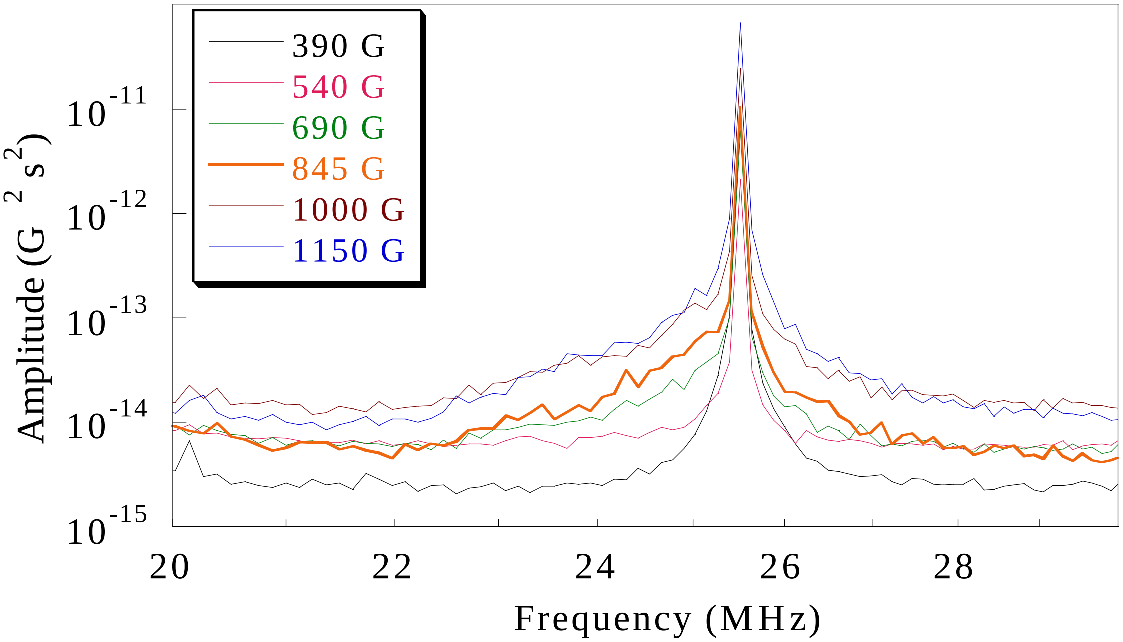

Figure 50. The power in the second harmonic for the NSH19 antenna for a range of magnetic fields, a driving frequency of 8.5 MHz, a RF power of 750 W, and a pressure of 3.6 mTorr.

## 5.0 DISCUSSION

The reengineering of the matching circuit antenna was critical to the success of these experiments. Components in the matching circuit and antenna are no longer prone to failure due to resistive heating. The increased efficiency results in higher densities at the same forward power than were possible with the original matching circuit and antenna. The decreased resistance in the antenna and circuitry, the balancing of the matching circuit (elimination of the ground), and the change in the location of the transmission line junction to the antenna clearly improved the efficiency of the source (Figure 35). In addition, HELIX can operate in steady state for extended periods at significantly higher powers ( > 1500 Watts). Such power levels would have resulted in catastrophic failure of electrical components in the previous matching circuit and antenna.

One possible impediment to the widespread use of helicon sources for high aspect ratio etching are the high perpendicular, $T_i \approx 1$ eV, intrinsic ion temperatures in low pressure, argon, helicon plasmas (Figure 41). Therefore, helicon sources may be prone to the same over-etching problems that plague high-pressure plasma sources despite their low operating pressures. These experiments unequivocally demonstrate that high perpendicular ion temperature in helicon sources can be avoided without sacrificing plasma density by an appropriate choice of operating parameters and antenna. For example, the perpendicular ion temperature for the NSH19 antenna was only 0.2 eV at a magnetic field of 700 G and a driving frequency of 12 MHz. At these parameters, the downstream density was maximized and the perpendicular ion temperature was only 20% of the peak ion temperature observed. For plasma etching applications, this choice of parameters and antenna is clearly advantageous. For plasma chemistry control, where the electron temperature is a key parameter, it may be desirable to operate at a slightly higher driving frequency where the electron temperature varies strongly with magnetic field and driving frequency.

These experiments demonstrate a clear correlation between the lower hybrid resonance, electron density production, and ion temperature in helicon sources. Collisional equilibration with electrons is clearly not responsible for the ion heating observed in helicon sources. The ion temperature peaks at source parameters that yield reduced electron temperatures and plasma densities. By operating a helicon source at frequencies slightly below the lower hybrid frequency, maximum perpendicular ion temperatures are generated at moderate plasma densities. To reduce the perpendicular ion temperature, the helicon source can be operated at higher frequencies, lower magnetic fields, or with an antenna that is less effective at coupling energy into the ions, e.g., a Nagoya III antenna. The penalty will be a reduced plasma density. The experimental data also indicate that narrow strap antennas couple energy into ions and electrons more cleanly, i.e., the regions of peak density production and peak ion heating are well defined and more uniform.

Helical, $m = +1$ antennas, couple power to the plasma more efficiently than Nagoya III antennas. Supporting this conclusion are the density measurements for the NSH19 and Nagoya III antennas (Figure 41). Both antennas are the same length and have comparable inductances (same electrical characteristics), thus the higher densities generated by the NSH19 antenna must be due to the difference in antenna shape. The two 19 cm long $m = +1$ antennas produce higher densities and greater ion temperatures than the 30 cm long $m = +1$ antenna (Figure 41). The parallel wavenumber measurements (Figure 46), indicate that the NSH19 and the WSH19 antennas launch waves with wavelengths closer to their expected values than the NSH30 antenna, i.e., the antenna length does not set the wavelength in the plasma. The wavelength in the plasma is determined by the dispersion relationship that governs the propagation of the RF wave. Since coupling to a resonant system is always more efficient when the external excitation is at the same frequency, or mode, as the natural modes in the system, the better power coupling to the plasma by the shorter $m = +1$ antennas is expected given the parallel wavenumber measurements. The parallel wavenumbers measured at the edge of the plasma suggest an antenna length of 7 cm would result in further improvements in efficiency.

That the regions of increased density and increased ion temperature lie on opposite sides of the $2pf = w_{LH}$ curve, suggests that the mechanisms responsible for coupling energy into the ions and electrons are fundamentally different in a helicon source. The magnetic field and RF frequency dependence of the electron density clearly indicates a correlation between density production and the lower hybrid frequency. Such trends are consistent with previous experiments [*Boswell*, 1984; *Yun et al.*, 1997; *Kwak et al.*, 1997; *Cho*, 2000]. However, these experiments are the first evidence of a correlation between ion temperature and lower hybrid frequency (Figure 44). Previous measurements only reported a correlation between ion temperature and magnetic field strength [*Scime et al.*, 1998]. The data in Figure 44 clearly show that the ion temperature is correlated with lower hybrid frequency and not magnetic field strength.

For many years, experimentalists attempting to heat plasmas have launched waves at frequencies slightly greater or less than the lower hybrid frequency [*Porkolab et al.*, 1977]. Those experiments rely on either direct absorption mechanisms to couple energy into ions or electrons, or parametric decay processes to generate lower frequency waves that can directly heat ions [*Cairns*, 1991]. For strong direct damping of lower hybrid waves on ions (electrons), the perpendicular (parallel) wave phase velocity must be comparable to the ion (electron) thermal speed [*Wegrow*, 1983]. Near the lower hybrid resonance, the perpendicular wavenumber becomes large. Thus, it is conceivable that the RF waves could directly damp on ions in a helicon source near the lower hybrid frequency. Such models of ion heating are consistent with observations of strongly anisotropic ion temperatures (Figure 14) [*Scime et al.*, 1998, *Keiter et al.*, 2000].

One possible explanation for the decrease in the amplitude of the power spectrum at the fundamental for high magnetic field strengths (Figure 49) is that at the lower hybrid frequency, electron cyclotron waves (the "TG" wave) become electrostatic and are no longer detectable by the magnetic sense coils around HELIX. With regards to the difference between the driving frequencies at which the ion temperature is the largest and the actual lower hybrid frequency, collisions typically introduce a shift in resonant frequency [*Stix*, 1992]

$$w' = w_o - in . \tag{23}$$

Consistent with the hypothesis that the NSH19 antenna generates a TG wave at the edge of the plasma that then directly damps on the ions at the lower hybrid resonance, are the higher azimuthal wavenumbers that appear in the wavenumber spectrum of the NSH19 antenna at high magnetic fields. Future experiments could confirm the growth of electrostatic lower hybrid waves in HELIX at these parameters with a series of electrostatic fluctuations measurements.

The other potential heating mechanism, parametric decay processes, may also occur if both a helicon and a TG wave exist in HELIX at the same frequency. In a parametric decay process, two waves exchange energy and momentum with a third wave. Energy (momentum) conservation demands that the sum of the frequencies (momenta) of the two waves equals the frequency (momentum). In this scenario, a helicon wave and a TG wave, both at the RF driving frequency, couple energy into harmonics of the RF driving frequency. One characteristic of parametric decay processes, as seen in Figure 50, is an asymmetric broadening of the power spectrum. *Imai et al.* [1979] reported similar asymmetric broadening at the harmonics of the driving wave during lower hybrid heating experiments in a tokamak. Confirmation of parametric decay processes requires wavenumber measurements that clearly show momentum conservation between three waves, i.e., $k_1 + k_2 = k_3$.

The data in this dissertation cannot provide absolute proof that parametric decay processes are involved in the ion heating that occurs for driving frequencies below the lower hybrid frequency. Azimuthal wavenumbers greater than $m = +2$ cannot be measured given the spacing of the magnetic sense coils. Higher order modes are clearly excited in HELIX by the NSH19 antenna (Figure 47) but determination of the true azimuthal wavenumber spectrum will require a set of probes with a smaller separation. The parallel wavenumber and frequency spectrum presented in Figure 47 shows evidence of frequency and parallel wavenumber conservation. In Figure 47, two distinct wavenumbers are measured at the fundamental frequency and the wavenumber of the first harmonic is equal to the difference of the two wavenumbers at the driving frequency. However, because of the aliasing issues discussed previously, similar results were not obtained for the azimuthal wavenumber measurements.

Finally, recent experiments in a modified version of HELIX lend additional support to the conclusion that surface waves play a key role in the ion heating process. In the modified version of HELIX, the glass vacuum chamber has been replaced with a mostly stainless steel vacuum chamber. Only the portion of the chamber under the RF antenna is glass. Ion temperature measurements in the modified HELIX experiment show a dramatic reduction in the ion temperature when the outer edge of the upstream plasma is blocked with a ceramic limiter [*Soulsby et al.*, 2000; *Scime*, private communication]. Future experiments will continue to explore the relationship between the edge physics in helicon sources and ion heating.

## 6.0 BIBLIOGRAPHY

Akhiezer A., Mikhailenko V. S. and Stepanov K. N., “Ion-sound parametric turbulence and anomalous electron heating with application to helicon plasma sources,” *Phys. Letters A.* vol. 245, p. 117, 1998.

Appleton E. V., "Wireless studies of the ionosphere," *J. Inst. Elec. Engrs.*, vol. 71, p. 642, 1932.

Assadi S., “Measurement of Magnetic Turbulence Structure and Nonlinear Mode Coupling of Tearing Fluctuations in the Madison Symmetric Torus Reversed Field Pinch,” Ph.D. Dissertation, University of Wisconsin, Madison, 1994.

Barkhausen H., “Whistling tones from the earth,” *Proc. I.R.E.*, vol. 18, p.143, 1930.

Bashkin S. and Stoner J. O., Atomic Energy Levels and Grotrian Diagram, N. Holand, 1975.

Beall J. M., Kim Y. C., and Powers E. J. "Estimation of wavenumber and frequency spectra using fixed probe pairs," *J. Appl. Phys.*, vol. 53, p. 3993. 1982.

Booker H. G., "Propagation of wave-packets incident obliquely upon a stratified double refracting ionosphere," *Philos. Trans. R. Soc. London A, Math. Phys. Sci.*, vol. 237A, p. 411, 1938.

Borg G. G., and Boswell R., W., “Power coupling to helicon and Trivelpiece-Gould modes in helicon sources,” *Phys. Plasmas*, vol. 5, p. 564, 1998.

Boswell R. W., "Plasma production using a standing helicon wave," *Phys. Lett.*, vol. 33A, pp. 457-458, 1970.

Boswell R. W., “Dependence of helicon wave radial structure on electron inertia,” *Australian Journal of Physics*, vol. 25, no. 4 , p. 403, 1972.

Boswell R. W., “Very efficient plasma generation by whistler waves near the lower hybrid frequency,” *Plasma Phys. Control Fusion*, vol. 26, p. 1147, 1984.

Boswell R. W. and Porteous R. K., “Large volume, high density RF inductively coupled plasma,” *Appl. Phys. Lett.*, vol. 50, p. 1130, 1987.

Boswell R. W., Morey I. J., and Porteous R. K., “Wave phenomena preceding and during a beam-plasma discharge,” *J. Geo. Research*. vol. 94, no. A3, p. 2654, 1989.

Boswell R. W. and Chen F. F., "Helicons-The Early Years," *IEEE Transaction on Plasma* Science, vol. 25, no. 6, Dec. 1997.

Cairns R. A., *Radiofrequency heating of plasmas*, (Adam Hilger, Bristol, UK 1991).

Chen F. F., “RF production of high density plasmas for accelerators,” *Laser and Particle Beams*, vol. 7, p. 551, 1989.

Chen F. F., “Plasma ionization by helicon waves,” *Plasma Phys. Control. Fusion*, vol. 33, p. 339, 1991.

Chen F. F., “Experiments on helicon plasma sources,” *J. Vac. Sci. Technol. A.*, vol. 10, no. 4, p. 1389, 1992.

Chen F. F., “Helicon plasma sources,” UCLA internal report PPG-1506, 1994.

Chen F. F., “Nonlinear Diffusion in Magnetized Discharges,” *Plasma Sources Sci. Technol* vol. 7, p. 458, 1998.

Chen F. F. and Chevalier G., "Experiments on helicon plasma sources," *J. Vac. Sci. Technol. A*, vol. 10, p. 1389, 1992.

Chen F. F., and Decker C. D., "Electron Acceleration in Helicon Source," *Plasma Phys. Control. Fusion*, vol. 34, p. 635, 1992.

Chen F. F., Jiang X., Evans J. D., Tynan G. and Arnush D., "Low Field Helicon Discharges," UCLA Internal Report PPG 1564, 1996.

Chen F. F. and Boswell R. W., “Helicons-the past decade,” *IEEE Transactions on Plasma Science*, vol.25, no.6, p.1245, 1997.

Chen F. F., Jiang X, Evans J. D., Tynan G., and Arnush A., “Low-field helicon discharges,” *Plasma Phys. Control. Fusion*, vol. 39, p. A411, 1997.

Chen F. F. and Blackwell D. D., “Upper limit to Landau damping in helicon discharges,” *Phys. Rev. Lett.*, vol. 82, p. 2677, 1999.

Chen R. T. S., Breun R. A., Gross S., Hershkowitz N., Hsieh M. K. J., and Jacobs J., “Experimental studies of multimode helicon plasma waves,” *Plasma Sources Sci. Technol* vol. 4, p. 337, 1995.

Chevalier G., and Chen F. F., “Experimental modeling of inductive discharges,” *J. Vac. Sci. Technol. A*, vol. 11, p. 1165, 1993.

Cho S. “The role of the lower hybrid resonance in helicon plasmas,” *Phys. Plasmas*, vol. 7, p. 417, 2000.

Chu C., Dawson J. M., and Okuda H., “Plasma heating at frequencies near the lower hybrid,” *Phys. of Fluids*, vol. 19, no. 7 1976.

Conrads H., and Schmidt M., “Plasma generation and plasma sources,” *Plasma Sources Sci. Technol.*, vol. 9, p. 441, 2000.

Degeling A. W. and Boswell R. W., “Modeling ionization by helicon waves,” *Phys. Plasmas*, vol. 4, p. 2748, 1997.

Ellingboe A. R., Boswell R. W., Booth J. P., and Sadeghi N., “Electron beam pulses produced by helicon-wave excitation,” *Phys. Plasmas*, vol.2, no.6, p.1807, 1995.

Ellingboe A. R. and Boswell R. W., “Capacitive, inductive and helicon-wave modes of operation of a helicon plasma source,” *Phys. Plasmas*, vol.3, no.7, p.2797, 1996.

Gallet R. M., Richardson J. M., Wieder B., and Ward G. D., "Microwave whistler mode propagation in a dense laboratory plasma," *Phys. Rev. Lett.*, vol. 4, p. 347, 1960.

Guo X. M., Scharer J., Mouzouris Y., and Louis L., “Helicon experiments and simulations in nonuniform magnetic field configurations,” *Phys Plasmas*, vol. 6, p. 3400, 1999.

Godyak V A, Piejak R B and Alexandrovich B., “Probe diagnostics of non-Maxwellian plasmas,” *J. Appl. Phys.* vol. 73, p. 3657, 1993.

Hartree D. R., "The propagation of electromagnetic waves in a refracting medium in a magnetic field," *Proc. Cambridge Phil. Soc.*, vol. 27, p. 143, 1931.

Heald M.A., and Warton C. B., *Plasma Diagnostics with Microwaves* (John Wiley & Sons Inc., New York 1965).

Hershkowitz N. and Harper M. K., “Elimination of notching and ARDE by simultaneous modulation of source and wafer RF,” *Proc. 26th IEEE Int. Conf. On Plasma Sci.* p. 127, 1999.

Hill D. N., fornaca S., and Wickham M. G., “Single frequency scanning laser as a plasma diagnostic,” *Rev. Sci. Instrum.*, vol. 54, p. 309, 1983.

Huba J. D. NRL Plasma Formulary (Naval Research Laboratory, Washington D.C.).

Hutchinson I. H., *Principles of Plasma Diagnostics* (Cambridge University Press, Cambridge 1987).

Imai T., Nagashima T., Yamamoto T., Uehara K., Konoshima S., Takeuchi H., Yoshida H., and Fujisawa N., “Parametric instabilities in lower-hybrid-frequency heating of a tokamak,” *Phys. Rev. Lett.*, vol. 43, no 8, p. 586, 1979.

Jiwari N., Iwasawa H., Narai A., Sakuae H., Shoji T., and Horike Y., *Jpn. J. Appl. Phys.*, vol. 32, p. 3019, 1993.

Kamenski I. V. and Borg G. G., “An evaluation of different antenna designs for helicon wave excitation in a cylindrical plasma source,” *Phys. Plasmas,* vol. 3, p. 4396, 1996.

Keiter P. A., *Frequency dependent Effects in Helicon Plasmas*, M.S. Thesis, West Virginia University, 1996.

Keiter P. A., *Experimental Investigation of Ion Temperature Anisotropy Driven Instabilities in a High Beta Plasma*, Ph.D. Disertation, West Virginia University, 1999.

Keiter P. A., Scime E. E., and Balkey M. M., "Frequency dependent effects in helicon plasmas," *Phys. Plasmas,* vol. 4, p. 2741, 1997.

Kim J. H., and Chang H. Y., “A study on ion energy distribution functions and plasma potentials in helicon wave plasmas,” *Phys. Plasmas* vol. 3, p. 1462, 1996.

Kline J. L., Scime E. E., Keiter P A, Balkey M. M., and Boivin R. F., “Ion heating in the HELIX helicon plasma source,” *Phys. Plasmas* vol. 6 p. 4767, 1999.

Kwak J. G., Choi H. D., Bak H. I., Cho S., Bak J. G., and Kim S. K., "Frequency dependence of the plasma density for helicon plasmas," *Phys, Plasmas*, vol. 4, p. 417, 1997.

Lieberman M. A. and Lichtenberg A. J. *Principles of Plasma Discharges and Materials Processing*, (John Wiley and Sons, Inc. New York, 1994).

Light M. and Chen F. F., ‘Helicon wave excitation with helical antennas,” *Phys. Plasmas*, vol. 2, p. 1084, 1994.

Light M., Sudit I. D., Chen F. F. and Arnush A., “Axial propagation of helicon waves,” *Phys. Plasmas*, vol. 2, p. 4094, 1995.

Loewenhardt P. K., Blackwell B. D., Boswell R. W., Conway G. D., Hamberger S. M., “Plasma production in a toroidal heliac by helicon waves,” *Phys. Rev. Lett.*, vol.67, no.20, p.2792, 1991.

Loewenhardt P. K., Blackwell B. D., Beichao Z., “A simple miniature magnetic probe with inherent electrostatic rejection (for plasma diagnostics),” *Rev. Sci.. Instrum.*, vol.64, no.11, 1993.

McWilliams R., Hill D. N., Wolf N. S., and Rynn N., “Cross-field ion transport and heating due to parametric decay of lower hybrid waves,” *Phys. Rev. Lett.*, vol. 50, no. 11, p. 836, 1983.

Molvik A. W., Ellingboe A. R., Rognlien T. D., “Hot-electron production and wave structure in a helicon plasma source,” *Phys. Rev. Lett.*, vol.79, no.2, p.233, 1997.

Nakano T., Giapis K. P., Gottscho R. A., Lee T. C., and Sadeghi N., “Ion velocity distributions in helicon wave plasmas: magnetic field and pressure effects, “ *J. Vac. Sci. Technol. B*, vol. 11, p. 2046, 1993.

Nakano T., Ohtake H., and Samukawa S., “Ion and neutral temperatures in a novel ultrahigh-frequency discharge plasma,” *Jpn. J. Appl. Phys. Part 2 (Letters)*, vol. 35, p. L338, 1996.

Perry A. J., and Boswell R. W., “Fast anisotropic etching of silicon in an inductively coupled plasma reactor,” *App. Phys. Lett.*, vol. 55, no. 2, p. 148, 1989.

Perry A. J., Vender D, and Boswell R. W., “The application of the helicon source to plasma processing,” *J. Vac. Sci. Technol. B.*, vol. 9, no. 2, p. 310, 1991.

Porkolab M., Bernabei S., Hooke W. M., and Motley R. W., “Obserbation of parametric instabilities in lower-hybrid radio-frequency heating of tokamaks,” *Phys. Rev. Lett.*, vol. 38, no5, p. 230, 1977.

Scime E. E., Keiter P. A., Zintl M. W., Balkey M. M., Kline J. L., and Koepke M. E., "Control of ion temperature anisotropy in a helicon plasma," *Plasma Sources Sci. Technol.*, vol. 7, p. 186, 1998.

Scime E. E., Boivin R. F., Balkey M. M., Kline J. L., “Microwave interferometer for steady-state plasmas,” *submitted to Rev. Sci. Instrum.*, 2000.

Shamrai K. P. and Taranov V. B., "Resonance wave discharge and collisional energy absorption in helicon plasma source," *Plasma Phys. and Control Fusion*, vol. 36, p. 1719, 1994

Shamrai K. P., Taranov V. B., “Resonances and anti-resonances of a plasma column in a helicon plasma source,” *Phys. Lett. A.*, vol. 204, p. 139, 1995.

Shoji T., Sakawa Y., Nakazawa S., Kadota K., and Sato T., “Plasma production by helicon waves,” *Plasma Sources Sci. Technol.*, vol. 2, p. 5, 1993.

Soulsby R.C., Kent B.R., Balkey M.M., Boivin R.F., Kline J.L., and Scime E.E., “Two-dimensional measurements of ion temperature in a helicon plasma source,” Bulletin of the American Physical Society vol. 45, no. 7, 2000.

Stepanov K. N., “Nonlinear parametric phenomena in plasma during radiation frequency heating in the ion cyclotron frequency range,” *Plasma Phys. Contro. Fusion*, vol. 38, p. A13, 1996.

Stern R., and Johnson J., “Plasma ion diagnostics using resonant fluorescence,” *Phys. Rev. Lett.*, vol. 34, p. 1548, 1975.

Stix T. H., *Waves in Plasmas*, (American Institute of Physics, New York 1992).

Storey L. R., “An investigation of whistling atmospherics,” *Philos. Trans. R. Soc. London A, Math. Phys. Sci.*, vol. 237A, p. 411, 1938.

Storey L. R., "An investigation of whistling atmospherics," *Philos. Trans. R. Soc. London A, Math Phys. Sci.*, vol. 246, p. 113, 1953.

Sudit I. D., and Chen F. F., “RF compensated probes for high-density discharges,” *Plasma Sources Sci. Technol.*, vol. 3, p. 162, 1994.

Sudit I. D., and Chen F. F., “Discharge equilibrium of a helicon plasma,” *Plasma Sources Sci. Technol.* vol.5, no.1, p.43, 1996.

Wegrow J. G., and Tonog G., *Non-Inductive Current Drive in Tokamaks, Proc. IEAE Technical Committee, Culham Laboratory,* 1983.

Yun S-M, Kim J-H, and Chang H-Y, “Frequency dependence of helicon wave plasmas near lower hybrid resonance frequency,” *J. Vac. Sci. Technol. A*, vol. 15, p. 673, 1997.

Yun S. M. and Chang H. Y., “Radial density profile change near lower hybrid frequency in M=0 helicon wave plasmas,” *Phys. Lett. A*, vol. 248, p. 400, 1998.

Zhu P. and Boswell R. W., “Ar II laser generated by Landau damping of whistler waves at the lower hybrid frequency,” *Phys. Rev. Lett.*, vol.63, no.26, p.2805, 1989.

Zhu P. and Boswell R. W. “A new argon-ion laser based on an electrodeless plasma,” *J. Appl. Physics,* vol. 68, no. 5, p. 1981, 1990.

Zhu P. and Boswell R. W., “Observation of nonthermal electron tails in an RF excited argon magnetoplasma,” *Phys. Fluids B.*, vol. 3, no. 4, p. 869, 1991.

# APPENDIX A

## Source Code CALIBRATE.C

```
#include <utility.h>
#include <analysis.h>
#include <ansi_c.h>
#include <high_freq_calib.h>
#include <parameters.h>

void calibrate_coil(void)
{
                double    reference[r_length];
                double    probe_signal[r_length];
                int                i;
                void      step_freq(int *,float *);
                void      delay_loop(float);
                void      get_data( double reference[r_length], double probe_signal[r_length],int );
                void      digitizer_setup(int ,float);
                char      coil[16];
//              float     lower_freq_limit;
//              float     upper_freq_limit;
                float     frequency;
                int                flag;
                int                freq_counter = 0;
                int       coil_min_index;
                double    coil_min;
                int       coil_max_index;
                double    coil_max;
                int       ref_min_index;
                double    ref_min;
                int       ref_max_index;
                double    ref_max;
                double    coil_ptp[231];
                double    ref_ptp[231];
                double    coil_area[231];
                double    helm_B;
                double    cross_sig[r_length/2];
                double    sig_phase[r_length/2];
                double    freq_int;
                int       cross_min_index;
                double    cross_min;
                int       cross_max_index;
                double    cross_max;
                double    phases[6000];
                double  time;

//              Define Output Files
                FILE      *sum_file;
                FILE      *raw_data_file;
                char      sum_name[128];
                char      raw_data_name[128];
                char      freq_number[32];

                GetCtrlVal (PANEL, PANEL_coil_box, &coil[0]);

//              strcpy(sum_name, "C:\\PlasmaData\\HF_Bdot_calib\\ReferenceCoil1\\");
                strcpy(sum_name, "C:\\PlasmaData\\HF_Bdot_calib\\ReferenceCoil2\\");
                strcat(sum_name, coil);
                strcat(sum_name, "\\");
                strcat(sum_name, coil);
                strcat(sum_name, ".sum");
```

```
        sum_file = fopen (sum_name, "w");
        fprintf (sum_file, "Coil PTP, Ref PTP, Coil Area, freq, Mag. Field, Phase\n");

do
            {
//      strcpy(raw_data_name, "C:\\PlasmaData\\HF_Bdot_calib\\ReferenceCoil1\\");
        strcpy(raw_data_name, "C:\\PlasmaData\\HF_Bdot_calib\\ReferenceCoil2\\");
        strcat(raw_data_name, coil);
        strcat(raw_data_name, "\\");
        strcat(raw_data_name, coil);
        strcat(raw_data_name, "_");
        sprintf (freq_number, "%i", freq_counter);
        strcat(raw_data_name, freq_number);
        strcat(raw_data_name, ".data");
        raw_data_file = fopen (raw_data_name, "w");

        fprintf (raw_data_file, "freq, reference signal, probe signal, time\n");
            step_freq(&freq_counter,&frequency);
            digitizer_setup(freq_counter,frequency);
            delay_loop(frequency);
            get_data( reference, probe_signal,freq_counter);
            for (i=0; i<r_length; i++)
            {
                time = (double) (i / d_rate);
                fprintf(raw_data_file, "%f, %lf,%lf, %e\n",   frequency,
                    reference[i],probe_signal[i],time);
            }

// Find Min and Max for reference signal
            MaxMin1D (reference, r_length, &ref_max, &ref_max_index,
               &ref_min,&ref_min_index);

// Find Min and Max for coil signal
            MaxMin1D(probe_signal, r_length, &coil_max, &coil_max_index, &coil_min,
                &coil_min_index);

// Find the Phase Spectrum at a particular frequency
            CrossPowerSpectrum (reference, probe_signal, r_length, 1/d_rate,cross_sig, sig_phase,
                &freq_int);
            MaxMin1D (cross_sig, r_length/2, &cross_max, &cross_max_index,
               &cross_min,&cross_min_index);
            phases[freq_counter] = sig_phase[cross_max_index];
//      index_freq = freq_int * (double)cross_max_index;

// Calculate the Peak to Peak Voltages for each signal
            ref_ptp[freq_counter] = fabs(ref_max) + fabs(ref_min);
            coil_ptp[freq_counter] = fabs(coil_max) + fabs(coil_min);

// Calculate the Magnetic field from the coil
            helm_B = YINT + SLOPE * ref_ptp[freq_counter]/COIL_RES ;

// Calculate the Effective Area of the coil at a particular frequency
            coil_area[freq_counter] = 1e10 * coil_ptp[freq_counter] / (helm_B * 6.28 * frequency);

// Save the Coil Area
            fprintf(sum_file, "%f,%f,%f,%f,%f,%f\n", coil_ptp[freq_counter], ref_ptp[freq_counter],
                coil_area[freq_counter], frequency, helm_B, phases[freq_counter]);
            fclose (raw_data_file);
            freq_counter = freq_counter+1;
        }
        while (freq_counter < count_max);
        fclose (sum_file);
```

## Source Wavetek.c

```
#include <utility.h>
#include <ansi_c.h>
#include <gpib.h>
#include <parameters.h>

static int wavetek_gpib;

//wavetek_gpib is the value that refers the computer to the wavetek function generator

/*The procedure wavetek_setup is called from the main program. It connects to the wavetek function generator and
initializes it for coil calibration. The function generator is set to generate a sine wave at a frequency of 0.5 MHz with an
amplitude of 500 mV.The function generator is then set to display frequency on it's led and the final line in the
procedure takes the function generator out of standby mode.*/

void wavetek_setup()
{
        wavetek_gpib = OpenDev("wavetek","");
        ibwrt (wavetek_gpib, "w1", 3);
        ibwrt (wavetek_gpib, "frq 6.0e+ 6", 12);
        ibwrt (wavetek_gpib, "amp 160.0e- 1", 13);
        ibwrt (wavetek_gpib, "vfrq", 4);
        ibwrt (wavetek_gpib, "d0", 3);
}
/*The function step_freq is called from the function calibrate_coil. This function changes the frequency of the wavetek
function from the lower limit to the upper limit. These limits are chosen by the user in the user interface. When the
upper limit is reached this function returns a value 0 which will terminate the do while loop in the function
calibrate_coil.*/

        void step_freq(int *freq_number, float *frequency){

        char freq_string[64];
        char amp_string[64];
        freq_array[0] = 22.0 * pow (10, 6);
        freq_array[1] = 27.0 * pow (10, 6);
        freq_array[2] = 30.0 * pow (10, 6);
        freq_array[3] = 35.0 * pow (10, 6);
        freq_array[4] = 38.0 * pow (10, 6);

        *frequency = freq_array[*freq_number];
        sprintf (freq_string, "frq %g/n", *frequency);
        ibwrt (wavetek_gpib, freq_string, 12);
}
void    delay_loop(float frequency)
{
        char freq_string[16];
        float actual_freq;
        do
        {
                Delay(1);
                ibwrt (wavetek_gpib, "frq?" , 4);
                ibrd (wavetek_gpib, freq_string, 13);
//              sscanf (freq_string, %s,%e/n, dummy,actual_freq);
                sscanf (&freq_string[4], "%8e",&actual_freq);
        }
        while (actual_freq < frequency);
```

## Source code Digitizer.c

```
#include <visa.h>
#include <ansi_c.h>
```

```
#include <TKTVS600.h>
#include <parameters.h>

/* Define Function for Displaying Error Messages */
//void      displayErr(ViSession InstrHndl,ViStatus err);
//void      get_data(float reference[], float probe_signal[]);
static      ViSession             digitizer_handle;
static      ViSession             defsesn;
static      ViSession             controller_hndl;

void displayErr(ViSession gInstrHndl,ViStatus err)
{
   char szErrMsg[256];
   tktvs600_error_message (gInstrHndl, err, szErrMsg);
   printf("%s\n", szErrMsg);
}

void Connect_to_digitizer()
{
            static      ViSession             result;
/*          Open VXI session */
//          result = viOpenDefaultRM (&defsesn);
/*          Find VXI controller */
//    result = viOpen (defsesn, "GPIB0::1::0", VI_NULL, VI_NULL, &controller_hndl);

/*          Find TVS600 instrument */
            if (result = tktvs600_autoConnectToFirst (&digitizer_handle))
   {
      displayErr(digitizer_handle,result);
   }
}

/* The function digitizer_setup connects to the TVS641 digitizer and opens a VXI
session and connects to the controller*/

void digitizer_setup(int freq_number, float freq)
{
            ViInt32 ave_num = 4;
            static      ViSession             result;
            ref_scale_array[0] =              10.0;
            ref_scale_array[1] =              8.00;
            ref_scale_array[2] =              3.00;
            ref_scale_array[3] =              3.60;
            ref_scale_array[4] =              3.60;
            probe_scale_array[0] = 0.40;
            probe_scale_array[1] = 0.20;
            probe_scale_array[2] = 0.40;
            probe_scale_array[3] = 0.30;
            probe_scale_array[4] = 0.22;
            d_rate = freq * 100;

            if (d_rate > 1e9)
            {
                        d_rate=1e9;
            }

/*          reset the device and clear status */
   if (result = tktvs600_sendCmd (digitizer_handle, "*RST;*CLS"))
   {
      displayErr(digitizer_handle,result);
   }
```

```
/*Set the vertical scale for the 4 channels of the 641*/
            tktvs600_setVert (digitizer_handle, TKTVS600_INP_CH1,
                                                    TKTVS600_INP_IMP_LO, TKTVS600_INP_AC_COUP,
                                                    TKTVS600_INP_BW_LOW, probe_scale_array[freq_number],
0.00);
            tktvs600_setVert (digitizer_handle, TKTVS600_INP_CH2,
                                                    TKTVS600_INP_IMP_LO, TKTVS600_INP_AC_COUP,
                                                                TKTVS600_INP_BW_HIGH,
            ref_scale_array[freq_number], 0.00);
/*          tktvs600_setVert (digitizer_handle, tktvs600_INP_CH3,
                        tktvs600_INP_IMP_LO,tktvs600_INP_AC_COUP,
                        tktvs600_INP_BW_FULL, 1.00, 0.00);

            tktvs600_setVert (digitizer_handle, tktvs600_INP_CH4,
                        tktvs600_INP_IMP_LO, tktvs600_INP_AC_COUP,
                        tktvs600_INP_BW_FULL, 1.00, 0.00);
            tktvs600_setHorz (digitizer_handle, d_rate, r_length,
                                                                            TKTVS600_HORZ_TP_REC, 0.0);
/*          Set up the acquisition style*/
            tktvs600_setAcq (digitizer_handle, TKTVS600_ACQ_TYPE_NORMAL, ave_num,
                        TKTVS600_ACQ_FORMAT_INT16, TKTVS600_ACQ_BORD_SWAPPED);  /* swap hi/lo
                        bytes for intel compatibility */

/*          Set up the trigger format*/
            tktvs600_setMainEdgeTrigger (digitizer_handle, tktvs600_TRIG_SOUR_CH2,
                        0.0, tktvs600_TRIG_SLOP_POS,tktvs600_TRIG_COUP_ACNR);
            tktvs600_setAcqActiveChannel (digitizer_handle,TKTVS600_ACQ_SRC_CHS12);
}

void get_data( double reference[], double probe_signal[], int freq_number)
{
            ViInt32 numblocks;
            ViInt32 retcnt;
            ViInt32 acquire_delay = 1.0;
            ViInt16 nWaveData[2 * r_length];
            int i;

            for (i = 0; i<r_length; i++)
            {
                        nWaveData[i]=0;
                        nWaveData[i+r_length]=0;
            }

            tktvs600_readWaveforms (digitizer_handle, nWaveData,
                        TKTVS600_IO_WS_PROT, TKTVS600_ACQ_SRC_CHS12,
                        acquire_delay, &retcnt, &numblocks);

            for (i = 0; i<r_length; i++)
            {
                        probe_signal[i] = (double)(probe_scale_array[freq_number] * nWaveData[i]/(2*32256));
                        reference[i] = (double)(ref_scale_array[freq_number] * nWaveData[i + r_length]/(2*32256));
            }
}
```

## APPENDIX B

### Header WAVE.H

```
#define MAX_RLENGTH 8192
#define PI      3.1415926535897932

int main_panel;
```

```
int fft_panel;
int cross_panel;
int menu_handle;

void free_dmatrix( double **, int , int );
double **dmatrix(int, int);
double **analyze(double Theta[MAX_RLENGTH], double cross[MAX_RLENGTH],
        double ave_wave1_pow[MAX_RLENGTH],
double ave_wave2_pow[MAX_RLENGTH],
        double freq[MAX_RLENGTH]);
void Find_k (double wave1[MAX_RLENGTH], double wave2[MAX_RLENGTH], double Theta[MAX_RLENGTH],
        double cross[MAX_RLENGTH],
                    double wave1_pow[MAX_RLENGTH],double wave2_pow[MAX_RLENGTH],
        double **S, double freq[MAX_RLENGTH]);
void Get_Colors(ColorMapEntry *, double );
int  getfiledata( double **array1, char filename1[256], int num_points, int cols);
void cross_plot(double Theta[MAX_RLENGTH], double cross[MAX_RLENGTH],
        double freq[MAX_RLENGTH]);
void fft_plot( double wave1_pow[MAX_RLENGTH],double wave2_pow[MAX_RLENGTH],
        double freq[MAX_RLENGTH]);
void intensity_plot(double **S, double freq[MAX_RLENGTH]);
void run_min_max_check( int panel, int control, int eventData1, int eventData2 );
void writefile(double **S, double ave_wave1_pow[MAX_RLENGTH], double ave_wave2_pow[MAX_RLENGTH]);
void set_plot_area( int panel, int control, int event, int eventData1, int eventData2 );
void run_coil_correction(double **array, int coil, int max_data_length, int cols);
int getfileinfo( char filename[256], int *cols, int *num_points);
double max2d( double **Z, int minx, int maxx, int miny , int maxy);
```

## Source Code Kspectrum.c

```
/***********************************************************************
 *   Program        :  K spectrum analysis                                   *
 *   Writen By      :  John Kline with analysis routine by Paul Keiter*
 *   Date Alpha version :  4/26/2000                                          *
 *                                                                                                    *
 *                       This program analyzes data from two files containing columns of  time series data producing      *
 *   a two dimensional K spectrum array, frequency vs K.         *
 *                                                                                                    *
*********************************************************************/

#include <ansi_c.h>
#include <userint.h>
#include <formatio.h>
#include <analysis.h>
#include <stdio.h>
#include <Kspectrum.h>
#include <wave.h>

// These variables are global for plotting purposes
static double Theta[MAX_RLENGTH];                                        // Theta is phase between two time
                        signals
static double cross[MAX_RLENGTH];                               // Power of cross power spectrum for two time
                        signals
static double ave_wave1_pow[MAX_RLENGTH];                       // Average fft of time series 1
static double ave_wave2_pow[MAX_RLENGTH];                       // Average fft of time series 2
      double **Sdata;                                                                  // Spectral density
                        for omega vs K
static double freq[MAX_RLENGTH];                                // Frequency axis

//int first_run_flag=0;   // This flag lets the progam know if it is the first
                      // through the program.  It is used in dereferencing
                      // pointer arrays.

void main()
 {
   // Main routine.  It just launched the panels and runs the user interface.


   fft_panel = LoadPanel (0, "Kspectrum.uir", FFTS);
   DisplayPanel(fft_panel);
   cross_panel = LoadPanel (0, "Kspectrum.uir", CROSS);
   DisplayPanel(cross_panel);
   main_panel = LoadPanel (0, "Kspectrum.uir", PANEL);
   DisplayPanel(main_panel);
   menu_handle = LoadMenuBar (main_panel, "Kspectrum.uir", MAIN);
   RunUserInterface ();
 }

// quit button: quit program routine
int CVICALLBACK quit (int panel, int control, int event,
                                    void *callbackData, int eventData1, int eventData2)
{
                        switch (event)
                                    {
                                    case EVENT_COMMIT:
                                                QuitUserInterface(0);
                                                break;
                                    }
                        return 0;
}
```

```
// run button: run the analyze function
int CVICALLBACK run (int panel, int control, int event,
		void *callbackData, int eventData1, int eventData2)
{
			switch (event)
				{
				case EVENT_COMMIT:
					SetCtrlAttribute (panel, PANEL_REPLOT, ATTR_DIMMED, 0); // let replot
						button be used
					Sdata = analyze(Theta, cross, ave_wave1_pow, ave_wave2_pow, freq);
					break;
				}
			return 0;
}

// replot button: updates plot on plot panel on which the button was pushed
int CVICALLBACK replot (int panel, int control, int event,
				void *callbackData, int eventData1, int eventData2)
{
			switch (event)
				{
				case EVENT_COMMIT:
					if ( panel == fft_panel) fft_plot( ave_wave1_pow, ave_wave2_pow, freq);
					if ( panel == cross_panel) cross_plot(Theta, cross, freq);
					if (panel == main_panel) intensity_plot(Sdata, freq);
					break;
				}
			return 0;
}

int CVICALLBACK min_max_check (int panel, int control, int event,
				void *callbackData, int eventData1, int eventData2)
{
			switch (event)
				{
				case EVENT_COMMIT:
					break;
				case EVENT_LOST_FOCUS:
					run_min_max_check( panel, control, eventData1, eventData2 );
				   break;
				}
			return 0;
}

// This routine brings up a file selection popup when a right mouse click is done on file text box.
int CVICALLBACK file_slct (int panel, int control, int event,
				void *callbackData, int eventData1, int eventData2)
{
   char filename[260];
   int result;

			switch (event)
				{
				case EVENT_COMMIT:
					break;
				case EVENT_RIGHT_CLICK:
					result = FileSelectPopup ("", "*.*", "", "File Selection",
				      VAL_OK_BUTTON, 0, 0, 1, 1, filename);
					if (result != 0) SetCtrlVal(panel,control,filename);
					break;
				}
			return 0;
```

```
}

// Save_file button:  writes 2d spectral density array to a file
int CVICALLBACK Save_to_file (int panel, int control, int event,
                              void *callbackData, int eventData1, int eventData2)
{
                  switch (event)
                           {
                           case EVENT_COMMIT:
                                     writefile(Sdata,ave_wave1_pow,ave_wave2_pow);
                                    break;
                           }
                  return 0;
}

// If someone changes the number of kbins or the rlength, the replot function will use the new
// values to plot but this will not match the data array size unless the analyze function has
// been run.  This function dimms ( disallow use of) the replot function when either the kbins
// or rlength control has been changed and is undimmed ( allows use of ) when go button is pushed.
int CVICALLBACK no_plot (int panel, int control, int event,
                              void *callbackData, int eventData1, int eventData2)
{
                  switch (event)
                           {
                           case EVENT_COMMIT:
                                           SetCtrlAttribute (panel, PANEL_REPLOT, ATTR_DIMMED, 1);
                                    break;
                           }
                  return 0;
}

// print button:  prints the current panel from which the print button was pushed.
int print (int panel, int control, int event,
                              void *callbackData, int eventData1, int eventData2)
{
switch (event) {
    case EVENT_COMMIT:
                                    SetPrintAttribute (ATTR_BITMAP_PRINTING, 1);
                                    SetPrintAttribute (ATTR_COLOR_MODE, VAL_COLOR);
                                    SetPrintAttribute (ATTR_PRINT_FONT_NAME,
                  VAL_MESSAGE_BOX_META_FONT);
                                    SetPrintAttribute (ATTR_PRINT_AREA_HEIGHT,
                  VAL_USE_ENTIRE_PAPER);
                                    SetPrintAttribute (ATTR_PRINT_AREA_WIDTH,
                  VAL_USE_ENTIRE_PAPER);
                                    PrintPanel (panel, "", 0, VAL_FULL_PANEL, 0);
                                    break;
                           case EVENT_RIGHT_CLICK:
                                    break;
                  }
                  return 0;
}

void CVICALLBACK menu (int menuBar, int menuItem, void *callbackData,
                              int panel)
{
   char filename[260];
   int i;
   int result;
   int rlength;
   double drate;
   double deltaf;
```

```
FILE *outfft;
switch(menuItem) {

                    case MAIN_FILE_1:
                        result = FileSelectPopup ("", "*.*", "", "File Selection",
                        VAL_OK_BUTTON, 0, 0, 1, 1, filename);
                        if (result != 0) SetCtrlVal(panel,PANEL_FILE1,filename);
                                    break;
                    case MAIN_FILE_2:
                        result = FileSelectPopup ("", "*.*", "", "File Selection",
                        VAL_OK_BUTTON, 0, 0, 1, 1, filename);
                        if (result != 0) SetCtrlVal(panel,PANEL_FILE2,filename);
                                    break;
                    case MAIN_FILE_OUT:
                         result = FileSelectPopup ("", "*.*", "", "File Selection",
                         VAL_OK_BUTTON, 0, 0, 1, 1, filename);
                         if (result != 0) SetCtrlVal(panel,PANEL_OUTPUT,filename);
                                    break;
                    case MAIN_FILE_SAVEFFT2:
                         result = FileSelectPopup ("", "*.*", "", "File Selection",
                         VAL_OK_BUTTON, 0, 0, 1, 1, filename);
                         if (result != 0) SetCtrlVal(panel,PANEL_OUTPUT,filename);
                         GetCtrlVal (main_panel, PANEL_DRATE, &drate);
                         GetCtrlVal (main_panel, PANEL_RLENGTH, &rlength);
                  deltaf = drate/ (double) rlength;
                         outfft = fopen (filename, "w");
                         fprintf(outfft,"freq,fft series #1, fft series #2\n");
                         for( i=0; i<rlength;i++){
                                  printf(outfft,"%e,%e,%e\n",(double)i*deltaf,ave_wave1_pow[i],ave_wave2_pow[i]);
                    }
                                  fclose(outfft);
                                  break;
                    case MAIN_FILE_SPACE:
                                  result = FileSelectPopup ("", "*.WKS", "", "File Selection",
                                  VAL_OK_BUTTON, 0, 1, 1, 1, filename);
                                  if (result != 0)
                                                 {
                                                    SavePanelState (main_panel, filename, PANEL);
                                                    SavePanelState (fft_panel, filename, FFTS);
                                                    SavePanelState (cross_panel, filename, CROSS);
                                                 }
                                    break;
                    case MAIN_FILE_RECALL:
                                  result = FileSelectPopup ("", "*.WKS", "", "File Selection",
                                  VAL_OK_BUTTON, 0, 1, 1, 1, filename);
                                  if (result != 0)
                                                 {
                                                  RecallPanelState (main_panel, filename, PANEL);
                                                  RecallPanelState (fft_panel, filename, FFTS);
                                                  RecallPanelState (cross_panel, filename, CROSS);
                                                 }
                                    break;
                        case MAIN_PREF_RESCALE:
                                    GetMenuBarAttribute (menuBar, MAIN_PREF_RESCALE, ATTR_CHECKED,
                                                          &result);
                                    SetMenuBarAttribute (menuBar, MAIN_PREF_RESCALE, ATTR_CHECKED,
                                                          !result);
                                  break;
                        case MAIN_PREF_SAVEFFT:
                                    GetMenuBarAttribute (menuBar, MAIN_PREF_SAVEFFT, ATTR_CHECKED,
                                                          &result);
```

```
                         SetMenuBarAttribute (menuBar, MAIN_PREF_SAVEFFT, ATTR_CHECKED,
                                         !result);
                        break;
                }
}


int CVICALLBACK plot_area (int panel, int control, int event,
                        void *callbackData, int eventData1, int eventData2)
{
                switch (event)
                        {
                        case EVENT_COMMIT:
                                set_plot_area( panel,  control, event, eventData1, eventData2 );
                                break;
                        case EVENT_VAL_CHANGED:
                                set_plot_area( panel,  control, event, eventData1, eventData2 );
                                break;
                        }
                return 0;
}
```

## Source code ANALYSIS.C

```
/***************************************************************
 *                                                                                                   *
 *   Program           :  K spectrum analysis                                   *
 *   Writen By         :  John Kline with analysis routine by Paul Keiter*
 *   Date Alpha version :  4/26/2000                                            *
 •       This routine calculates K given two time series of data then puts the K in
  *    a 2d
 *   array of freq vs K.
 *
******************************************************************************/

#include <userint.h>
#include <analysis.h>
#include <ansi_c.h>
#include "wavelength.h"
#include <wave.h>

#define SCALE   1e15


void get_coil_info( double freq[MAX_RLENGTH], double ca1[MAX_RLENGTH],
                 double ca2[MAX_RLENGTH], double phase[MAX_RLENGTH]);



double **analyze(double Theta[MAX_RLENGTH], double cross[MAX_RLENGTH],
             double ave_wave1_pow[MAX_RLENGTH],double ave_wave2_pow[MAX_RLENGTH],
             double freq[MAX_RLENGTH])

 {

//  This is the main analysis loop.  It runs every time the go button is pushed.
//  It loops through all of the necessary functions to analyze the data pointed
//  to by the S pointer.


   static double **wave1;      //  pointer to a 2d array of time series for analysis
   static double **wave2;      //  pointer to a 2d array of time series for analysis
   static double **S;
   double wave1out[MAX_RLENGTH]; //  array used to pass a single time series to analysis routine
   double wave2out[MAX_RLENGTH];             //  array used to pass a single time series to analysis routine
   double srate;                             //  sampling rate variable
   double dist;                              //  coil separation distance
   int iterations;                           //  Number of time series to use in analysis
   int rlength;                              //  Number of points in time series to analyze
   int krlength;                             //  Number of points for K measuments
   int kbins;                                //  Number of fft bins to combine for K
   static int cols1;               //  Number of columns in Time series file
   static int cols2;               //  Number of columns in Time series file
   static int max_data_length1;
   static int max_data_length2;
   int i,j;                                  //  counters
   int coilnum1;
   int coilnum2;
   static int old_coilnum1;
   static int old_coilnum2;
   int result=0;                   //  generic result variable
   int klambda_flag;               //  flag to plot vs K or vs lambda
   static int old_rlength;//  Stores old value of rlength before processing
   static int old_krlength;//  Stores old value of Krlength before processing
```

```
    char coil1[260];                //  Path and filename used for data set 1
    char coil2[260];                //  Path and filename used for data set 2
    static char old_coil1[260];//  Path and filename used for data set 1
    static char old_coil2[260];//  Path and filename used for data set 2
    int file_flag = 0;

// get defalt values
            GetCtrlVal (main_panel, PANEL_DRATE, &srate);
            GetCtrlVal (main_panel, PANEL_FILE1, coil1);
            GetCtrlVal (main_panel, PANEL_FILE2, coil2);
            GetCtrlVal (main_panel, PANEL_ITER, &iterations);
            GetCtrlVal (main_panel, PANEL_RLENGTH, &rlength);
            GetCtrlVal (main_panel, PANEL_KBINS, &kbins);
            GetCtrlVal (main_panel, PANEL_COILNUM1, &coilnum1);
            GetCtrlVal (main_panel, PANEL_COILNUM2, &coilnum2);


//  calculate number of K values need for analysis
krlength = 2*(int)((rlength/((kbins)*2))+1.0); //divide by two then multiply by two after making int to preserve symetry

// if S is null don't try to free the array because there is nothing to free
// then create new 2s array for omega vs K
if( S != NULL) free_dmatrix(S,old_rlength/2, old_krlength); //Clean memory
S = dmatrix(rlength/2, krlength);  // Create a pointer to a 2d array, i.e. create 2d array

// This section loads information for file #1
            if ( strcmp(old_coil1, coil1) != 0 || old_coil1num1 != coilnum1)
             {
      if( wave1 != NULL) free_dmatrix(wave1,max_data_length1, cols1); //Clean memory
      getfileinfo(coil1, &max_data_length1, &cols1);
             wave1 = dmatrix(max_data_length1, cols1);       // Create a pointer to a 2d array, i.e. create 2d array for
                                    file input
      if (result = getfiledata( wave1, coil1, max_data_length1, cols1) == 0)
            run_coil_correction(wave1,coilnum1,max_data_length1, cols1);
      else file_flag = 1;

      if ( max_data_length1 >= max_data_length2 )
                SetCtrlAttribute (main_panel, PANEL_RLENGTH, ATTR_MAX_VALUE, max_data_length1 );
                else
      SetCtrlAttribute (main_panel, PANEL_RLENGTH, ATTR_MAX_VALUE, max_data_length2 );
              if ( cols1 >= cols2)
                 SetCtrlAttribute (main_panel, PANEL_ITER, ATTR_MAX_VALUE, cols1);
                else
                 SetCtrlAttribute (main_panel, PANEL_ITER, ATTR_MAX_VALUE, cols1);
    }

            if ( strcmp(old_coil2, coil2) != 0 ||  old_coilnum2 != coilnum2)
             {
      if( wave2 != NULL) free_dmatrix(wave2,old_rlength, cols2); //Clean memory
      getfileinfo(coil1, &max_data_length2, &cols2);
                wave2 = dmatrix(max_data_length2, cols2);    // Create a pointer to a 2d array, i.e. create 2d array for
                                              file input
            if (result = getfiledata( wave2, coil2, max_data_length2, cols2) == 0) run_coil_correction(wave2,coilnum2,
                      max_data_length2, cols2);
                else file_flag = 1;

      if ( max_data_length1 >= max_data_length2 )
                         SetCtrlAttribute (main_panel, PANEL_RLENGTH, ATTR_MAX_VALUE, max_data_length1
                                    );
                else
                           SetCtrlAttribute (main_panel, PANEL_RLENGTH, ATTR_MAX_VALUE,
                           max_data_length2 );
```

```
                    if ( cols1 >= cols2)
                              SetCtrlAttribute (main_panel, PANEL_ITER, ATTR_MAX_VALUE, cols1);
                     else
                               SetCtrlAttribute (main_panel, PANEL_ITER, ATTR_MAX_VALUE, cols1);
                  }


// read in file information and if no error in the read start analysis
// procedures else fail with a miserable message.
  if (file_flag == 0)
     {
// Initialize arrays to zero
                          for (i=0;i<rlength/2;i++)
                                   {
                                   ave_wave1_pow[i]=0;
                                   ave_wave2_pow[i]=0;
                                   for(j=0;j<krlength;j++)
                           {
                                   S[i][j] = 0;
                           }
                                   }

// Find the k values looping through for each iteration
                          for (i=0; i < iterations; i++)
                          {

// put in values for time series one at a time for analysis
                          for (j=0; j < rlength; j++)
                          {
                                    wave1out[j]=wave1[j][i];
                    wave2out[j]=wave2[j][i];
               }
// Pauls analysis routine for finding 2d spectral density
    Find_k ( wave1out, wave2out, Theta, cross, ave_wave1_pow, ave_wave2_pow, S, freq);
     }
               for(i=0;i<rlength/2;i++)
                 {
                    freq[i]= (double)i*srate/(double)rlength;
                 }

//  Plot ffts and cross power info
   cross_plot(Theta, cross, freq);
   fft_plot( ave_wave1_pow, ave_wave2_pow, freq);

// set x axis for k and plot intensity and plot intensity
               GetCtrlVal (main_panel, PANEL_DIST, &dist);
               GetCtrlVal (main_panel, PANEL_KLAMBDA_FLAG, &klambda_flag);
               if (klambda_flag == 0)
                 {
                   SetCtrlVal (main_panel, PANEL_XMIN, -PI/dist);
                   SetCtrlVal (main_panel, PANEL_XMAX, PI/dist);
                 }
                else
                 {
                   SetCtrlVal (main_panel, PANEL_XMIN, -dist*PI);
                   SetCtrlVal (main_panel, PANEL_XMAX,  dist*PI);
                 }
   intensity_plot( S, freq);

  }
 else
  {
```

```
                MessagePopup ("Error", "Unable to get data from file");
   }

     old_rlength = rlength; // Store values to clear array later since rlength and krlength
     old_krlength = krlength; // will be different when this function is called again
               strcpy (old_coil1, coil1);
               strcpy (old_coil2, coil2);
               old_coilnum1 = coilnum1;
               old_coilnum2 = coilnum2;
     return S;
 }// end of data analysis

void Find_k (double wave1[MAX_RLENGTH], double wave2[MAX_RLENGTH], double Theta[MAX_RLENGTH],
           double cross[MAX_RLENGTH], double ave_wave1_pow[MAX_RLENGTH],double
ave_wave2_pow[MAX_RLENGTH],
           double **S, double freq[MAX_RLENGTH])
{
      double wave1_I[MAX_RLENGTH];
      double wave2_I[MAX_RLENGTH];
      double wave1_pow[MAX_RLENGTH];
      double wave2_pow[MAX_RLENGTH];
      double real_cross_spec[MAX_RLENGTH];
      double imag_cross_spec[MAX_RLENGTH];
      double K[MAX_RLENGTH/2];
      double coherence[MAX_RLENGTH];
      double coherence_length[MAX_RLENGTH];
      double ca1[MAX_RLENGTH];
      double ca2[MAX_RLENGTH];
      double phase[MAX_RLENGTH];


      double deltak;
      double wave1_mean;
      double wave2_mean;
      double dist;

      int i;
      int j;
      int n;
      int iterations;
      int rlength;
      int krlength;
      int kbins;



                GetCtrlVal (main_panel, PANEL_ITER, &iterations);
                GetCtrlVal (main_panel, PANEL_RLENGTH, &rlength);
                GetCtrlVal (main_panel, PANEL_DIST, &dist);
                GetCtrlVal (main_panel, PANEL_KBINS, &kbins);
//      get_coil_info( freq, ca1, ca2, phase);

// Find the mean for each signal
                Mean(wave1, rlength, &wave1_mean);
                Mean(wave2, rlength, &wave2_mean);

// Subtract mean from signal
                for (j = 0; j < rlength; j ++)
                          {
                                   wave1[j] = (wave1[j] - wave1_mean);
                                   wave2[j] = (wave2[j] - wave2_mean);
                                   wave1_pow[j] = wave1[j];
```

```
                        wave2_pow[j] = wave2[j];
                }

// Create Power Spectrum for each signal
          Spectrum(wave1_pow, rlength);
          Spectrum(wave2_pow, rlength);

// Determine the Cross Spectrum for the two coils.
// cross is the real part (quad)
// Theta is the imaginary part
     CrossSpectrum(wave1, wave2, rlength, real_cross_spec, imag_cross_spec);

          for (j = 1; j < rlength/2; j++)
                {
                  ave_wave1_pow[j] += wave1_pow[j]/iterations;
                  ave_wave2_pow[j] += wave2_pow[j]/iterations;
                        if (cross[j] == 0)
                                cross[j] = 1e-20;

// Size of wavenumber bin
        deltak = kbins*2*PI / (dist * (double) rlength);
    krlength = 2*(int)((rlength/((kbins)*2))+1.0);
//divide by two then multiply by two after making int to preserve symetry
// Subtract the phaseshift of the coils from the measured phase shift and divide
// by the distance to determine the k-value

                for (j = 0; j < rlength/2; j++)
                {
                         K[j] = atan2(imag_cross_spec[j],real_cross_spec[j]) / dist;
                        cross[j] = sqrt(imag_cross_spec[j]*imag_cross_spec[j] +
                                real_cross_spec[j]*real_cross_spec[j]);
                        Theta[j] = atan2(imag_cross_spec[j],real_cross_spec[j]);
/*
                // Calculate the coherency
                        coherence[j] +=
                                sqrt(abs((real_cross_spec[j]/wave2_pow[j])*(real_cross_spec[j]/wave1_pow[j])
                                ))/iterations;

                // Calculate the coherence length
                        if (coherence[j] == 1)
                                coherence[j] = .9999999999;
                        if (coherence[j] == 0)
                                coherence[j] = 1e-20;

                        coherence_length[j] = -dist/(log(coherence[j]));
*/
                }


                for (j = 0; j < rlength/2; j++)
                {
                        for (n = 0; n < krlength/2; n ++)
                                {
         if (K[j] >= 0)
         {
                                        if ( ((double)n-0.5)*deltak < K[j] && ((double)n+0.5)*deltak > K[j] )
                                                {
                                                S[j][((krlength/2) + n)] += (.5 * (wave2_pow[j] +
wave1_pow[j]));//spectral density
                                                }
                                        else
                                                S[j][((krlength/2) + n)] += 0;
```

```
					}
					else
					{
						if ( (-0.5 - (double)n)*deltak < K[j] && (0.5 - (double)n)*deltak >
K[j] )
							{
							S[j][((krlength/2) - n)] += (.5 * (wave2_pow[j] +
wave1_pow[j]));//spectral density
							}
						else
							S[j][((krlength/2) - n)] += 0;
					 }
				}
			}
 }
```

## Source Code fileproc.c

```
/************************************************************
 *                                                                              *
 *         Program          :  K spectrum analysis              *
 *   Writen By         :  John Kline with analysis routine by Paul Keiter*
 *   Date Alpha version :  4/26/2000                               *
 *         File             :  file_proc.c                         *
 *                                                                             *
 *   This file contains procedures for both file input and out put. *
 *                                                                             *
 *  *******************************************************/

#include <userint.h>
#include <formatio.h>
#include <ansi_c.h>
#include <wave.h>
#include <Kspectrum.h>
#include <lowlvlio.h>

/****************************************************************************
 *
 * This procedure opens the input file and determines the number of rows and
 * columns for the file
 *
 ****************************************************************************/
int getfileinfo( char filename[256], int *num_points, int *cols )

  {
    char linein[10001];
    char strcmp1[8] = "time";
    char *strptr;
    int flag = 1;
    int result;
    int j,i;
    int filein;
        *cols = 0;
    *num_points=0;

// Open files
        filein = OpenFile (filename, VAL_READ_ONLY, VAL_OPEN_AS_IS, VAL_ASCII);
        if ( errno == 0 ) flag = 0;

// find first line of data for file 1
        if (flag == 0)
         {
    j = 0;
                ReadLine (filein, linein, 10000);
    while ( result = memcmp (linein, strcmp1, 4) != 0 && j < 30 )
      {
       ReadLine (filein,linein , 10000);
         j++;
      }
    if (j == 30) flag = 1;
                else
                 {
                  for(i=0;i<= strlen(linein);i++)
                   {
                          if( strncmp (&linein[i], ",", 1) == 0 ) *cols= *cols +1;
                   }
       while ( result = eof (filein) == 0 && *num_points < 8192)
              {
```

```
                            ReadLine (filein, linein , 10000);
                            *num_points= *num_points+1;
              }
          }

//  END of file processing
                CloseFile (filein);
  }
  errno = 0;
  return(flag);
 }

/***************************************************************************
 *
 * This procedure opens the input file and determines the number of rows and
 * columns for the file
 *
 ***************************************************************************/

int  getfiledata( double **array1, char filename[256], int num_points, int cols)
  {
    char linein[10001];
    char strcmp1[8] = "time";
    char format[32];
    char *strptr;
    int flag = 1;
    int result;
    int j;
    int filein;

// Open files

        filein = OpenFile (filename, VAL_READ_ONLY, VAL_OPEN_AS_IS, VAL_ASCII);
        if ( errno == 0 ) flag = 0;

// find first line of data for file 1
        if (flag == 0)
         {
    j = 0;
                ReadLine (filein, linein, 10000);
    while ( result = memcmp (linein, strcmp1, 4) != 0 && j < 30 )
      {
        ReadLine (filein,linein , 10000);
         j++;
      }
    if (j == 30) flag = 1;

//              sprintf (format, "%s>%%df[x]", ,cols);
// Read in data for file 1
    while ( result = eof (filein) == 0 && j < num_points)
            {
                          ReadLine (filein, linein , 10000);
                          Scan (linein, "%s>%150f[x]", &array1[j][0]);
                          j++;
            }
//  END of file processing
                CloseFile (filein);

  }
  errno = 0;
  return(flag);
  }
```

```
 /****************************************************************************
 *
 * This procedure opens the input file and determines the number of rows and
 * columns for the file
 *
 ********************************************************************************/

void writefile(double **S, double ave_wave1_pow[MAX_RLENGTH], double ave_wave2_pow[MAX_RLENGTH])
  {

      int rlength;
      int kbins;
      int krlength;
      int file_fft_flag;
      int i;
      double dist;
      double drate;
      double deltak;
      double deltaf;
      char output[260];
      char outputfft[260];
      FILE *outfile;
      FILE *outfft;

      GetCtrlVal (main_panel, PANEL_RLENGTH, &rlength);
             GetCtrlVal (main_panel, PANEL_KBINS, &kbins);
             GetCtrlVal (main_panel, PANEL_DIST, &dist);
      GetCtrlVal (main_panel, PANEL_OUTPUT, output);
      GetCtrlVal (main_panel, PANEL_DRATE, &drate);

      krlength = 2*(int)((rlength/((kbins)*2))+1.0); //divide by two then multiply by two after making int to preserve
                                    symmetry
              deltak = kbins*2*PI / (dist * (double) rlength);
              deltaf= drate/(double)rlength;
              outfile = fopen (output, "w");
              fprintf(outfile,"Delta K = %e\n",deltak);
              fprintf(outfile,"Delta Freq = %e\n", drate/rlength);
              fprintf(outfile,"\nDATA\n");
              fclose(outfile);


             ArrayToFile (output, *S, VAL_DOUBLE, krlength*(rlength/2),rlength/2, VAL_GROUPS_TOGETHER,
                         VAL_GROUPS_AS_ROWS, VAL_SEP_BY_COMMA, 10, VAL_ASCII, VAL_APPEND);

// Save fft info with 2d array in separate file with .fft at the end
      GetMenuBarAttribute (menu_handle, MAIN_PREF_RESCALE, ATTR_CHECKED, &file_fft_flag);
               if ( file_fft_flag == 1 )
                 {
                           strcpy (outputfft, output);
                     strncat (outputfft, ".fft", 4);
               outfft = fopen (outputfft, "w");
                           fprintf(outfft,"freq,fft series #1, fft series #2\n");
         for( i=0; i<rlength;i++)
           {
fprintf(outfft,"%e,%e,%e\n",(double)i*deltaf,ave_wave1_pow[i],ave_wave2_pow[i]);
           }
                           fclose(outfft);
        }
```

## Source Code DARRAY.C

```
/*****************************************************************************
*    Program            :  K spectrum analysis
*    Writen By          :  John Kline with analysis routine by Paul Keiter  *
*    Date Alpha version :  4/26/2000
  * The follow routines create a 2d array( returning a pointer to it) and frees a
  * 2d array. These two routines where copied from numerical recipies in C and *
  * modified for use in this program.
*****************************************************************************/

#include <analysis.h>
#include <ansi_c.h>

// This routine creates the 2d array returning a pointer
double **dmatrix(int rows, int cols)
  {
     int i;
     double **m;

     m = (double **) malloc((size_t)((rows)*sizeof(double*)));
     m[0] = (double *) malloc((size_t)(rows*cols*sizeof(double)));

     for ( i = 1; i < rows; i++)
      {
        m[i]=m[i-1] + cols;
      };
     return m;
  }

// This routine frees the memory pointed to by a pointer
void free_dmatrix( double **m, int rows, int cols)

  {
                free((char *) m[0]);
                free((char *) m);
  }
```

## Source Code COILINFO.C

```
/*********************************************************************************
 *                                                                              *
 *          Program          :  K spectrum analysis                            *
 *   Writen By         :  John Kline with analysis routine by Paul Keiter*
 *   Date Alpha version :  4/26/2000                                            *
 *                                                                              *
 *          This file contains functions that correct the time series data for phase and       *
 *   effective coil area.  The algorithym passes functions for the phase correction as a     *
 *   function of frequency and the effective coil area as a function of frequency for each *
 *   coil.  These functions are created from coil calibration data for each coil.  A case  *
 *   statement assigns a pointer to the functions for phase and effective coil area based  *
 *   control on front panel.  Then the coil correction is done in frequency space by       *
 *   adjusting the real and imaginary parts for both phase and amplitude.  To get the      *
 *   right the signs of the real and imaginary part had to be done manually.                      *
 *                                                                                              *
 *          Windowing of time series (Hanning) moved to after storage of corrected times series    *
 *                    so stored time series are unwindowed.
**********************************************************************************************/

#include <analysis.h>
#include <ansi_c.h>
#include <analysis.h>
#include <Kspectrum.h>
#include <wave.h>

typedef double ModelFunc(double);   // defines type so function can be passed as variable

#define NONE  0

// LPA Theta coils 5,8, and 9
#define LPA5 5
#define LPA8 8
#define LPA9 9

double LPA5CA(double f) {return(974.67+2.4484*(f*1.0e-3)-0.33565*pow((f*1.0e-3),2)
                        +0.0043464*pow((f*1.0e-3),3)-1.8052e-05*pow((f*1.0e-3),4));}
double LPA5P(double f) {return((90.329+1.4759*(f*1.0e-3)-0.0053901*pow((f*1.0e-3),2))*PI/180.0);}

double LPA8CA(double f) {return(728.65-5.1309*(f*1.0e-3)-0.23834*pow((f*1.0e-3),2)
                        +0.00447*pow((f*1.0e-3),3)-2.1768e-05*pow((f*1.0e-3),4));}
double LPA8P(double f) {return((93.445+2.6485*(f*1.0e-3)-0.011834*pow((f*1.0e-3),2))*PI/180.0);}

double LPA9CA(double f) {return(979.72+1.9369*(f*1.0e-3)-0.30621*pow((f*1.0e-3),2)
                       +0.0036231*pow((f*1.0e-3),3)-1.732e-05*pow((f*1.0e-3),4));}
double LPA9P(double f) {return((89.759+1.8344*(f*1.0e-3)-0.0058301*pow((f*1.0e-3),2))*PI/180.0);}

// LPA Radial coils 2,4 and 7
#define LPA2  2
#define LPA4  4
#define LPA7  7

double LPA2CA(double f) {return(1101.7-6.9856*(f*1.0e-3)-0.35504*pow((f*1.0e-3),2)
                       +0.006463*pow((f*1.0e-3),3)-3.109e-05*pow((f*1.0e-3),4));}
double LPA2P(double f) {return((93.357+2.5753*(f*1.0e-3)-0.010962*pow((f*1.0e-3),2))*PI/180.0);}

double LPA4CA(double f) {return(975.41-7.4235*(f*1.0e-3)-0.30644*pow((f*1.0e-3),2)
                       +0.0057878*pow((f*1.0e-3),3)-2.79945e-05*pow((f*1.0e-3),4));}
double LPA4P(double f) {return((93.889+2.4118*(f*1.0e-3)-0.01205*pow((f*1.0e-3),2))*PI/180.0);}

double LPA7CA(double f) {return(1320.0-2.5788*(f*1.0e-3)-0.5363*pow((f*1.0e-3),2)
```

```
                              +0.0083681*pow((f*1.0e-3),3)-3.7721e-05*pow((f*1.0e-3),4));}
double LPA7P(double f) {return((91.82+1.8344*(f*1.0e-3)-0.0096852*pow((f*1.0e-3),2))*PI/180.0);}

// LPA Radial coils 1,3 and 6
#define LPA1  1
#define LPA3  3
#define LPA6  6

double LPA1CA(double f) {return(999.85-0.35549*(f*1.0e-3)-0.2376*pow((f*1.0e-3),2)
                              +0.0028775*pow((f*1.0e-3),3)-1.0998e-05*pow((f*1.0e-3),4));}
double LPA1P(double f) {return((90.286+1.7886*(f*1.0e-3)-0.0055725*pow((f*1.0e-3),2))*PI/180.0);}

double LPA3CA(double f) {return(975.85-0.33916*(f*1.0e-3)-0.2198*pow((f*1.0e-3),2)
                              +0.0025455*pow((f*1.0e-3),3)-9.2875e-06*pow((f*1.0e-3),4));}
double LPA3P(double f) {return((91.634+1.7415*(f*1.0e-3)-0.005064*pow((f*1.0e-3),2))*PI/180.0);}

double LPA6CA(double f) {return(967.69+1.2161*(f*1.0e-3)-0.28645*pow((f*1.0e-3),2)+
                               0.0034795*pow((f*1.0e-3),3)-1.3458e-05*pow((f*1.0e-3),4));}
double LPA6P(double f) {return((90.037+1.7897*(f*1.0e-3)-0.005674*pow((f*1.0e-3),2))*PI/180.0);}

// HPA radial probes
#define HPAR1 10
#define HPAR2 11
#define HPAR3 12
#define HPAR4 13
#define HPAR5 14

double HPAR1CA(double f) {return(27.726*exp(-9.9472e-08*f));}
double HPAR1P(double f) {return(-1.681-2.6379e-08*f);}

double HPAR2CA(double f) {return(40.522*exp(-1.0111e-07*f));}
double HPAR2P(double f) {return(-1.7386-2.4374e-08*f);}

double HPAR3CA(double f) {return(32.946*exp(-9.3124e-08*f));}
double HPAR3P(double f) {return(1.365-2.2378e-08*f);}

double HPAR4CA(double f) { return(21.71*exp(-9.227e-08*f));}
double HPAR4P(double f) {return(-1.5143-3.405e-08*f);}

double HPAR5CA(double f){return(37.857*exp(-8.9839e-08*f));}
double HPAR5P (double f){return(1.4265-3.0479e-08*f);}

// HPA Z probes
#define HPAZ1 15
#define HPAZ2 16
#define HPAZ3 17
#define HPAZ4 18
#define HPAZ5 19

double HPAZ1CA(double f) {return(29.05*exp(-9.2701e-08*f));}
double HPAZ1P(double f) {return(1.4357-2.7329e-08*f);}

double HPAZ2CA(double f) {return(14.152*exp(-8.8728e-08*f));}
double HPAZ2P(double f) {return(-1.5607-2.8666e-08*f);}

double HPAZ3CA(double f) {return(32.986*exp(-9.5409e-08*f));}
double HPAZ3P(double f) {return(-1.667-2.3509e-08*f);}

double HPAZ4CA(double f) { return(25.382*exp(-9.6384e-08*f));}
double HPAZ4P(double f) {return(1.453-2.4226e-08*f);}

double HPAZ5CA(double f){return(25.237*exp(-8.664e-08*f));}
```

```
double HPAZ5P (double f){return(1.5475-2.9145e-08*f);}

// HPA Theta probes
#define HPAT1 20
#define HPAT2 21
#define HPAT3 22
#define HPAT4 23
#define HPAT5 24

double HPAT1CA(double f) {return(24.176*exp(-1.0422e-07*f));}
double HPAT1P(double f) {return(-1.7156-3.4264e-08*f);}

double HPAT2CA(double f) {return(24.744*exp(-8.4643e-08*f));}
double HPAT2P(double f) {return(1.3945-2.7713e-08*f);}

double HPAT3CA(double f) {return(35.096*exp(-9.2822e-08*f));}
double HPAT3P(double f) {return(1.3474-6.0613e-08*f);}

double HPAT4CA(double f) { return(34.192*exp(-1.0423e-07*f));}
double HPAT4P(double f) {return(-1.7573-1.873e-08*f);}

double HPAT5CA(double f){return(26.841*exp(-9.4092e-08*f));}
double HPAT5P (double f){return(-1.63-2.7011e-08*f);}

void run_coil_correction( double **array, int coil, int max_data_length, int cols)
  {

     double real[MAX_RLENGTH];             // real part of fft
     double imaginary[MAX_RLENGTH];          // imaginary part of fft
     double freq[MAX_RLENGTH];                // frequency axis
     double p;                                // phase correcton constant
     double f1;                                // real part temporary correction variable
     double i1;                                // imaginary part temporary correction variable
     double f2;                               // real part temporary correction variable
     double i2;                               // imaginary part temporary correction variable
     double theta;                     // phase of correction factor
     double drate;                     // digitazation rate
     int i,j;                                 // counter variables
     ModelFunc  *phase;                        // pointer to phase correction function
     ModelFunc  *ca;                          // pointer to coil area correction function

     FILE *outfile;

     if ( coil != NONE)
       {
        GetCtrlVal (main_panel, PANEL_DRATE, &drate);

        for(i=0;i<=max_data_length/2;i++) freq[i] = i*drate/ (double)max_data_length;

              switch (coil)
                   {
                      case HPAR1:  // HELIX PROBE ARRAY COIL
                        phase = &HPAR1P;
                        ca = &HPAR1CA;
                            break;
                      case HPAR2:  // HELIX PROBE ARRAY COIL
                        phase = &HPAR2P;
                        ca = &HPAR2CA;
                            break;
                      case HPAR3:  // HELIX PROBE ARRAY COIL
                        phase = &HPAR3P;
                        ca = &HPAR3CA;
```

```
          break;
case HPAR4:  // HELIX PROBE ARRAY COIL
  phase = &HPAR4P;
  ca = &HPAR4CA;
          break;
case HPAR5:  // HELIX PROBE ARRAY COIL
  phase = &HPAR5P;
  ca = &HPAR5CA;
          break;
case HPAZ1:  // HELIX PROBE ARRAY COIL
  phase = &HPAZ1P;
  ca = &HPAZ1CA;
          break;
case HPAZ2:  // HELIX PROBE ARRAY COIL
  phase = &HPAZ2P;
  ca = &HPAZ2CA;
          break;
case HPAZ3:  // HELIX PROBE ARRAY COIL
  phase = &HPAZ3P;
  ca = &HPAZ3CA;
          break;
case HPAZ4:  // HELIX PROBE ARRAY COIL
  phase = &HPAZ4P;
  ca = &HPAZ4CA;
          break;
case HPAZ5:  // HELIX PROBE ARRAY COIL
  phase = &HPAZ5P;
  ca = &HPAZ5CA;
          break;
case HPAT1:  // HELIX PROBE ARRAY COIL
  phase = &HPAT1P;
  ca = &HPAT1CA;
          break;
case HPAT2:  // HELIX PROBE ARRAY COIL
  phase = &HPAT2P;
  ca = &HPAT2CA;
          break;
case HPAT3:  // HELIX PROBE ARRAY COIL
  phase = &HPAT3P;
  ca = &HPAT3CA;
          break;
case HPAT4:  // HELIX PROBE ARRAY COIL
  phase = &HPAT4P;
  ca = &HPAT4CA;
          break;
case HPAT5:  // HELIX PROBE ARRAY COIL
  phase = &HPAT5P;
  ca = &HPAT5CA;
          break;
case LPA1:  // LEIA PROBE ARRAY COIL 1 Bz
  phase = &LPA1P;
  ca = &LPA1CA;
break;
case LPA2:  // LEIA PROBE ARRAY COIL 2 Br
  phase = &LPA2P;
  ca = &LPA2CA;
          break;
case LPA3:  // LEIA PROBE ARRAY COIL 3 Bz
  phase = &LPA3P;
  ca = &LPA3CA;
          break;
case LPA4:  // LEIA PROBE ARRAY COIL 4 Bz
```

```
                                phase = &LPA4P;
                                ca = &LPA4CA;
                                        break;
                           case LPA5:  // LEIA PROBE ARRAY COIL 5 Bt
                                phase = &LPA5P;
                                ca = &LPA5CA;
                                        break;
                           case LPA6:  // LEIA PROBE ARRAY COIL 6 Bz
                                phase = &LPA6P;
                                ca = &LPA6CA;
                                        break;
                           case LPA7:  // LEIA PROBE ARRAY COIL 7 Br
                                phase = &LPA7P;
                                ca = &LPA7CA;
                                        break;
                           case LPA8:  // LEIA PROBE ARRAY COIL 8 Bt
                                phase = &LPA8P;
                                ca = &LPA8CA;
                                        break;
                           case LPA9:  // LEIA PROBE ARRAY COIL 9 Bt
                                phase = &LPA9P;
                                ca = &LPA9CA;
                                        break;
                            }

                          for (j = 0; j < cols; j++)
                            {
                              for( i = 0; i <max_data_length; i++)
             {
                                     real[i]= array[i][j]; // put new time series into real for fft
                                     imaginary[i] = 0;      // zero imaginary array before fft or fft will be wrong

                                     }

                 FFT(real, imaginary, max_data_length);
            for( i = 1; i < max_data_length/2; i++)
                               {

// theta is the phase correction to be made.  The modulus function keeps the value between
// plus and minus 2*PI so the difference in the two phase factors is not with in the percision
// of the variable, i. e. we don't subtract 0.123 rad from 4.3234e13 rad which looks like 4.3234e13
// rad

theta = fmod((atan2(imaginary[i],real[i])-fmod(phase(freq[i]),2*PI)),(2*PI));
p = tan(atan2(imaginary[i],real[i])-fmod(phase(freq[i]),2*PI));
i1 = fabs(real[i]*p);
f2 = fabs(real[i])*(sqrt( pow(real[i],2) + pow(imaginary[i],2))/ sqrt(pow(real[i],2) + pow(i1,2)));
i2 = i1*(sqrt( pow(real[i],2) + pow(imaginary[i],2))/ sqrt(pow(real[i],2) + pow(i1,2)));

// Set the values for real and imaginary part to correct quadrant
                if (( theta > (PI/2) && theta < PI) || (theta < -PI && theta > (-3*PI/2) ))
                  {
                     f2*=-1;
                  }
                if (( theta > PI && theta < (3*PI/2)) || (theta < -1.57 && theta > -PI ))
                  {
                     f2*=-1;
                     i2*=-1;
                  }
                if (( theta > (3*PI/2) && theta < (2*PI)) || (theta < -0.00 && theta > (-1*PI/2) ))
                  {
                     i2*=-1;
```

```
            }

// put the phase corrected value in for real and imaginary parts of fft
                                   real[i] = f2;
                                   imaginary[i] = i2;
                                   real[max_data_length-i] = f2;
                                   imaginary[max_data_length-i] = -1*i2;
// correct for effective coil area both real and imaginary parts of fft.
                                   real[i] *= ca(freq[i])/sqrt(2);
                                   imaginary[i] *= ca(freq[i])/sqrt(2);
                                   real[max_data_length-i] *= ca(freq[i])/sqrt(2);
                                   imaginary[max_data_length-i] *= ca(freq[i])/sqrt(2);
                                  }
// inverse fft
                          ReInvFFT (real, imaginary, max_data_length);

// Uncomment this section to save corrected time series info
// This saves the second column of input file number 2
//                        if( j == 1) outfile = fopen("time.out", "w");
// Store the corrected time series back into the originally passed array
                          for( i = 0; i < max_data_length; i++)
                           {
                            array[i][j]=real[i];
//                          if ( j == 1) fprintf(outfile,"%e\n", real[i]);
                           }
//                        if (j == 1) fclose(outfile);
// Hanning window choosen because there is very little harmonic leakage into other frequencies.
                    HanWin (real, max_data_length);

                         }
                 }
}
```

## VITAE

Matthew M. Balkey

Employment:

Research Assistant, 1997 - 2000
    West Virginia University.
Research Physicist, summer 1997
    Space Plasma Physics Group, Los Alamos National Laboratory
Teaching Assistant, August 1995 - 1996
    West Virginia University.
Research Assistant, summer 1994
    West Virginia University.

Education:

M. S. in Plasma Physics, 1998.
    West Virginia University
B. S. in Plasma Physics, 1995.
    Wheeling Jesuit College
    Cum Laude with honors

Awards and Honors:

NRC Research Fellowship 2000

Professional Memberships:

The American Physical Society
    Division of Plasma Physics
The American Geophysical Union

Publications:

1. C. J. Pollock, K. Asamura, M.M. Balkey, J.L. Burch, H.O. Funsten, M. Grande, M. Gruntman, J.-M. Jahn, M. Lampton, D. J. McComas, T. Mukai, M.L. Schattenburg, E. Scime, R. Skoug, P. Valek, S. Widner, and M. Wuest, 'Medium Energy Neutral Atom Images of the Earth's Magnetosphere During Substorms and Storm-time,' submitted to *Geophys. Res. Lett.* (2000).
2. M. Balkey, R. Boivin, P. A. Keiter, J. L. Kline, and E. Scime, 'Observation of uncorrelated ion heating and density production in a helicon source,' submitted to *Plasma Sources Sci. and Tech.* (2000).
3. E. Scime, R. Boivin, M. Balkey, and J. Kline, 'Microwave Interferometer for Steady-State Plasmas,' submitted to *Rev. Sci. Instrum.* (2000).

4. Earl E. Scime, Paul A. Keiter, S. Peter Gary, Matthew M. Balkey, Robert F. Boivin, John L. Kline, and Melanie Blackburn, 'Ion Temperature Anisotropy Limitation in High Beta Plasmas,' *Phys. Plasmas* **7**, 2157 (2000).
5. C. J. Pollock, M. Balkey, J. Burch, J. Cravens, G. Dirks, H. Funsten, M. Grande, M. Gruntman, j.-M. Jahn, M. Lampton, D. J. McComas, T. Mukai, S. Pope, S. Ritzau, M. Schattenburg, E. Scime, R. Skoug, P. Valek, S. Wiidner, M. Wuest, 'Medium Energy Neutral Atom (MENA) Imager for the IMAGE Mission,' *Space Sci. Reviews* **91**, 113 (2000).
6. Paul A. Keiter, Earl E. Scime, Matthew M. Balkey, Robert Boivin, John L. Kline and S. Peter Gary, 'Beta-Dependent Upper Bound on Ion Temperature Anisotropy in a Laboratory Plasma,' *Phys. Plasmas* **7**, 779 (2000).
7. J. L. Kline, E. E. Scime, P.A. Keiter, M. M. Balkey, and R. F. Boivin, 'Ion Heating in the HELIX helicon plasma source,' *Phys. Plasmas* **6**, 4767 (1999).
8. Matthew M. Balkey, Earl E. Scime, Mark L. Schattenburg, Joost van Beek, ‘Effects of Slit Width on VUV Transmission Through Sub-Micron Period, Free-Standing, Transmission Gratings,’ *App. Optics* **37**, 5087 (1998).
9. Earl E. Scime and M. M. Balkey, ‘Compact, Intense, Monochromatic, Atmospheric Pressure, Extreme Ultraviolet Light Source,’ *Rev. Sci. Instrum.* **69**, 1581-1583 (1998).
10. Earl E. Scime, Paul A. Keiter, Michael W. Zintl, Matthew M. Balkey, John L. Kline, and Mark E. Koepke, ‘Control of Ion Temperature Anisotropy in a Helicon Plasma,’ *Plasma Sources Sci. and Technol.* **7**, 186-191 (1998).
11. Keiter, P. A., E. E. Scime and M. M. Balkey, ‘Frequency dependent effects in helicon plasmas,’ *Phys. Plasmas* **4**, 2741 (1997).